Monte Carlo Studies of Electron Transport In Semiconductor Nanostructures

by

Brian David Tierney

A Dissertation Presented in Partial Fulfillment
of the Requirements for the Degree
Doctor of Philosophy

Approved September 2011 by the
Graduate Supervisory Committee:

Stephen Goodnick, Chair
David Ferry
Richard Akis
Marco Saraniti
Dragica Vasileska

ARIZONA STATE UNIVERSITY

December 2011

©2011 Brian David Tierney
All Rights Reserved

ABSTRACT

An Ensemble Monte Carlo (EMC) computer code has been developed to simulate, semi-classically, spin-dependent electron transport in quasi two-dimensional (2D) III-V semiconductors. The code accounts for both three-dimensional (3D) and quasi-2D transport, utilizing either 3D or 2D scattering mechanisms, as appropriate. Phonon, alloy, interface roughness, and impurity scattering mechanisms are included, accounting for the Pauli Exclusion Principle via a rejection algorithm. The 2D carrier states are calculated via a self-consistent 1D Schrödinger-3D-Poisson solution in which the charge distribution of the 2D carriers in the quantization direction is taken as the spatial distribution of the squared envelope functions within the Hartree approximation. The wavefunctions, subband energies, and 2D scattering rates are updated periodically by solving a series of 1D Schrödinger wave equations (SWE) over the real-space domain of the device at fixed time intervals. The electrostatic potential is updated by periodically solving the 3D Poisson equation. Spin-polarized transport is modeled via a spin density-matrix formalism that accounts for D'yakanov-Perel (DP) scattering. Also, the code allows for the easy inclusion of additional scattering mechanisms and structural modifications to devices.

As an application of the simulator, the current voltage characteristics of an InGaAs/InAlAs HEMT are simulated, corresponding to nanoscale III-V HEMTs currently being fabricated by Intel Corporation. The comparative effects of various scattering parameters, material properties and structural attributes are investigated and compared with experiments where reasonable agreement is obtained.

The spatial evolution of spin-polarized carriers in prototypical Spin Field Effect Transistor (SpinFET) devices is then simulated. Studies of the spin coherence times in quasi-2D structures is first investigated and compared to experimental results. It is found that the simulated spin coherence times for GaAs structures are in reasonable agreement with experiment.

The SpinFET structure studied is a scaled-down version of the InGaAs/InAlAs HEMT discussed in this work, in which spin-polarized carriers are injected at the source, and the coherence length is studied as a function of gate voltage via the Rashba effect.

DEDICATION

This dissertation is dedicated to my wife Camille. Her patience and support have been monumental while I have been in the Ph.D. program; a time span that has covered the birth of our wonderful children, Brendan and Caitlin, and the start of my secondary career as an Officer in the United States Army Reserve.

ACKNOWLEDGMENTS

I gratefully acknowledge the support of my advisor, Doctor Stephen Goodnick. In addition to his financial support, Dr. Goodnick has given me the intellectual freedom to explore various methodologies related to this work. Furthermore, Dr. Goodnick facilitated the collaborative opportunities afforded me by the members of the Numerical Device Modeling Group of Intel Corporation, who are also duly acknowledged.

Additionally, the guidance and time provided to me by the members of my Ph.D. supervisory committee is gratefully acknowledged. Gratitude is owed to Dr. Richard Akis for sharing with me his knowledge, his repository of related results, and his office camaraderie. I am thankful to Dr. David Ferry for his constructive criticisms and the rigor to which he has held me accountable. To Dr. Marco Saraniti, whom I met while I was still a student at Illinois Institute of Technology (IIT) in Chicago, I owe the opportunity to do research at Arizona State University (ASU) and my introduction to this field. A great deal of gratitude is also owed to Dr. Dragica Vasileska for sharing her expertise and for her uplifting words of encouragement over the years.

Special thanks are also given to the many friends, fellow students and mentors who have helped me throughout graduate school, including: Dr. Jason Ayubi-Moak, for his counsel and countless discussions on Monte Carlo Modeling; Dr. Larry Cooper, for sharing with me his expertise and providing me with many words of encouragement; Dr. Aron Cummings, for many enlightening discussions on spin dynamics; Dr. Timothy Day, for his related experimental

contributions and discussions; Dr. John Shumway, for his critiques and insight into issues regarding quantum transport; Dr. Denis Mamaluy for the many hours he devoted to reviewing my work and discussing the validity of various numerical techniques with me; Dr. Gil Speyer, of the High Performance Computing Initiative at ASU, for his assistance with my computing issues; Dr. James Stine, formerly of IIT, who mentored me earlier in my career; and Dr. Clarence Tracy for many enlightening discussions.

Additionally, a word of thanks must be given to Dr. Goodnick's office staff, in particular Rebecca Davis, who helped me navigate many administrative issues and was my friend throughout the process.

TABLE OF CONTENTS

Page

LIST OF FIGURES ... x

CHAPTER

1 INTRODUCTION ... 1
  - 1.1 Background and Motivation ... 1
  - 1.2 Semi-classical Monte Carlo Simulation ... 5
  - 1.3 Dissertation Organization ... 9

2 CARRIER SCATTERING MECHANISMS ... 10
  - 2.1 Overview ... 10
  - 2.2 Fermi’s Golden Rule ... 11
  - 2.3 3D Scattering Mechanisms ... 12
    - 2.3.1 3D Polar Optical Phonon Scattering ... 14
    - 2.3.2 3D Acoustic Deformation Potential Scattering ... 17
    - 2.3.3 3D Non-Polar Optical Scattering ... 18
    - 2.3.4 3D Ionized Impurity Scattering ... 20
    - 2.3.5 3D Alloy Scattering ... 21
  - 2.4 2D Scattering Mechanisms ... 22
    - 2.4.1 2D Polar Optical Scattering ... 24
    - 2.4.2 2D Acoustic Phonon Scattering ... 26
    - 2.4.3 2D Non-Polar Optical Scattering ... 26
    - 2.4.4 2D Interface Roughness Scattering ... 26
    - 2.4.5 2D Alloy Scattering ... 29

CHAPTER Page

2.5 Plots of 2D Scattering Rates 29

3 ENSEMBLE MONTE CARLO DEVICE SIMULATOR 37

3.1 Overview... 37

3.2 Monte Carlo Transport Kernel..................................... 40

3.3 Structural Definitions and Nomenclature 43

3.4 Time Step and Mesh Size Criteria 45

3.5 Initialization of Carrier Distribution 46

3.6 Descritization of Poisson's Equation........................... 49

3.7 Descritization of SWE.. 51

3.8 Carrier Motion 53

3.8.1 Specular Reflection 55

3.8.2 Barrier Encounters for 3D Carriers.................... 56

3.9 2D→3D Transitions 57

3.10 3D→2D Transitions 58

3.11 Scattering Final State Selection 59

3.11.1 Isotropic Scattering 59

3.11.2 Anisotropic Scattering...................................... 61

3.12 Inclusion of Degeneracy (Pauli Exclusion Principle) . 64

3.13 Inclusion of Spin Dynamics.. 67

3.14 Contact Modeling.. 71

4 SIMULATION RESULTS 75

4.1 Model Verification 75

CHAPTER Page

4.2 Intel Corp. HEMT Simulation 77

4.3 Spintronics Simulation Results 92

5 SUMMARY AND FUTURE WORK.. 99

REFERENCES 102

LIST OF FIGURES

Figure Page

2.1 Schematic depiction of interface roughness in a semiconductor heterointerface 27

2.2 Polar optical 2D phonon scattering for a 13nm $In_{0.7}Ga_{0.3}As$ quantum well bound by $In_{0.52}Al_{0.48}As$ cladding layers 31

2.3 Acoustic 2D phonon scattering rate for a 13nm $In_{0.7}Ga_{0.3}As$ quantum well bound by $In_{0.52}Al_{0.48}As$ cladding layers 32

2.4 Intervalley non-polar optical phonon scattering rate for a 13nm $In_{0.7}Ga_{0.3}As$ quantum well 34

2.5 Roughness and alloy scattering rates for the 13nm $In_{0.7}Ga_{0.3}As$ quantum well 35

2.6 Total scattering rate from the 1st subband of the 13nm $In_{0.7}Ga_{0.3}As$ quantum well 36

3.1 Flowchart of the Ensemble Monte Carlo process 37

3.2 Depiction of the scattering table at a particular value of kinetic energy in the range $E_k \pm dE_k/2$ 43

3.3 One-dimensional depiction of the non-uniform center-point difference grid, showing the variation of effective mass and permittivity parameters. 44

3.4 Depiction of specular reflection at a Neumann boundary 56

Figure Page

3.5 Scattering angles in the isotropic scattering process 60

3.6 Rotated coordinate system used to determine anisotropic scattering angle 61

3.7 Rotated coordinate system for anisotropic scattering........................ 62

3.8 Boundary conditions imposed on HEMT during EMC simulation, in the absence of a tunneling model 74

4.1 Bulk GaAs EMC simulation. T=300K. 3-valley model. (Γ, L, X valleys) 76

4.2 Bulk GaAs velocity field characteristics from EMC simulation. T=300K. 3-valley model. (Γ, L, X valleys) 77

4.3 Intel Corp. HEMT simulated structure.. 78

4.4 Velocity field characteristics corresponding to the gate heterostructure of Figure 4.3 as a function of the interface roughness height.. 79

4.5 Velocity field characteristics corresponding to the gate heterostructure of Figure 4.3 as a function of the alloy disorder potential at roughness height of 0.6nm and length of 1.5 nm 80

4.6 Lower curves: Effect of two different 2D effective mass calculation schemes on velocity field results for the gate heterostructure of Figure 4.4... 81

4.7 EMC simulation of I_d vs. V_{ds} curves for the structure depicted in Figure 4.3, and the corresponding experimental results of [17]........ 82

4.8 Simulated I_d vs. V_{gs} curves for the structure depicted in Figure 4.3, and the corresponding experimental results of [17], at V_{ds} = 0.5V,.. 83

4.9 Calculated transconductance based on Figure 4.8 EMC curve......... 84

4.10 Effect of various scattering parameters and quantum well widths on HEMT drive current 85

4.11 Plot of cumulative charge vs. time through the source and drain for the contacts for the device depicted in Figure 4.3. V_{gs} =0.9 V , V_{ds} =0.0 V.. 87

4.12 Plot of cumulative charge vs. time through the source and drain for the contacts for the device depicted in Figure 4.3. V_{gs} =0.9 V, V_{ds} =0.8 V.. 87

4.13 Average carrier velocity and energy at V_{gs} = 0.5V, V_{ds} = 0.5V........ 88

4.14 Potential energy profile over the simulation domain at V_{gs}=0.8V, V_{ds}=0.8V. 89

4.15 Steady-State carrier density at V_{gs}=0.8V, V_{ds}=0.8V, corresponding to the potential profile plot in Figure 4.14... 90

4.16 Rotated view of Figure 4.15 91

4.17 Carrier density at V_{gs}=0.8V, V_{ds}=0.1V. The figure is oriented in the same way as in Figure 4.16 92

Figure Page

4.18 Spin relaxation rates, as determined by the EMC are compared to experimental data for various well widths. 94

4.19 Decoherence as a function of "position" in k-space, for the heterostructure of the gate region of the Intel HEMT device depicted in Figure 4.3. T=77K. 96

4.20 Spin polarization as a function of source to drain position in a scaled down version of the Intel HEMT depicted in Figure 4.3. V_{ds}= 0.15V. T= 77K 97

1. Introduction

1.1 Background and Motivation

Since the commercial realization of Integrated Circuits (ICs) in the 1960s, the number of transistors that can be economically fabricated onto a single IC "chip" has doubled nearly every two years. This extraordinary trend is believed by many to have been postulated shortly after the invention of the IC in 1958 and has become popularly known as "Moore's Law", in recognition of Intel Corporation co-founder Gordon Moore's famous 1965 exposé on the matter [1].

From a device physics standpoint, a primary reason that the semiconductor industry has been able to adhere to this trend for over forty years is due to the remarkable scaling properties of the silicon Metal Oxide Semiconductor Field Effect Transistor (MOSFET) [2,3,4,5]. This device is the basic building block of the ubiquitous complementary metal oxide semiconductor (CMOS) logic IC scheme. In fact, as of 2011, the minimum feature sizes in state-of-the-art commercially available MOSFETs are on the order of 30 nm [6], as opposed to feature sizes on the order of tens of microns for the first microprocessors that appeared on the market in the early 1970s. Such feature size scaling has resulted in today's most advanced microprocessors containing around 2.5 *billion* transistors per chip, as opposed to a few thousand per chip in the early 1970s. Consequently, today's length scales of less than 100 nm allow clocking frequencies on the order of a few Gigahertz, as opposed to the hundreds of KHz range that was the state of the art in the early 1970s.

Alarmingly though, as silicon MOSFETs continue to scale toward the 10 nanometer regime, the physical limitations of scaling become very apparent. Specifically, as silicon devices are scaled into the tens of nanometers regime, short channel effects and gate leakage currents become problematic [7]. Additionally, if Moore's Law were to continue over the next decade, increasing integration densities due to continued scaling would result in on-chip heat dissipation on the order of hundreds, if not thousands, of watts per square centimeter. Compounding the problem is that voltage scaling in silicon MOSFETs below about 1.0V is very difficult, as the electron mobility of silicon severely hinders drive currents at sub-1V source-to-drain bias voltages [8,9].

Furthermore, from a manufacturing standpoint, the fabrication of sub-10nm devices is very problematic. In fact, diffraction effects destroy the resolution of the lithographic process and random process variations become increasingly difficult to control below about 10nm resolution [10].

While the use of gate insulating materials in MOSFETs with relatively higher dielectric constants compared to SiO_2, known as "high-k dielectrics", has forestalled an abrupt end to Moore's Law within the past few years [11], alternatives to silicon based logic devices are clearly needed if aggressive scaling is to continue past the current decade. Indeed, an end to the future "CMOS roadmap" based on Moore's Law is looming unless other technologies can be utilized whose operational capabilities exceed those of silicon MOSFETS, and can also be economically fabricated into ICs by exploiting the well established layout designs of silicon-based CMOS circuitry and the associated fabrication processes.

Amongst the most attractive candidates to replace aggressively scaled silicon based logic devices are FET devices constructed from heterostructures of III-V compounds and their alloys such as GaAs, InAs, AlAs and $In_xGa_{1-x}As$. Such High Electron Mobility Transistors (HEMTs) exhibit low-field mobilities in excess of 10,000cm^2/V-s. This is because electron transport in these devices occurs in a quasi-2D electron gas formed in the quantum well channel that exists between heterolayers with varying conduction band offsets. Furthermore, scattering in HEMTs is greatly reduced, as compared to other III-V devices such as metal semiconductor field effect transistors (MESFETs) or modulation doped semiconductor field effect transistors (MODFETs), due to the physical separation of dopant layers from the transport channel by barrier layers several nanometers thick [12,13,14,15]. Additionally, HEMTs have demonstrated operating frequencies on the order of several hundred GHz [16], and recent experimental research into 30nm HEMT devices shows drive currents comparable to the most aggressively scaled silicon devices and transconductances on the order of 3000 uS/mV, at bias voltages less than 1 Volt [17].

Furthermore, while extensive HEMT research has occurred since the early 1980s [12,13,14,15,16,17], only since the 1990s has the fabrication process matured such that the devices are now widely used in mobile phone applications and power amplifiers [18]. This process maturity suggests that economical, high volume production of these devices as logic elements in CMOS-style layout schemes may be possible [19].

However, if III-V devices with feature sizes on the order of a few tens of nanometers are to exist on the "CMOS Roadmap", extensive research into their operational capabilities is still needed. Naturally, a crucial component of the research process is the conduction of low-cost computer "simulation experiments".

Therefore, the development of the III-V Monte Carlo device simulator presented in this dissertation is motivated by the desire to exploit and refine existing semiconductor simulation techniques in order to effectively study III-V HEMTs with feature sizes on the order of tens of nanometers. Modifications to well established semi-classical Monte Carlo techniques [20] have proven well suited for this task, as will be discussed in Section 1.2.

The versatility of the semi-classical Monte Carlo approach also permits in this work the simulation of spin-polarized transport in prototypical spintronic devices [21]. The field of spintronics, in which the quantum mechanical property of electron spin is used as a logic state [22,23,24,25], represents a fundamental paradigm shift from conventional electronics.

Fortuitously, the structure of a prototypical Spin Field Effect Transistor (SpinFET) [21] is actually an aggressively scaled variant of the aforementioned III-V HEMT structural scheme, and could perhaps become a viable technology in future decades beyond the existing "CMOS roadmap". In the prototypical SpinFET device conceived by Datta and Das in 1990 [21], the source and drain ends of the quasi 2D channel, in an otherwise standard HEMT-type device, act as source and detector, respectively, of spin-polarized electrons. As spin-polarized electrons traverse the channel, the presence of Rashba spin-orbit coupling [26] results in a precession of the electron spin vector about an effective magnetic field that is perpendicular to both the direction of transport and the electric field due to the gate. The magnitude of the spin-orbit interaction and corresponding rate of spin precession can be modulated via the usual "top" electrostatic gate. Consequently, the magnitude of the drain current is proportional to the degree of alignment of the electron spin and "drain" magnetic field.

The simplest conceptual means of achieving a polarized electron ensemble in the polarizing "source" is via dilute ferromagnetic semiconductor materials [27], or perhaps by electrical means using quantum point contacts (QPCs) [28, 29]. While this field is in its infancy, recent experimental work has in fact demonstrated the efficacy of the gate-controlled Rashba effect. [30,31,32].

1.2 Semi-classical Monte Carlo Simulation

Ideally, the simulation of carrier motion in semiconductor devices, either that of electrons or holes, requires the solution to what is fundamentally a many-body quantum mechanical problem. However, even with today's computer technology, obtaining such a many body, full quantum mechanical solution is intractable. Fortunately, for semiconductor devices whose critical dimensions are larger than those of the mesoscopic regime and which operate in ambient temperatures near or greater than room temperature (which is the case in most commercial applications), carrier transport can be described as being that of plasma of electrically charged point-like *particles*. This simplification often allows the utilization of particle-based computer simulation methods, such as the Monte Carlo (MC) technique, to accurately study the physics of carrier transport in semiconductors.

The justification for such a *semi-classical* approach is rooted in the Heisenberg Uncertainty Principle. Within the aforementioned constraints of feature sizes and temperature, the uncertainty in a carrier's momentum $\mathbf{p}$ and position $\mathbf{r}$ can be shown to be typically much less than the average momentum and the mean free path, respectively, of an ensemble of such carriers. Under these circumstances, the carrier can be considered to behave as a narrow wavepacket. The average momentum of a carrier ensemble is then given by the de Broglie relation as $\mathbf{p} = \hbar\mathbf{k}$, where $\mathbf{k}$ is the average wavevector of the ensemble. The mean free path is determined from the mean time between collisions, which is nearly equal to the inverse of the average scattering rate. It follows then that a simple calculation based on these assumptions reveals that at $T = 300\mathrm{K}$, and for carrier kinetic energies less than about 1.0eV, scattering occurs at a sufficiently low rate to satisfy the Uncertainty Principle and validate the semi-classical approach [33].

Therefore, the fundamental equation that typically needs to be solved in the semi-classical simulation of semiconductor devices is the Boltzmann Transport Equation (BTE). This equation describes the time-evolution of the carrier *distribution function,* $f(\mathbf{k},\mathbf{r})$ and is written as

$$\frac{\partial f(\mathbf{k},\mathbf{r})}{\partial t} = -\dot{\mathbf{r}} \cdot \nabla_{\mathbf{r}} f(\mathbf{k},\mathbf{r}) - \dot{\mathbf{k}} \cdot \nabla_{\mathbf{k}} f(\mathbf{k},\mathbf{r}) + \left(\frac{\partial f(\mathbf{k},\mathbf{r})}{\partial t} \right)_{collisions}, \quad (1.1)$$

where $f(\mathbf{k},\mathbf{r})$ represents the population distribution of carriers in six-dimensional phase-space, and the collision term in (1.1) is due to the relevant scattering processes. Knowledge of the distribution function as a function of time allows the determination of all physical quantities of interest such as currents, carrier energies, and densities.

No analytical solution exists to the BTE, except for a very narrow set of parameter constraints [34]. However, it has been proven that a Monte Carlo (MC) approach to the problem results in a numerical solution to the BTE [35], whose accuracy is only limited due to statistical error. Furthermore, the MC technique is superior in comparison to other semi-classical methods such as the Drift Diffusion (DD) or Hydrodynamic (HD) models, since these other approaches do not always capture the important transport physics, such as velocity overshoot in short channel devices [36].

Accordingly, since the inception of the Single Particle Monte Carlo (SPMC) technique in the 1960s to model transport in bulk semiconductors [37], the complexity of various MC techniques has increased steadily over the past four decades. By the 1980s, the Ensemble Monte Carlo (EMC) technique, a straightforward extension of the SPMC, was being widely used to simulate 3D transport in homostructure devices such as metal oxide field effect transistors (MOSFETs) and quasi-2D transport in heterostructure devices such as modulation doped field effect transistors (MODFETs) and high electron mobility transistors (HEMTs) [20,38,39,40,41,42,43].

By the 1990s, drastic improvements in computer memory technology made possible the development of Full Band EMC [44,45,46,47] and Cellular Monte Carlo (CMC) methods [33,48]. Unlike that of the SPMC or EMC methods, in the CMC the probabilities of scattering from any state to any other state are pre-tabulated and stored in random access memory (RAM) before the transport simulation begins. This procedure results in a demonstrated vast improvement in computational speeds in the simulation of MOSFET devices [33].

Since the 1990s and continuing to the present day, though, the continued scaling of semiconductor devices deep into the nanometer regime has made it crucial in MC modeling to accurately account for the effects of quantization in semiconductor nanostructures. Such effects can be very pronounced in the quantum well comprising the channel of a MODFET or HEMT, or at the Si-SiO_2 interface of silicon-based MOSFET, for example.

In retaining the well established semi-classical MC framework, various "quantum correction" techniques are used to treat such quantization issues. Amongst them are "effective potential" methods, such as the one due to Ferry [49], to account for such quantization effects such as interface charge-setback. Schrödinger-based solutions are also widely used, as noted in [50,51]. Additionally, the use of "quantum potentials" as corrective terms to the electrostatic potential has recently gained attention, along with continued research in increasingly complex Schrödinger-based approaches [52,53,54].

In this work, quantization is treated by applying an admixture of various "quantum corrections" such as periodic SWE updates over the entire real-space simulation domain, usage of "2D contacts", and the initialization of carrier attributes in a manner consistent with the proper quantum mechanical density and energy distribution.

Also in this work, the D'yakanov-Perel spin-density matrix formalism is utilized within the framework of a self-consistent EMC simulation of a SpinFET. In doing so, real-space boundary conditions are imposed over the entire simulation domain. These conditions, while simultaneously accounting for the spatial variation of the spin-density matrix spin-orbit parameters, represent an original contribution to the field of study.

1.3 Dissertation Organization

Successive chapters of this dissertation are organized as follows. In Chapter 2, the derivations of the scattering mechanisms included in the EMC developed in this work are delineated. In Chapter 3, the EMC Algorithms are explained in detail. In Chapter 4, simulation results are presented for the current voltage characteristics of an InGaAs/InAlAs HEMT, corresponding to nanoscale III-V HEMTs currently being fabricated by Intel Corporation. Additionally, in Chapter 4, results are presented for prototypical SpinFET simulations, in which spin-polarized carriers are injected at an "ideal" polarizing source, and the coherence length is studied as a function of gate voltage via the Rashba effect. Finally, a summary and intent of future work is given in Chapter 5.

2. Carrier Scattering Mechanisms

2.1 Overview

Carrier motion within the crystalline structure of a semiconductor is governed by the Bloch Theorem. This theorem states that in the presence of a periodic potential the carrier's wavefunction can be written in the form of a plane wave modulated by a cell periodic component. Thus, within the single particle model, the solutions to the Schrödinger wave equation (SWE) that describe the carrier motion are of the functional form

$$\Psi_{n,\mathbf{k}}(\mathbf{r}) = u_{n,\mathbf{k}}(\mathbf{r}) e^{i\mathbf{k}\cdot\mathbf{r}}, \tag{2.1}$$

which are known as Bloch functions. In (2.1), $\mathbf{k}$ and $\mathbf{r}$ denote the wavevector and real-space position vector, respectively, and n denotes the band index of the cell periodic function, $u_{n,\mathbf{k}}(\mathbf{r})$.

For particle motion in an *ideal* periodic potential, no scattering occurs. In actuality, though, the periodicity of the crystal potential is disrupted by random perturbing potentials, which form the basis of the quantum mechanical scattering mechanisms that may alter a carrier's momentum and kinetic energy.

In this work, scattering mechanisms relevant for carrier motion in bulk III-V semiconductor materials are used, both 3D as well as the relevant 2D mechanisms for carrier transport that occurs in the quasi two-dimensional electron gas that is formed in the quantum well comprising the channel of a semiconductor heterostructure. These scattering mechanisms account for the presence of phonons (the quantized vibrations of the crystal lattice), the random fluctuation in the periodic potential in the presence of ternary semiconductor alloys, the surface roughness that exists at the interfaces of the various material layers in a heterostructure, and the presence of ionized impurities in each material layer. Electron-electron and plasmon scattering have not been considered as part of the present work.

Phonon scattering is the dominant mechanism in III-V compounds at $T = 300\mathrm{K}$ and consists, in general, of optical and acoustic modes. Optical phonons exist due to the two dissimilar atoms in the unit cell that oscillate about their equilibrium positions within the crystal lattice, out of phase with each other. For acoustic phonon modes, on the other hand, the oscillations of the atoms are in phase with each other. This results in the relative displacement of the atoms about their equilibrium sites being the same everywhere. Hence, in that case, induce strain is the physical quantity of interest that results in a perturbation to the potential.

2.2 Fermi's Golden Rule

The transition rate, i.e., the scattering rate, per unit time of a carrier in state $\Psi(\mathbf{k},\mathbf{r})$ to a state $\Psi(\mathbf{k}',\mathbf{r})$ (where the index n has been dropped for simplicity) due to a perturbation of the Hamiltonian of magnitude H', is given, within first-order, time dependent perturbation theory as

$$S(\mathbf{k}',\mathbf{k}) = \frac{2\pi}{\hbar} \left| \langle \mathbf{k}' | H' | \mathbf{k} \rangle \right|^2 \delta\left(E_{\mathbf{k}'} - E_{\mathbf{k}} \mp \hbar\omega\right) \ , \tag{2.2}$$

where the Dirac bra and ket variables $\mathbf{k}$ and $\mathbf{k}'$ denote the corresponding state vectors. The Kronecker delta function δ in (2.2) enforces conservation of energy between the initial and final energy states, $E_{\mathbf{k}}$ and $E_{\mathbf{k}'}$, respectively, accounting for the emission or absorption of a phonon of energy $\hbar\omega$ in the scattering process, where $\hbar$ is the Planck constant and ω denotes the phonon frequency. This famous result is known as the Fermi Golden Rule. It is important to note that (2.2) assumes that momentum scattering occurs instantaneously, and that the real-space position of the particle remains constant during the collision.

The particular form of H' depends on the relevant scattering mechanism in question for the material of interest, and will be discussed in subsequent subsections of this chapter. Furthermore, the form of the Bloch function as given by (2.1) needs to be modified if the motion of the particle is dimensionally restricted due to quantization in a particular direction in the device, as occurs in semiconductor heterostructures, as discussed in Section 2.4.

2.3 3D Scattering Mechanisms

Since the perturbing potentials associated with the aforementioned mechanisms are time-harmonic and of the form [55]

$$H'(t) = H'e^{\mp i\omega t} \quad , \tag{2.3}$$

each perturbing potential can be expanded into a Fourier series as

$$H' = \sum_{\mathbf{q}} U_{\mathbf{q}} e^{i\mathbf{q}\cdot\mathbf{r}} \quad . \tag{2.4}$$

Substituting the Bloch function (2.1) and (2.4) into the matrix element within (2.2) and recognizing that the periodicity of the exponential term yields a non-zero result for the matrix element only when $\mathbf{k}' = \mathbf{k} \pm \mathbf{q}$ gives

$$\left|\langle \mathbf{k}' | H' | \mathbf{k} \rangle\right| = U_{\mathbf{k}'-\mathbf{k}} I(\mathbf{k},\mathbf{k}') \quad , \tag{2.5}$$

where

$$U_{\mathbf{k}'-\mathbf{k}} = \int_{\Omega} e^{-i\mathbf{k}'\cdot\mathbf{r}} U(\mathbf{r},t) e^{i\mathbf{k}\cdot\mathbf{r}} d\mathbf{r} \quad , \tag{2.6}$$

$$I(\mathbf{k},\mathbf{k}') = \int_{\Omega} u^{*}_{\mathbf{k}'}(\mathbf{r}) u_{\mathbf{k}}(\mathbf{r}) d\mathbf{r} \quad , \tag{2.7}$$

with the range of integration being that of the crystal volume, Ω. The factor $I(\mathbf{k},\mathbf{k}')$ defines an overlap integral and is only valid provided that the spatial variation of H' occurs slowly compared to the cell periodic component of the Bloch function. For the case of conduction bands arising from s-like orbitals and assuming spherical and parabolic bands, $I(\mathbf{k},\mathbf{k}') \approx 1.0$ [55].

The total scattering rate from state $\mathbf{k}$, as a function of kinetic energy, is then deduced by inserting (2.5) into (2.2) and integrating (2.2) over all $\mathbf{k}'$ states that satisfy momentum and energy conservation requirements. In doing this, one must determine the total number of possible final states contained within a k-space cell of volume $\mathrm{d}\mathbf{k}'$ about the point $\mathbf{k}'$ by utilizing the appropriate expression for the density of states. In this work, the non-parabolic 3D density of states is utilized for all scattering mechanisms (unless otherwise noted):

$$N(E_k) = \left(2m^{*}\right)^{3/2} \gamma^{1/2}(E_k) \frac{d\gamma(E_k)}{dE_k} \quad , \tag{2.8}$$

where

$$\gamma(E_k) = \frac{\hbar^2 k^2}{2m^{*}} = E_k\left(1+\alpha E_k\right) \quad , \tag{2.9}$$

is the Kane expression [56] describing the non-parabolic dispersion. The non-parabolicity factor is determined from **k.p** theory and is given as

$$\alpha = \frac{1}{E_g}\left(1-\frac{m^*}{m_o}\right)^2 \quad , \tag{2.10}$$

where E_g is the material bandgap and m^* is the effective mass at the band extrema. For the conduction bands of the III-V compounds of interest, those are those are the Γ, L, X valley k-space points.

Using the aforementioned prescription, the scattering mechanisms for the relevant 3D scattering mechanisms in III-V compounds, expressed as a function of kinetic energy, are well known and presented next without rigorous proof.

2.3.1 3D Polar Optical Phonon Scattering

In III-V compounds, polar optical phonon scattering results from the dipole moment formed by the ionic bond that exists between the two dissimilar atoms that compose the unit cell of the crystal structure. It is a dominant inelastic scattering mechanism in III-V compounds at room temperature.

The perturbing potential that induces the longitudinal lattice vibrations within the crystal has been derived by Frölich and is given as

$$\mathbf{H}' = -eU(\mathbf{r}) \quad , \tag{2.11}$$

where e is the electronic charge and $U(\mathbf{r})$ is an effective electrostatic potential. $U(\mathbf{r})$ is proportional to the relative, instantaneous displacement of the atoms about their equilibrium positions and is given as [13]

$$U(\mathbf{r}) = -i\frac{N}{\Omega}\cdot\frac{e^*}{q\varepsilon_\infty}\mathbf{u}(\mathbf{r}) \quad , \tag{2.12}$$

where N is the number of dipoles in the crystal, Ω is the crystal volume, ε_∞ is the high frequency permittivity, q is the magnitude of the phonon wavevector, e^* is the effective charge due to Frölich, and $\mathbf{u}(\mathbf{r})$ is the relative displacement of the atoms about their equilibrium positions. In (2.12), $\mathbf{u}(\mathbf{r})$ is written as [53],

$$\mathbf{u}(\mathbf{r}) = \sum_{\mathbf{q}} \left(\frac{\hbar}{2NM\omega_o} \right)^{1/2} \mathbf{e}_{\mathbf{q}} \left(a_{\mathbf{q}} + a_{-\mathbf{q}}^{+} \right) e^{i\mathbf{q}\cdot\mathbf{r}} \quad . \tag{2.13}$$

In (2.13), the summation is over all phonon wavevectors (modes) $\mathbf{q}$, and the approximation is made that all wavevectors are associated with the constant angular frequency ω_o. In this expression the unit polarization vector is $\mathbf{e}_{\mathbf{q}}$ and $a_{-\mathbf{q}}^{+}$ and $a_{\mathbf{q}}$ are the quantum mechanical raising and lowering operators, respectively. The Frölich effective charge, e^*, in (2.12) is written

$$e^* = \left(\frac{\Omega M}{N} \right)^{1/2} \omega_o \varepsilon_\infty \left(\frac{1}{\varepsilon_\infty} - \frac{1}{\varepsilon_s} \right)^{1/2} \quad . \tag{2.14}$$

Using the aforementioned form of the interaction potential and following the procedure delineated in section (2.3) Fawcett and Swain [35] have derived an expression for 3D polar optical phonon scattering, in which they account for a non-parabolic $E(\mathbf{k})$ dispersion. The scattering rate is given as,

$$W(E_k) = \frac{em^{*1/2}\omega_o}{\sqrt{2}\hbar} \left(\frac{1}{\varepsilon_\infty} - \frac{1}{\varepsilon_o} \right) \frac{(1 + 2\alpha E_{k'})}{\gamma^{1/2}(E_k)} \left(N_o(\omega_o) + \frac{1}{2} \mp \frac{1}{2} \right) F_o(E_k, E_{k'}) \quad . \tag{2.15}$$

In (2.15), the requirement that $E_{k'} = E_k \pm \hbar\omega_o$ ensures conservation of energy. The kinetic energy of the carrier after the collision is either lowered or raised by an amount equal to $\hbar\omega_o$ for the emission or absorption of a phonon, respectively. Momentum is conserved since $\mathbf{k}' = \mathbf{k} \pm \mathbf{q}$. This result also assumes that the phonons are bulk-like, as opposed to existing in confined modes [57], and dispersionless with a constant frequency denoted by ω_o. The function

$$N_o(\omega_o) + \frac{1}{2} \mp \frac{1}{2} = \frac{1}{\exp(\hbar\omega_o / k_B T) - 1} + \frac{1}{2} \mp \frac{1}{2} \quad , \tag{2.16}$$

is the Bose-Einstein distribution function which denotes the phonon occupancy factor for the mode $\mathbf{q}$ at angular frequency ω_o, where the upper sign is for absorption and the bottom for emission. Finally, the last term of (2.15) is given as

$$F_o(E_k, E_{k'}) = C^{-1}\left(A \ln\left| \frac{\gamma^{1/2}(E_k) + \gamma^{1/2}(E_{k'})}{\gamma^{1/2}(E_k) - \gamma^{1/2}(E_{k'})} \right| + B \right) \quad , \tag{2.17}$$

where

$$A = \left[2(1 + \alpha E_k)(1 + \alpha E_{k'}) + \alpha\{\gamma(E_k) + \gamma(E_{k'})\}\right]^2 \ , \tag{2.18}$$

$$B = -2\alpha\gamma(E_k)^{1/2}\gamma(E_{k'})^{1/2}\left[4(1 + \alpha E_k)(1 + \alpha E_{k'}) + \alpha\{\gamma(E_k) + \gamma(E_{k'})\}\right] \ , \tag{2.19}$$

$$C = 4(1 + \alpha E_k)(1 + \alpha E_{k'})(1 + 2\alpha E_k)(1 + 2\alpha E_{k'}) \ , \tag{2.20}$$

and

$$\gamma(E_k) = \frac{\hbar^2 k^2}{2m^*} = E_k(1 + \alpha E_k) \quad . \tag{2.21}$$

Since the dipole moment of the Frölich interaction is directional in nature, it can be shown that small angle scattering is favored. This type of scattering is therefore highly anisotropic. However, since the probability of scattering through some angle θ is a monotonically increasing function of the angle θ, a random number r can be utilized to select the scattering angle. The result [35] is given as

$$\cos\,\theta = \frac{1 + f - (1 + 2f)^r}{f} \quad , \tag{2.22}$$

where

$$f = \frac{2\sqrt{E_k E_{k'}}}{\left(\sqrt{E_k} - \sqrt{E_{k'}}\right)^2} \quad . \tag{2.23}$$

It is imperative to recognize that the angle θ denotes the polar angle between the initial and final wavevectors, but that the azimuthal angle must still be chosen at random, since spherical symmetry exists about the azimuthal direction.

2.3.2 3D Acoustic Deformation Potential Scattering

As mentioned in section (2.1), the physical quantity of interest in this case is the interaction potential resulting from the induced strain. Hence,

$$H'(\mathbf{r},t) = \Xi_d \,\nabla \cdot \mathbf{u}(\mathbf{r},t) \quad , \tag{2.24}$$

where Ξ_d denotes the acoustic deformation potential and $\mathbf{u}(\mathbf{r},t)$ is given as

$$\mathbf{u}(\mathbf{r},t) = \sum_{\mathbf{q}} \left(\frac{\hbar}{2\rho\Omega\omega_{\mathbf{q}}} \right)^{1/2} \mathbf{e}_{\mathbf{q}} \left(a_{\mathbf{q}} + a^{+}_{-\mathbf{q}} \right) e^{i\mathbf{q}\cdot\mathbf{r}} \quad , \tag{2.25}$$

where the summation is over all phonon wavevectors (modes) $\mathbf{q}$ at angular frequency $\omega_{\mathbf{q}}$. In this expression the crystal volume is given as Ω, $\mathbf{e}_{\mathbf{q}}$ is the unit polarization vector, and $a^{+}_{-\mathbf{q}}$ and $a_{\mathbf{q}}$ are the quantum mechanical raising and lowering operators, respectively.

At $T = 300K$, $\hbar\omega << k_B T$ so that one can make the equipartition approximation that $N_o(\omega_o) \approx \dfrac{k_B T}{\hbar\omega_o}$ which implies that $N_o(\omega_o) \approx N_o(\omega_o) + 1$ and $\hbar\omega \approx 0$. The approximation can therefore be made that the scattering is elastic. The resulting scattering rate is

$$W(E_k) = \frac{2\pi\,\Xi^2 k_B T_L}{\hbar c_L} N(E_k) \frac{(1+\alpha E_k)^2 + \frac{1}{3}(\alpha E_k)^2}{(1+2\alpha E_k)^2} \quad , \qquad (2.26)$$

where T_L is the lattice temperature, and c_L is the material dependent elastic constant defined as $c_L = \rho v_s^2$ where ρ is the mass density and v_s is the velocity of sound in the material (the velocity of sound can also be expressed as ω_q / q). In this case, the 3D density of states for a carrier in a non-parabolic band is given as

$$N(E_k) = (2m^*)^{3/2} \gamma^{1/2}(E_k) \frac{d\gamma(E_k)}{dE_k} \quad , \qquad (2.27)$$

where γ is the Kane factor given by (2.9).

In spherical and parabolic bands, the acoustic deformation potential scattering is isotropic and the final wavevector can be chosen at random since all scattering angles are equally probable. Although the scattering is not strictly isotropic in the case of non-parabolic bands, this approximation is retained in the final state selection in the EMC model.

2.3.3 3D Non-Polar Optical Scattering

Unlike the case of acoustic deformation potential scattering where induced strain is of importance, here the interaction potential is proportional to the displacement, as in the polar optical case. Also, the higher optical frequencies involved in the interaction result in phonon energies on the order of the thermal energy. Hence, the scattering must be considered inelastic. This implies that the thermodynamic approximations used for the acoustic case cannot be used.

Therefore, for non-polar optical phonons near the zone center the interaction potential is given as

$$H'(\mathbf{r},t) = \mathbf{D_o} \cdot \mathbf{u}(\mathbf{r},t) \quad . \tag{2.28}$$

Additionally, near the edge of the Brillouin zone, the non-polar optical phonons that contribute to intervalley scattering are at slightly lower energies (on the order of a few meV) than those at the zone center. Accordingly, a valley dependent deformation potential $\mathbf{D}_{ij}$ between the valleys i and j must be employed near the edge of the zone instead of using $\mathbf{D_o}$.

Using the same index scheme for the intra and inter-valley cases, the resulting scattering rate from the ith to the jth valley is

$$W(E_k) = \frac{Z_j \pi D_{ij}^2}{\rho \omega_{ij}} \left(N_o(\omega_o) + \frac{1}{2} \mp \frac{1}{2} \right) N(E_{k'}) F_{ij}(E_k, E_{k'}) \quad , \tag{2.29}$$

where

$$E_{k'} = E_k \pm \hbar\omega_o - \Delta E_{ji} \quad . \tag{2.30}$$

In (2.30), ΔE_{ji} and ω_{ij} denote the energy offset and intervalley phonon frequency, respectively, between the ith and jth valleys in the 3-valley model employed. Z_j denotes the number of equivalent j valleys due to crystal symmetry and ρ is the mass density. $N(E_{k'})$ is the density of final states, defined as in (2.8). The last term of (2.29) is given as

$$F_{ij}(E_k, E_{k'}) = \frac{(1+\alpha_i E_k)(1+\alpha_j E_{k'})}{(1+2\alpha_i E_k)(1+2\alpha_j E_{k'})} \quad . \tag{2.31}$$

2.3.4 3D Ionized Impurity Scattering

In highly doped semiconductors (doping density greater than ~10^{17}/cm^3), the resulting ionized impurities create coulombic potentials that scatter the carriers. These potentials are screened by the free carriers in the vicinity of the ions. A screening model that is typically used, which is employed here, is the Brooks-Herring model. In this scheme, the screened perturbation potential is given by

$$V(r) = \frac{Zen_o}{4\pi\varepsilon_s r} e^{-q_D r} \quad , \tag{2.32}$$

where Ze denotes the charge of the ion, r the distance of the carrier from the ion, and n_o is the equilibrium density (i.e., the density of free carriers that would exist in the vicinity of the impurity if it were not ionized) . The screening factor, q_D, is taken as the Debye wavevector given by

$$q_D = \sqrt{\frac{e^2 n_o}{\varepsilon_s k_B T}} \quad . \tag{2.33}$$

Multiplying (2.32) by the electronic charge e yields the perturbating Hamiltonian

$$H' = \frac{Ze^2 n_o}{4\pi\varepsilon_s r} e^{-q_D r} \quad . \tag{2.34}$$

The resulting scattering rate, from Fermi's Golden Rule, is

$$W(E_k) = \frac{2\pi N_i Z^2 e^4}{\hbar \varepsilon_s^2} N(E_k) \frac{1}{q_D^2 \left(4k^2 + q_D^2\right)} \quad , \tag{2.35}$$

which is valid within the Brooks-Herring model so long as q_D in the denominator of (2.35) is large enough so that the scattering rate does not diverge. It is important to note that while the non-parabolicity of the density of states is taken into consideration, the overlap integral of (2.7) has been ignored in this case.

As was the case for polar optical scattering, ionized impurity scattering is anisotropic and the probability of scattering through some angle θ is a monotonically increasing function of the angle θ. Therefore, a random number r can be utilized to select the scattering angle. In this case [20],

$$\cos\,\theta = \frac{1 - 2r}{1 + (1 - r)\left(\frac{2k}{q_D}\right)^2} \quad . \tag{2.36}$$

2.3.5 3D Alloy Scattering

The introduction of alloys to pure III-V compounds results in additional disruption to the periodic potential. In this work the scattering rate discussed in [20] is employed. It is written (for the case $S = 1$ in [58]),

$$W(E_k) = \frac{3\pi}{8\sqrt{2}} \frac{\left(m^*\right)^{3/2}}{\hbar^4} [x(1 - x)][\gamma(E)]^{1/2} \frac{d\gamma(E)}{dE} \Omega |\Delta V|^2 \quad , \tag{2.37}$$

where x is the molar fraction, the volume of the unit cell Ω is given by $\left(a_o^3/4\right)$ where a_o is the lattice constant, and ΔV characterizes the strength of the perturbing potential.

2.4 2D Scattering Mechanisms

In the single band *effective mass approximation*, the Bloch function, (2.1), needs to be modified so that the component of the wavefunction in the quantized direction assumes the form of an envelope function. The modified Bloch function is then written

$$\Psi_{n,\mathbf{k}_{/\!/}}(\mathbf{r}) = u_{n,\mathbf{k}}(\mathbf{r})\varphi_i(z)e^{i\mathbf{k}_{/\!/}\cdot\mathbf{r}_{/\!/}} \quad , \tag{2.38}$$

where $\varphi_i(z)$ is the solution of the one-dimensional effective-mass equation with respect to the direction of quantum confinement. This corresponds to the heterostructure growth direction for the systems under consideration in this work, unless otherwise noted. The effective mass equation is written,

$$\left(\frac{\hbar^2}{2m_z^*}\frac{\partial^2}{\partial^2 z} + V_c(z) - E_i\right)\varphi_i(z) = 0 \quad . \tag{2.39}$$

In (2.39), $V_c(z)$ is the potential energy due to the combined effect of the electrostatic potential and the material potential energy offsets of the semiconductor heterostructure.

Since the confinement potential in a device will vary as a function of the in-plane position vector, an accurate treatment of the problem requires a calculation of scattering rates for each in-plane device coordinate. Furthermore, a more accurate treatment of 2D phonon scattering requires that phonon modes be treated as confined, due to boundary conditions being imposed upon the displacement vector. In this work, however, bulk phonons are assumed in all 2D scattering mechanisms. The justification for this is that the quantum well structures remain in intimate contact with the substrate [59].

Inserting (2.38) into $\left|\langle \mathbf{k}' | H' | \mathbf{k} \rangle\right|$ in lieu of the Bloch function given by (2.1), equations (2.5)-(2.7) become modified to account for the quantization such that

$$\left|\langle n', \mathbf{k}' | H' | n, \mathbf{k} \rangle\right| = \int_{\Omega} \varphi_{n'}(z) e^{-i\mathbf{k}'\cdot\mathbf{r}} H' \varphi_n(z) e^{i\mathbf{k}\cdot\mathbf{r}} d\mathbf{r} \quad . \tag{2.40}$$

Substituting (2.40) into a modified form of (2.2), to account for the band indexing, the integration over the exponential terms results in the matrix element being equal to zero for all values of $q_{//}$ except the one for which $\pm q_{//} = k'_{//} - k_{//}$, analogous to the 3D case. However, the summation over the q_z components of the phonon wavevector remains in the matrix element. Thus,

$$\left|\langle n', \mathbf{k}' | H' | n, \mathbf{k} \rangle\right| = U' \int_{-\infty}^{\infty} \varphi_{n'}(z) \left(\sum_{q_z} e^{iq_z z} \right) \varphi_n(z) dz \quad , \tag{2.41}$$

where U' is the pre-factor of the perturbing potential. This equation is typically re-written as

$$\left|\langle n', \mathbf{k}' | H' | n, \mathbf{k} \rangle\right| = \sum_{q_z} G_{n',n}(q_z) \quad , \tag{2.42}$$

where

$$G_{n',n}(q_z) = \int_{-\infty}^{\infty} \varphi_{n'}(z) e^{iq_z z} \varphi_n(z) dz \quad , \tag{2.43}$$

defines the *overlap integral* between the initial and final envelope functions.

Inserting (2.42) into Fermi's Golden Rule, and evaluating the square of the matrix element is not a straightforward process though, due to the summation over q_z in (2.42). Fortunately, however, the summation over q_z can be transformed to one over z [59, 60] allowing one to obtain expressions for the 2D scattering rates that are easily evaluated numerically.

The 2D scattering mechanisms presented in the following sections were derived utilizing the aforementioned $q_z \to z$ transformation. Additionally, the band structure is assumed to be spherical and parabolic for each 2D mechanism presented. While this assumption of spherical and parabolic bands is clearly invalid at high kinetic energies, these scattering rates are only used for carriers in the Γ valley in k-space; a regime where the energies are typically less than $\approx 0.5\text{eV}$, the order of magnitude for the upper valley energy gaps in III-V compounds. 2D scattering rates for non-parabolic bands have been utilized by other researchers [50] and will be included in future modifications to this work.

2.4.1 2D Polar Optical Scattering

As was the case for the 3D scattering mechanism, the unscreened Frölich interaction is utilized. The intra-valley scattering rate from the ith to the jth subband is then given by [61],

$$W_{i,j}(E_k) = \frac{m^* e^2 \omega_o}{8\pi\hbar^2} \left(\frac{1}{\varepsilon_\infty} - \frac{1}{\varepsilon_s} \right) \left(n_{\omega_o} + \frac{1}{2} \mp \frac{1}{2} \right) \int_0^{2\pi} d\theta \, \frac{H_{ij}(q_\pm)}{q\pm} \quad , \qquad (2.44)$$

where the top signs on the right are for phonon absorption and the bottom signs for phonon emission. The overlap integral is

$$H_{ij}\left(q_{\pm}\right)=\int_{-\infty}^{\infty}dz\int_{-\infty}^{\infty}dz'\rho_{ij}\left(z\right)\rho_{ij}^{*}\left(z'\right)e^{-q_{\pm}\left|z-z'\right|} \quad , \tag{2.45}$$

where

$$\rho_{ij}\left(z\right)=\varphi_{i}^{*}\left(z\right)\varphi_{j}\left(z\right) \quad . \tag{2.46}$$

It can be readily verified that conservation of momentum and energy is insured by the following expression for $q\pm$,

$$q_{\pm}=\left|\vec{k}-\vec{k}'\right|=\left[2k^{2}\pm\frac{2\omega_{ij}^{*}m^{*}}{\hbar}-2k\left(k^{2}\pm\frac{2\omega_{ij}^{*}m^{*}}{\hbar}\right)^{1/2}\cos\theta\right]^{1/2} \quad . \tag{2.47}$$

In this expression $\hbar\omega_{ij}^{*}=\hbar\omega_{o}\pm\left(E_{i}-E_{j}\right)$ and the initial and final subband energies are given by E_{i} and E_{j}, respectively.

With regard to final state selection after scattering, the anisotropic nature of 2D polar optical scattering favors small angle scattering as in the 3D case. To determine the scattering angle, a random number r is first chosen and then compared to the probability of scattering to some angle θ, as θ is varied from 0 to 2π. Those probabilities are determined by tabulating the normalized integrand of (2.44) for each angle θ from 0 to 2π in increments of $d\theta$. As soon as an angle is found whereby the random number r is less than the probability of scattering to that angle θ, that particular angle is chosen. Further details of final state selection are discussed in Chapter 3.

2.4.2 2D Acoustic Phonon Scattering

In this case, thermodynamic approximations of the 3D case are retained, and the scattering is therefore treated as elastic. The scattering rate is found to be [21]:

$$W_{i,j}\left(E_k\right) = \frac{m^* k_B T\, \Xi_{i,j}^2}{\hbar^3 \rho v_s^2} \int_{-\infty}^{\infty} dz\, \Phi_{i,j}^2(z) \quad . \tag{2.48}$$

where $\Phi_{i,j}(z) = \varphi_i^*(z)\varphi_j(z)$, ρ is the mass density and v_s is the velocity of sound. In selecting the final state, the scattering is assumed to be isotropic.

2.4.3 2D Non-Polar Optical Scattering

The treatment is analogous to the 3D case. The scattering rate requires a summation over the number of equivalent valleys v_f and is written [60]

$$W_{v_i,i,j}\left(E_k\right) = \sum_{v_f} m_{v_f,j}^* \,\frac{D_{v_i,v_f,i,j}^2 \left(n_{\omega_{v_i,i}} + \frac{1}{2} \mp \frac{1}{2} \right)}{2\rho \omega_{v_i,i} \hbar^2} \int_{-\infty}^{\infty} dz \left|\varphi_{v_i,i}^2(z)\right| \left|\varphi_{v_f,j}^2(z)\right| \quad , \tag{2.49}$$

where the upper sign on the right side is for phonon absorption, and the lower sign for phonon emission. As in the 3D case, the scattering is considered to be isotropic. Also, although effective masses and deformation potentials are specified for each valley/subband transition, these quantities in the upper valleys are often difficult to determine experimentally, and approximations based on the values for the Γ valley are used as needed.

2.4.4 2D Interface Roughness Scattering

The material interfaces of a semiconductor heterostructure are never "perfectly smooth" due to lattice mismatch and fabrication process tolerances.

This "roughness" is characterized by local fluctuations in the heterostructure confinement potential that serve to disrupt the periodic potential of the ideal crystal. These potential fluctuations are the basis of the perturbation to the ideal Hamiltonian.

In this work, only the interface roughness that exists at the barriers between the quantum well channel of the heterostructure is considered, using the theory developed in [61]. The situation for a single interface is depicted in Figure (2.1).

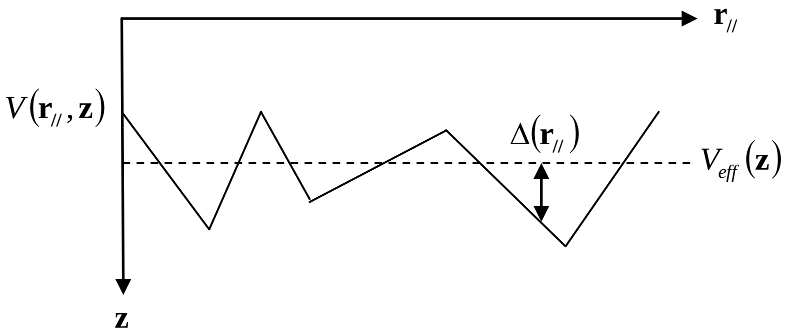

Figure 2.1 Schematic depiction of interface roughness in a semiconductor heterointerface.

Expanding the actual 2D confinement potential $V(\mathbf{r}_{//}, z)$ about the ideal potential $V_{eff}(z)$ at each $\mathbf{r}_{//}$, a perturbing roughness potential can be defined as,

$$V^{SR}(\mathbf{r}_{//}, z) = V_{eff}(z + \Delta(\mathbf{r}_{//})) - V_{eff}(z) \cong \Delta(\mathbf{r}_{//}) \frac{\partial V_{eff}(z)}{\partial z} \quad . \tag{2.50}$$

After multiplying by the electronic charge to obtain the proper energy perturbation in the Hamiltonian, (2.50) is inserted into (2.42) to obtain

$$\left\langle \psi_{n',\mathbf{k}'_{//}} \left| eV^{SR}\left(\mathbf{r}_{//}, z\right) \right| \psi_{n,\mathbf{k}_{//}} \right\rangle = e\int_{-\infty}^{\infty} dr\, e^{i\left(\mathbf{k}_{//} - \mathbf{k}'_{//}\right)\cdot\mathbf{r}_{//}} \Delta\left(\mathbf{r}_{//}\right) \int_{-\infty}^{\infty} dz\ \varphi_{n'}^{*}(z) \frac{\partial V_{eff}(z)}{\partial z} \varphi_n(z)$$

$$= e\Delta(q) F_{avg}^{n,n'} \quad , \tag{2.51}$$

where

$$F_{avg}^{n,n'} = \int_{-\infty}^{\infty} dz\ \varphi_{n'}^{*}(z) \frac{\partial V_{eff}(z)}{\partial z} \varphi_n(z) \quad , \tag{2.52}$$

takes the form of an average electric field in the quantum well and,

$$\Delta(q) = \int_{-\infty}^{\infty} dr\, e^{i(k-k')\cdot r} \Delta(r) \quad , \tag{2.53}$$

where $q = k - k'$, and $\Delta(q)$ is the Fourier transform of $\Delta(r)$. Therefore, when the square of the matrix element is determined, the resulting function $S(q) = \left|\Delta(q)\right|^2$ can be interpreted as the power spectrum of the roughness fluctuations, when a sum over all q (equivalently all $\mathbf{k}'$) is performed.

As first shown by Goodnick [61], the associated autocovariance function takes the form of an exponential. This implies that

$$S(q) = \frac{\pi \Delta^2 L^2}{\left[1 + q^2 L^2 / 2\right]^{3/2}} \quad , \tag{2.54}$$

where the parameters Δ and L are known as the rms roughness height and correlation length, respectively. Assuming parabolic bands, it is then straightforward to evaluate the scattering rate as,

$$W_{n,n'}(E_k) = \frac{e^2 \left| F_{avg}^{n,n'} \right|^2 m^*}{2\pi\hbar^3} \int_0^{2\pi} d\theta \; S(q) \quad , \tag{2.55}$$

where $q = 2k\sin(\theta/2)$ and $q = 2k\sin(\theta/2)$.

2.4.5 2D Alloy Scattering

In this case the interaction potential is the same, naturally, as in the 3D case. Hence, a straightforward extension of the 3D formalism, using the 2D density of states yields [62]

$$W_{n,n'}(E_k) = \frac{m^* x(1-x)}{\hbar^3} \left(\frac{a_o^3}{4} \right) |\Delta V|^2 \int_{-\infty}^{\infty} dz \left| \varphi_n^2(z) \right| \left| \varphi_{n'}^2(z) \right| \quad , \tag{2.56}$$

where x is the molar fraction, and the volume of the unit cell is given by $(a_o^3/4)$ where a_o is the lattice constant.

2.5 Plots of 2D Scattering Rates

In this section plots of the 2D scattering rates, as a function of kinetic energy, are presented for each previously discussed 2D scattering mechanism for a 13nm $In_{0.7}Ga_{0.3}As$ quantum well bound by $In_{0.52}Al_{0.48}As$ cladding layers (The structure is exactly as depicted in Figure 4.3 under the gate region of the Intel HEMT device). In these results, a mean effective mass was determined, based on the effective masses of the indivdual heterostructure layers, weighted by the quantum mechanical probability (square of the envelope functions) of the carrier "residing" within a particular layer. In turn, the effective masses of the alloys of InAs and GaAs were taken as a linear interpolation from those of the pure compounds, $0.036m_o$ and $0.067m_o$ respectively. Accordingly, the effective mass in this case was $\approx 0.04 m_o$. In each of the following plots, four subbands were included in plotting the scattering rate "out" of the first subband to, to all other subbands. The choice of using four subbands was based upon the assumed conduction band offset of $\Delta E_c = 0.50\text{eV}$ between the $\text{In}_{0.7}\text{Ga}_{0.3}\text{As}$ and by $\text{In}_{0.52}\text{Al}_{0.48}\text{As}$ cladding layers. In all cases, $T = 300\text{K}$.

In Figure 2.2, the 2D polar optical phonon scattering rates are plotted for both absorption, emission, and the combined rate. As expected from the dependence on the inverse of $q\pm$ in (2.44) the overall scattering rate decreases as the energy increases. The "jumps" in the curve indicate that additional states are available for scattering, when inter-subband transitions are allowed, as dictated by conservation of momentum and energy requirements.

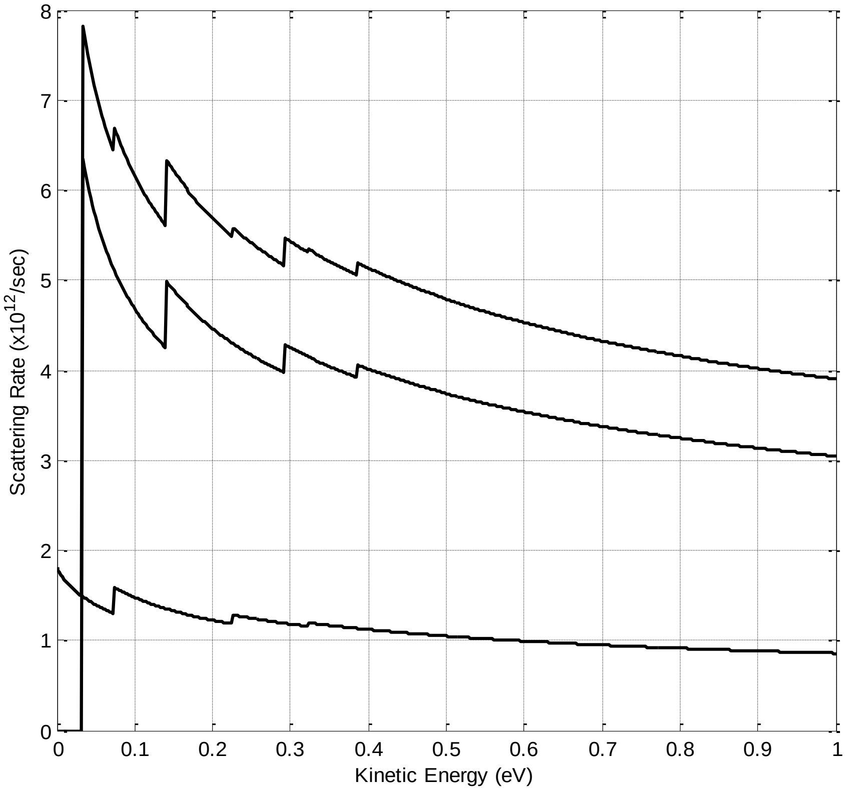

Figure 2.2 Polar optical 2D phonon scattering for a 13nm $In_{0.7}Ga_{0.3}As$ quantum well bound by $In_{0.52}Al_{0.48}As$ cladding layers, as discussed in the text; Bottom curve: Absorption rate; Middle curve: Emission rate; Top curve: Emission + Absorption.

In Figure 2.3, the 2D acoustic phonon scattering rate is plotted. Unlike the case of polar optical scattering, the scattering is considered to be elastic in this case and the "flat" step-like dependence of the scattering rate is indicative of the constant 2D density of states. In this case, inter-subband transitions are allowed when conservation of energy permits such transitions. i.e., when

$$E_{k,i} + E_{sub,i} = E_{k,f} + E_{sub,f} \ .$$

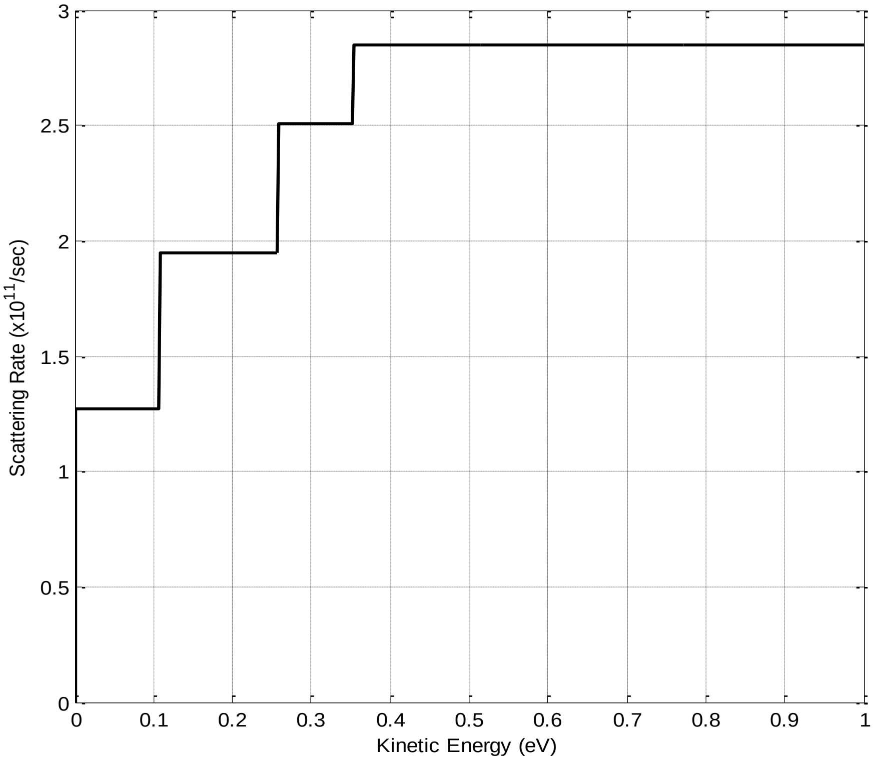

Figure 2.3 Acoustic 2D phonon scattering rate for a 13nm $In_{0.7}Ga_{0.3}As$ quantum well bound by $In_{0.52}Al_{0.48}As$ cladding layers, as discussed in the text.

In Figure 2.4, the 2D non-polar optical scattering rate that contributes to intervalley scattering from the 1st subband of the Γ valley to the L valley subbands is plotted for both the emission and absorption cases. In doing this the four equivalent final valleys are considered, as indicated in (2.49). The effective masses of the upper valleys are not well established experimentally for $In_{0.7}Ga_{0.3}As$, so an effective mass of $0.22m_o$ was used, based on previously used values for GaAs that gave reasonable velocity-field characteristics. Additionally, the conduction band offsets of the upper valleys was taken as roughly one quarter of the central valley offsets. Admittedly, this is a rather dubious assumption made in order to obtain results for quantized states in the upper valleys. Typically, the upper valleys are treated as 3D. In fact, for most of the simulations conducted in this work, the $2\mathrm{D} \leftrightarrow 3\mathrm{D}$ transition threshold is considered to be the Γ valley to the L valley energy separation, so the effects of quantization in the upper valleys are not always a factor in the EMC model. In this case, conservation of energy requirements dictate that the energy separation of the valleys also be taken into consideration prior to a transition.

In Figure 2.5, plots of both surface roughness scattering and 2D alloy scattering are presented, per the treatment considered in sections 2.4.4 and 2.4.5. For the case of roughness scattering, only the "top" interface material barrier offset contributes to the average electric field in (2.55). Also, although it is difficult to see on the plot, the onset of scattering to the 4th subband occurs at approximately 0.35 eV. In this case the rms roughness length is 0.3 nm and the autocovariance length is 1.5 nm. With regard to the alloy scattering rate plotted per (2.56), the alloy perturbing potential is given as $\Delta V = 0.5\mathrm{V}$ and the lattice constant is taken as $5.8\overset{\circ}{\mathrm{A}}$

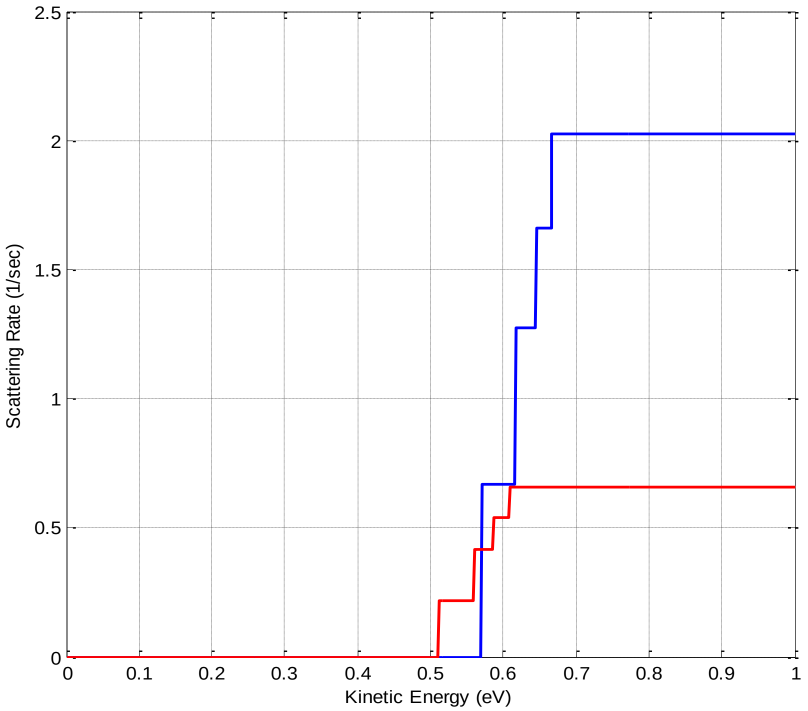

Figure 2.4 Intervalley non-polar optical phonon scattering rate for a 13nm $In_{0.7}Ga_{0.3}As$, as discussed in the text. Blue: emission rate; Red: absorption rate.

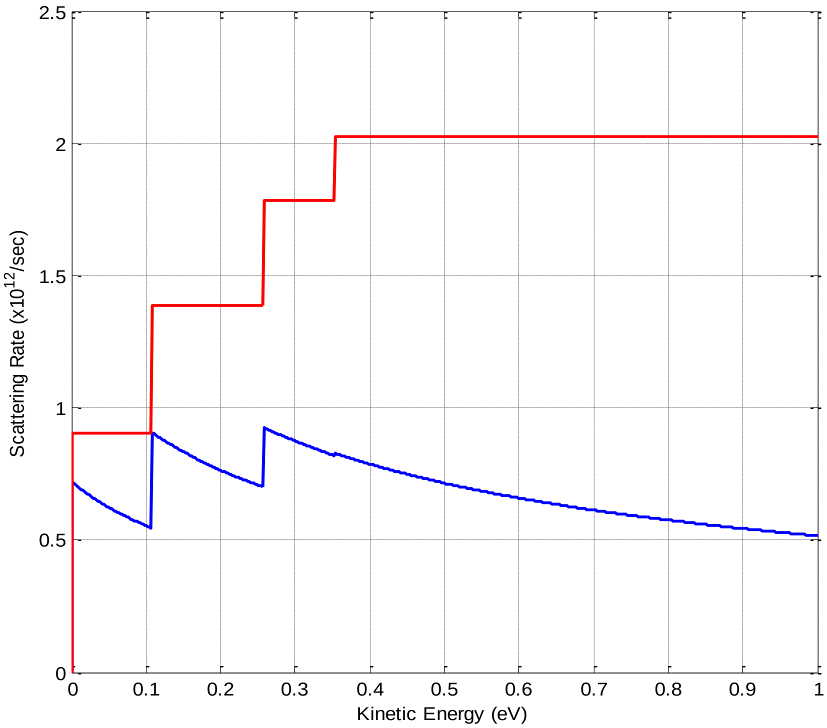

Figure 2.5 Roughness (blue, lower curve) and alloy scattering rates (red, upper curve) for the 13nm $In_{0.7}Ga_{0.3}As$ quantum well as discussed in the text.

Finally, the total scattering rate, taken as a sum of each rate plotted in Figures 2.2 -2.5, is given in Figure. 2.6.

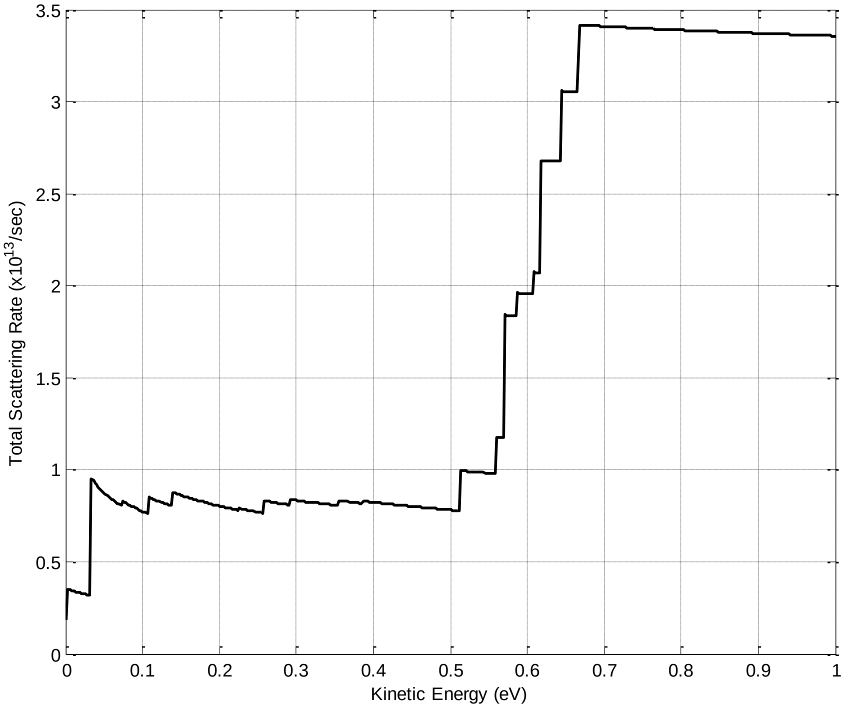

Figure 2.6. Total scattering rate from the 1st subband of the 13nm $In_{0.7}Ga_{0.3}As$ quantum well as discussed in the text. Each of the scattering rates plotted in Figures 2.2 - 2.5 are included.

3. Ensemble Monte Carlo Device Simulator

3.1 Overview

In this chapter, the details of the Ensemble Monte Carlo (EMC) algorithms utilized in this work are explained. The salient features of each algorithm are discussed in subsequent subsections of this chapter. First though, an overview of the entire process is presented as depicted in Figure 3.1. The resulting code is written in Fortran90, and output plots are generated using Matlab.

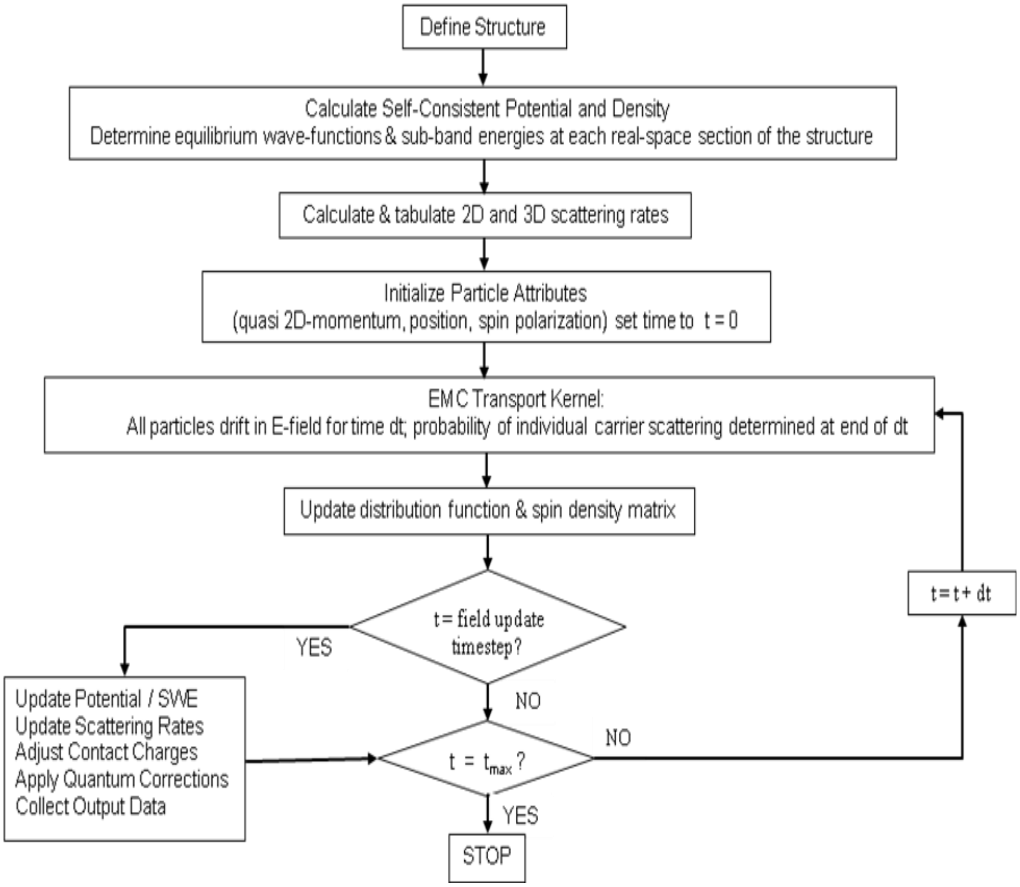
Define Structure
Calculate Self-Consistent Potential and Density
Determine equilibrium wave-functions & sub-band energies at each real-space section of the structure
Calculate & tabulate 2D and 3D scattering rates
Initialize Particle Attributes
(quasi 2D-momentum, position, spin polarization) set time to t = 0
EMC Transport Kernel:
All particles drift in E-field for time dt; probability of individual carrier scattering determined at end of dt
Update distribution function & spin density matrix
t = field update timestep?
YES
NO
t = t + dt
Update Potential / SWE
Update Scattering Rates
Adjust Contact Charges
Apply Quantum Corrections
Collect Output Data
t = t_max ?
NO
YES
STOP

Figure 3.1 Flowchart of the Ensemble Monte Carlo process.

First, the device structure is defined as a discrete set of mesh (grid) points. Accordingly, a particle-mesh scheme is created such that during the course of the simulation carrier attributes such as real-space position and momentum can acquire a continuous range of values, while the charge density is mapped to the discrete grid in order to calculate the electrostatic potential (and resulting electric field, which accelerates the carriers). In doing that mapping, a nearest grid-point scheme is employed, as opposed to a cloud-in-cell scheme, with only nominal differences observed in the results, since a "fine" mesh of 1nm or less is typically used.

After the structure is defined, a series of 1D Schrödinger Wave Equations (SWEs) coupled to a 3D Poisson Solver are solved self-consistently over the entire simulation domain in order to determine the initial potential (and resulting electric field), carrier density, subband energies, and wavefunctions for the 2D scattering rates. In doing this, a 1D SWE is solved along the direction of quantization (heterostructure growth direction) at each grid point, or "slice" of the device along the direction of transport. However, in doing this, the domain of the SWE solutions is not extended to certain regions of the device that are classified as only "3D", such as HEMT cap layers or HEMT entrenched gate regions. This was done for the numerical convenience of not possibly generating eigen-solutions spanning multiple quantum wells. Hence, in this work the initial carrier distribution in real-space is treated as 2D except within the cap layers and gate region of the III-V HEMT devices under consideration. Also, while the number of carriers per grid cell is based on the self-consistent density, the initial real-space positions within a grid cell are chosen at random. If desired, the initial spin distribution is also defined at this stage.

Then, after the initial real-space positions of the carriers are chosen, the carrier momentum and kinetic energy distribution is initialized according to either a Maxwell-Boltzmann or Fermi-Dirac Distribution. The 3D and initial 2D scattering rates are then calculated for each quantum state (i.e., every valley and subband) as a function of kinetic energy and tabulated as will be explained further in Section 3.2.

Next, during the EMC Kernel, carriers drift and scatter in the device under a fixed potential profile for a pre-determined number of free-flight time intervals (aka, "timesteps") until the charge distribution evolves so much that static electric field is considered to be "outdated". The time interval (and mesh size) between potential updates is chosen to satisfy the stability criteria associated with an electron plasma, as discussed in Section 3.4. Also, at each free-flight timestep of the EMC kernel, a check of the carrier energy, with respect to a pre-defined threshold, such the channel quantum well barrier height or Γ to L valley energy separation, is conducted to determine if a $\text{2D} \leftrightarrow \text{3D}$ transition is in order.

Once the simulation has been "frozen" momentarily in time in order to update the potential, the carrier positions are mapped to the discrete grid to obtain the density needed in solving the Poisson equation. Prior to updating the potential however, the charge distribution in the contact regions is adjusted to maintain the distribution that existed in the contact regions at equilibrium. (The net change in the charge at the contacts between potential updates serves as one measure of the carrier current). Additionally, throughout the simulation domain, the distribution of charge in the direction of quantization (i.e., the heterostructure growth direction) associated with 2D carriers is mapped to the grid in order to conform to the spatial distribution of the squared envelope functions. In doing this, the contributions from carriers in each 2D subband contribute to the charge density.

Then, just after the potential is updated and prior to resuming the dynamical simulation, or at some pre-defined number of "SWE timesteps" later, the 1D SWE equations are re-solved and the 2D scattering rates updated. Also, prior to resuming the dynamical simulation after updating the potential, output quantities as a function of time are stored. Amongst these are the carrier density, average velocity, average carrier energy, spin polarization (if applicable), and certain diagnostic quantities such as 2D subband occupancy as a function of time and position.

In the subsequent subsections, the EMC kernel will be presented first, since understanding it is critical to appreciating the structure of the other routines.

3.2 Monte Carlo Transport Kernel

In Ensemble Monte Carlo (EMC) simulation, the random motion of charge carriers in the semiconductor device is simulated as free flights subjected to forces that accelerate the carriers during free flight and instantaneous scattering events that randomize the velocity. The choice of a particular scattering mechanism is a stochastic process whereby a random number with uniform probability distribution between 0 and 1 is first selected. The value of this number, relative to its position in a normalized table of the comparative scattering rates, then determines the particular scattering mechanism to be chosen. The quantitative details of this process will now be discussed (In this chapter the notation of Tomizawa [63] is frequently employed).

The probability per unit time that a carrier will travel for a free flight of duration τ and then scatter at the end of this time is given as

$$P(\tau) = W_T(E_k)\exp\left(-\int_0^{\tau} W_T(E_k)dt\right) \quad , \tag{3.1}$$

where $W_T(E_k)$ refers to an algebraic summation of all the scattering mechanisms as a function of kinetic energy that will be included in the model. Since $W_T(E_k)$ is, of course, not constant as a function of energy, an analytical evaluation of (3.1) is not possible. However, a clever solution to the problem is to introduce the concept of self-scattering [37] in which a self-scattering rate $W_S(E_k)$ is defined at descritized intervals of kinetic energy, in order to yield a total scattering rate, Γ, that is a constant over the entire energy range. This virtual scattering mechanism causes no actual change to carrier dynamics. Thus, (3.1) can be re-written as,

$$P(\tau) = \Gamma e^{-\Gamma\tau} \quad . \tag{3.2}$$

In consideration of (3.2), the MC algorithm can now proceed in two different ways, both of which yield statistically equivalent results. In the first approach, a random number can be chosen that is distributed uniformly between 0 and 1. This number is then said to be equal to $P(\tau)$, and (3.2) is then solved for the resultant free flight time τ. Alternatively, as is done in this work, a random-number rejection technique can also be employed. In that case, the free flight time

τ can be defined *a priori* and (3.2) is then solved for $P(\tau)$. A random number is then chosen, distributed uniformly between 0 and 1. If this number is less than $P(\tau)$ a scattering event will occur. Otherwise, a new free flight will simply take place. This latter method was chosen so as to utilize certain code segments developed by this author for other work, but otherwise arbitrarily.

Next, if it has been decided that a scattering event should occur, the particular mechanism is determined by choosing another random number that also has a uniform probability distribution between 0 and 1. The value of this number, with respect to its position in a normalized table of comparative scattering rates, determines the particular scattering mechanism chosen. This table is computed prior to running the dynamical portion of the EMC.

Depicted in Figure 3.2 is a section of this table for some carrier with kinetic energy $E_k \pm dE_k/2$. For n scattering mechanisms considered, numerically labeled 1 through n, a particular mechanism is chosen such that $P_n \le r \le P_{n-1}$ where P_n is the probability of choosing the nth mechanism , and r is the value of the random number. If these criteria cannot be satisfied, the event is treated as self-scattering, and no change occurs to the carrier's wavevector.

In the EMC model developed in this work, a normalized scattering table as a function of kinetic energy is created for every quantum mechanical state. For 3D carriers, this implies that separate tables are needed for each valley. For 2D carriers, a separate table is created for each subband within each valley. However, the carriers in the upper valleys are typically treated as 3D as they are high in energy relative to the central valley. The choice of 2D or 3D carrier motion in the upper valleys is user-defined in the parameter input files.

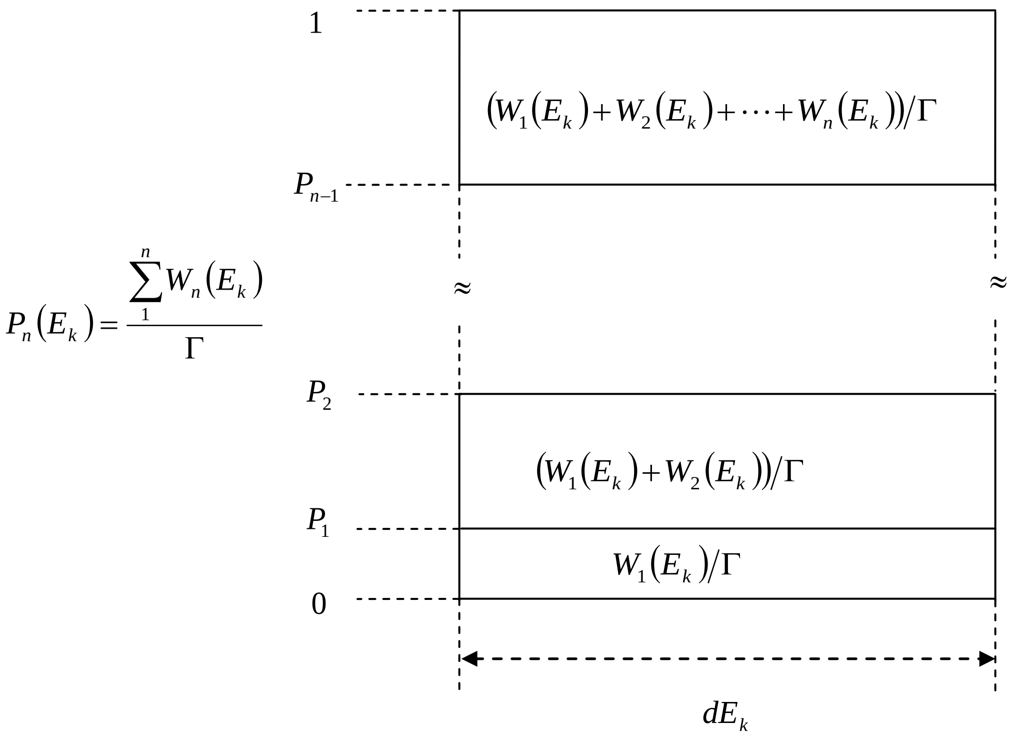
1
$(W_1(E_k)+W_2(E_k)+\cdots+W_n(E_k))/\Gamma$
P_{n-1}
$P_n(E_k)=\frac{\sum_1^n W_n(E_k)}{\Gamma}$
≈
≈
P_2
$(W_1(E_k)+W_2(E_k))/\Gamma$
P_1
$W_1(E_k)/\Gamma$
0
dE_k

Figure 3.2 Depiction of the scattering table at a particular value of kinetic energy in the range $E_k \pm dE_k/2$.

3.3 Structural Definitions and Nomenclature

For the particle-mesh scheme used in this work, a non-uniform, center-point finite difference scheme defines the discrete mesh (grid) for all three spatial dimensions for any rectilinear structure considered. Such a non-uniform grid is crucial in solving the SWE and Poisson equations, if large variations in the potential occur over small spatial lengths. A one-dimensional depiction of the grid is given in Figure 3.3.

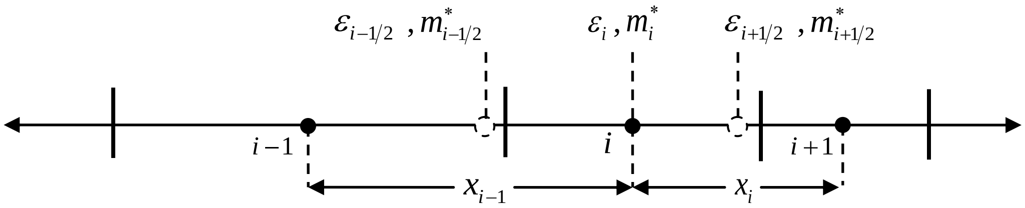

$\varepsilon_{i-1/2}$, $m^*_{i-1/2}$
ε_i , m^*_i
$\varepsilon_{i+1/2}$, $m^*_{i+1/2}$
$i-1$
i
$i+1$
x_{i-1}
x_i

Figure 3.3 One-dimensional depiction of the non-uniform center-point difference grid, showing the variation of effective mass and permittivity parameters. The notation is adapted from [25].

Note that in Figure 3.3 the effective mass and permittivity parameters are defined for each ith grid point, and also at half the distance to adjacent grid points, which are not necessarily spaced apart from one another uniformly. Also, the notation of defining the distance between the ith grid point and the adjacent grid points as x_{i-1} and x_i will be retained in subsequent sections of this chapter, notably in sections 3.6 and 3.7 in which the descritization of the SWE and Poisson equations is explained.

Of course, a two-dimensional extension of the mesh scheme depicted in Figure 3.3 is actually employed for the HEMT simulation in this work in order to define the heterostructure growth and transport directions that correspond to the device depth and length, respectively. For the HEMT modeling in this work, however, the width dimension is not needed in solving the Poisson equation. This is because the width of the HEMT is assumed to be sufficiently large such that a constant potential can be assumed in that direction, for each particular mesh point of the residual two dimensional plane that is defined by the growth and transport directions. The width dimension is needed though in modeling some spintronics devices where confinement potentials in the transverse direction are considered.

The index naming scheme used throughout this work is as follows: The "i" index corresponds to the heterostructure growth direction, increasing in value from the top surface of the device to the substrate. The direction of transport in the devices is defined by the "j" index, which increases from the "source" to "drain" side of the device. The "k" index refers to the mesh along the device width in the 3D version of the code.

3.4 Time Step and Mesh Size Criteria

As mentioned in the Introduction, carrier transport in a semiconductor device can be described essentially as that of a plasma. A well known result of basic plasma physics for non-degenerate systems is that the spatial variation of charge density results in a variation of the potential that can only be resolved within a minimal spatial distance known as the Debye length. The Debye length is expressed as

$$L_D = \sqrt{\frac{\varepsilon k_B T}{q^2 N_s}} \quad , \tag{3.3}$$

where ε is the material permittivity and N_s is the doping concentration. Consequently, it is imperative that the grid spacing never exceed this length. Otherwise, non-physical plasma oscillations will result from a grid which is too course.

Likewise, due to the Coulombic forces amongst the constituent charge carriers of the plasma, the charge distribution will oscillate at the plasma frequency expressed as

$$\omega_p = \sqrt{\frac{nq^2}{\varepsilon m^*}} \quad , \tag{3.4}$$

where ε is the material permittivity and n is the charge density. Therefore, the time interval between successive updates of the potential (aka, the timestep) should not exceed that of the plasma period, which is the inverse of (3.4), given as,

$$T_p = \frac{2\pi}{\omega_p} \quad . \tag{3.5}$$

In practice, choosing the timestep and grid spacing is by trial-and-error, within these guidelines. A good rule of thumb is that the ratios of timestep and grid spacing, to the plasma period and Debye length, respectively, should be on the order of unity. A comprehensive discussion of the aforementioned stability criteria issues is given in [65].

3.5 Initialization of Carrier Distribution

In principle, the initial energy, momentum, and spatial distribution of carriers does not matter, if one is only interested in studying steady state phenomena, and computational efficiency is not of consequence. In those cases, it is sometimes convenient, from a coding perspective, to simply assign the initial position of the carriers about the dopant sites, and to assign the carriers an initial momentum and energy based upon the proper thermodynamic statistical distribution (e.g. Fermi-Dirac).

However, in this work, all carrier attributes are initialized to the condition of thermodynamic equilibrium via a self consistent solution of the SWE and

Poisson equations. The initial motion is thus treated as 2D, except within the cap layers of the Intel HEMT structure under consideration, in which case the carriers are always assumed to be 3D. This initialization scheme is deemed to be the "most realistic" physical scenario prior to running the dynamical EMC part of the simulation. Based on prior experience, initializing the distribution to the dopant sites results in much longer transient times prior to reaching steady state, and can possibly yield drastic, unphysical "swings" in the electrostatic potential prior to convergence to such an extent that carriers become "trapped" in momentum space, in upper valleys, while traveling (in real space) from the dopant sites to the channel.

Due to their complexity, the details for solving either the Poisson or SWE equations are reserved for subsections 3.6 and 3.7 of this chapter, respectively. However, the general scheme of the SWE-Poisson calculation is as follows: First, an initial guess is first made of the 3D electrostatic potential ϕ by solving the 3D Poisson equation,

$$\nabla \cdot \varepsilon \cdot \left(-\nabla \cdot \phi\right) = \rho \quad , \tag{3.6}$$

using the initial assumption that the carrier density, ρ, is equal to the doping density. Then, for each region of quantization in the device (i.e., each mesh "slice" of the 2D plane defined by the growth and transport directions, or in the case of 3D devices, each "column" of grid points, defined at every in-plane mesh point), the resulting electrostatic potential is then added to the material band offset potentials, in order to determine the potential energy contribution to the Hamiltonian of the one-dimensional effective mass equation for that region. A quantum mechanical approximation determination of the 3D carrier density can then be extracted for that region as

$$n_{3D}(i, j, k) = \sum_{n=1}^{nsub} (n_{2D})_n \, \varphi_n^*(i)\varphi_n(i)\Big|_{j,k} \quad , \tag{3.7}$$

where n_{2D} is the 2D sheet density and $\varphi_n(i)$ is the envelope function for the nth subband, which must be normalized so that its units are $1/\sqrt{meters}$. The newly determined 3D density is then fed back into the 3D Poisson equation, the electrostatic potential is re-calculated, and the process is iterated until convergence is reached, i.e., the difference in the potential, as computed from successive iterations of the Poisson equation, is lower than some pre-defined tolerance.

In (3.7), the determination of the sheet density n_{2D} is based on the well known expression

$$n_{2D} = \int_0^\infty D_{2D}(E)\, f_{FD}(E, E_f, T)\, dE \quad , \tag{3.8}$$

where, in this case the 2D density of states $D_{2D}(E)$ is a constant given by $m^*/(\pi\hbar^2)$ and f_{FD} is the Fermi-Dirac function. Thus,

$$\begin{aligned} n_{2D} &= \int_0^\infty \frac{m^*}{\pi\hbar^2}\left[\exp\left(\frac{E-E_F}{k_B T}\right)+1\right]^{-1} dE \\ &= \sum_1^{n\max} \frac{m^* k_B T}{\pi\hbar^2} \ln\left(1+\exp\left(\frac{E_n - E_F}{k_B T}\right)\right) \quad . \end{aligned} \tag{3.9}$$

where E_n is the subband minimum for the nth subband, $n\max$ is a pre-defined maximum number of allowed subbands.

Numerically, the choice of $n\max$ must be such that all occupied subbands in the quantum well are included. Also, for computational convenience the Fermi level, E_f, is set to mathematical zero. Furthermore, in this work, the maximum error allowed in the converged solution is typically less than 10^{-5} V, based on a tradeoff between accuracy and convergence times.

3.6 Descritization of Poisson's Equation

From Maxwell's equations,

$$\nabla \cdot \mathbf{D} = \rho \quad , \tag{3.10}$$

where $\mathbf{D}$ is the electric displacement vector and ρ is the free charge density. The displacement vector in turn is given by the constitutive equation,

$$\mathbf{D} = \varepsilon \cdot \mathbf{E} \quad , \tag{3.11}$$

where ε is the dielectric permittivity and $\mathbf{E}$ is the electric field. In turn, the electric field is defined in terms of the gradient of the electrostatic potential as

$$\mathbf{E} = -\nabla\phi \quad . \tag{3.12}$$

Substituting (3.11) into (3.10), using (3.12), yields (3.6), repeated for convenience:

$$\nabla \cdot \varepsilon \cdot \left(-\nabla\phi\right) = \rho \quad . \tag{3.13}$$

The descritization of (3.13) is done using a center-point finite difference scheme as depicted in Figure 3.3. (In the following argument, only one dimension is depicted for clarity, since the presence of the dot product implies that the multi-dimensional derivation is straightforward extension of the one-dimensional argument). Starting with the differentiation of (3.10),

$$\nabla \cdot \mathbf{D}\Big|_{x_i} = \frac{\mathbf{D}_{i+1/2} - \mathbf{D}_{i-1/2}}{0.5\left(x_i + x_{i-1}\right)} = \rho\left(x_i\right) \quad , \tag{3.14}$$

inserting (3.11) to into (3.14) yields,

$$\nabla \cdot \mathbf{D}\Big|_{x_i} = \frac{\varepsilon_{i+1/2}\mathbf{E}_{i+1/2} - \varepsilon_{i-1/2}\mathbf{E}_{i-1/2}}{0.5\left(x_i + x_{i-1}\right)} = \rho\left(x_i\right) \quad . \tag{3.15}$$

Thus, (3.15) can be re-written, making use of (3.12), as,

$$\begin{aligned} \nabla \cdot \mathbf{D}\Big|_{x_i} &= \frac{-\left(\varepsilon_{i+1/2}\nabla\phi_{i+1/2} - \varepsilon_{i-1/2}\nabla\phi_{i-1/2}\right)}{0.5\left(x_i + x_{i-1}\right)} \\ &= \frac{-\left(\varepsilon_{i+1/2}\dfrac{\phi_{i+1} - \phi_i}{x_i} - \varepsilon_{i-1/2}\dfrac{\phi_i - \phi_{i-1}}{x_{i-1}}\right)}{0.5\left(x_i + x_{i-1}\right)} \\ &= \rho\left(x_i\right) \quad . \end{aligned} \tag{3.16}$$

Finally, re-arranging (3.16) gives

$$ncoef\ \left(\phi_{i-1}\right) + ccoef\ \left(\phi_i\right) + scoef\ \left(\phi_{i+1}\right) = ff\ \left(x_i\right) \quad , \tag{3.17}$$

where the "north", "south", and "center " coefficients and the "ff" (forcing function) in (3.17) are given as,

$$ncoef = \varepsilon_{i-1/2} \frac{1}{0.5x_{i-1}\left(x_i + x_{i-1}\right)} \quad , \tag{3.18}$$

$$scoef = \varepsilon_{i+1/2} \frac{1}{0.5x_{i}\left(x_i + x_{i-1}\right)} \quad , \tag{3.19}$$

$$ccoef = -\left(\frac{\varepsilon_{i+1/2}}{x_i} + \frac{\varepsilon_{i-1/2}}{x_{i-1}}\right)\frac{1}{0.5\left(x_i + x_{i-1}\right)} \quad , \tag{3.20}$$

$$ff = -\rho\left(x_i\right) \quad . \tag{3.21}$$

Thus, given a charge density $\rho\left(x_i\right)$, the electrostatic potential ϕ_i can be solved by iteratively operating on (3.17), after a first guess of each ϕ_i is made. Neumann boundary conditions are imposed on the solution when the electric field is assumed to be zero at a boundary, and Dirichlet conditions imposed for points of constant potential in the simulation domain.

In this work, the well known Gauss-Siedel iterative scheme was used to solve the three-dimensional extension of (3.17). While this scheme has been found adequate in the present work, future device structures with highly non-uniform meshes will likely require the utilization of a multigrid technique [33].

3.7 Descritization of SWE

When computer memory is not an issue, a uniform mesh may be sufficient to descritize the SWE. Usage of a uniform mesh preserves the symmetry of the matrix of the eigen-operator, making the eigenvalue problem easier to solve. In order to account for a non-uniform grid though, as is often necessary for HEMT structures, the method, due to Tan, et al. [64], is utilized as discussed below.

Assuming a position-dependent effective mass, the 1D SWE is,

$$-\frac{\hbar^2}{2}\nabla\left(\frac{1}{m^*(x)}\nabla\right)\psi(x)+V(x)\psi(x)=E\,\psi(x) \quad . \tag{3.22}$$

Since the first term on the left-hand side of (3.22) is of the same form as the left hand side of (3.6) the center-point finite difference descritization scheme is exactly analogous to that of the Poisson equation. Accordingly, (3.22) can be expressed as (using matrix notation):

$$\mathbf{A}\psi = \lambda\psi \quad , \tag{3.23}$$

where the matrix elements of $\mathbf{A}$ are given as,

$$A_{ij} = -\frac{\hbar^2}{2}\left(\frac{1}{m^*_{i-1/2}}\frac{1}{x_{i-1}}\frac{1}{L_i^2}\right) \text{ for } \; j = i+1 \quad , \tag{3.24}$$

$$A_{ij} = -\frac{\hbar^2}{2}\left(\frac{1}{m^*_{i+1/2}}\frac{1}{x_i}\frac{1}{L_i^2}\right) \text{ for } \; j = i-1 \quad , \tag{3.25}$$

$$A_{ij} = -A_{i,i+1} - A_{i,i-1} + V \text{ for } \; j = i \quad , \tag{3.26}$$

and otherwise

$$A_{ij} = 0 \text{ for } \; j = i \quad . \tag{3.27}$$

Note that a matrix $\mathbf{L}$ has now been defined so that the square of each element L_i can be written as $L_i^2 = 0.5x_i(x_i + x_{i-1})$. This allows one to define a new matrix $\mathbf{B}$ such that $\mathbf{B} = \mathbf{LLA}$, where $B_{ij} = L_i^2 A_{ij}$. Now, making the substitution $\mathbf{M} = \mathbf{LL}$, (3.23) is recast as,

$$\mathbf{B}\psi = \mathbf{MA}\psi \quad . \tag{3.28}$$

Operating on both sides of (3.28) with the inverse of matrix $\mathbf{L}$ as

$$\mathbf{L}^{-1}\mathbf{B}\psi = \mathbf{L}^{-1}\mathbf{L}\mathbf{L}\mathbf{A}\,\psi \quad , \tag{3.29}$$

one observes that

$$\mathbf{L}^{-1}\mathbf{B}\psi = \mathbf{L}^{-1}\mathbf{B}\mathbf{L}^{-1}\mathbf{L}\psi \quad . \tag{3.30}$$

Finally, setting, $\mathbf{H} = \mathbf{L}^{-1}\mathbf{B}\mathbf{L}^{-1}$ and $\Phi = \mathbf{L}\psi$, one obtains

$$\mathbf{H}\Phi = \lambda\Phi \quad . \tag{3.31}$$

which implies that $\mathbf{H}$ is symmetric since $\mathbf{L}^{-1}$ is diagonal and $\mathbf{B}$ is symmetric. Thus, solving the eigenvalue problem given by (3.31) immediately yields the correct eigen-energies, λ. The original wavefunction ψ is then found by simply operating on (3.31) with the inverse of matrix operator $\mathbf{L}$.

In this work, the solution of (3.31) was performed using the well known Fortran LAPACK routine DSTEVX.

3.8 Carrier Motion

By the Bloch acceleration theorem, the force acting on a carrier is given as

$$\mathbf{F} = \hbar\frac{d\mathbf{k}}{dt} \quad , \tag{3.32}$$

where $\mathbf{k}$ denotes the particle wavevector. In the EMC, the force is the electrostatic force, $\mathbf{F} = -q\mathbf{E}$, whereby the carriers have charge magnitude q and are subjected to an electric field given as $\mathbf{E} = -\nabla\varphi$, where the electrostatic potential given as φ. Use of (3.32) thus implies that the change of the particle's wavevector due to acceleration in the electric field is

$$d\mathbf{k} = \frac{q\mathbf{E}dt}{\hbar} \quad . \tag{3.33}$$

Thus, after carrier drift the wavevector is updated as

$$\mathbf{k}' = \mathbf{k} + d\mathbf{k} \quad . \tag{3.34}$$

The real-space position of the particle is then updated by making use of the following definition of velocity:

$$\mathbf{v} = \frac{1}{\hbar}\nabla_k E_k \quad , \tag{3.35}$$

and utilizing the Kane relation for non-parabolic dispersion

$$E_k = \frac{\sqrt{1+4\alpha\gamma(k)}-1}{2\alpha} \quad . \tag{3.36}$$

Inserting (3.36) into (3.35) yields,

$$\mathbf{v} = \frac{\hbar\mathbf{k}}{m^*\sqrt{1+4\alpha\gamma(k)}} \quad . \tag{3.37}$$

Taking the average over all particles in the ensemble, the average instantaneous velocity is given as

$$\langle\mathbf{v}\rangle = \frac{\hbar\langle\mathbf{k}\rangle}{m^*\sqrt{1+4\alpha\gamma(\langle k\rangle)}} \quad . \tag{3.38}$$

Note that

$$\langle\mathbf{k}\rangle = \frac{\mathbf{k}_f + \mathbf{k}_i}{2} \quad , \tag{3.39}$$

denotes the average of the initial and final wavevectors. (3.39) and (3.37) can be then be combined. This implies that

$$\langle \mathbf{k} \rangle = \mathbf{k}_i + \frac{d\mathbf{k}}{2} \quad . \tag{3.40}$$

Therefore, since $\langle d\mathbf{r} \rangle = \langle \mathbf{v} \rangle dt$ and $\mathbf{r}' = \mathbf{r} + \langle d\mathbf{r} \rangle$, substituting (3.40) into (3.38) results in the carrier position after drift being expressed as

$$\mathbf{r}' = \mathbf{r} + \frac{\hbar \langle \mathbf{k} \rangle}{m^* \sqrt{1 + 4\alpha\gamma(\langle k \rangle)}} dt \quad . \tag{3.41}$$

For the case of parabolic bands $(\alpha = 0)$ (3.40) reduces to

$$\mathbf{r}' = \mathbf{r} + \frac{\hbar}{m^*} dt \left(\mathbf{k} + \frac{d\mathbf{k}}{2} \right) \quad . \tag{3.42}$$

3.8.1 Specular Reflection

After a carrier drift, the position of the carrier may exceed the specified dimensions of the device. If the grid cell prior to the drift was defined by a Dirichlet condition (i.e., the potential is fixed to some value) corresponding to an ohmic contact, the particle is absorbed and removed from the simulation. However, if a Neumann boundary condition exists on the charge density then a specular reflection occurs. A reflection about the "top" or "bottom" surface of a rectilinear device is depicted in Figure 3.4 (the argument for a reflection at a "left" or "right" boundary is directly analogous).

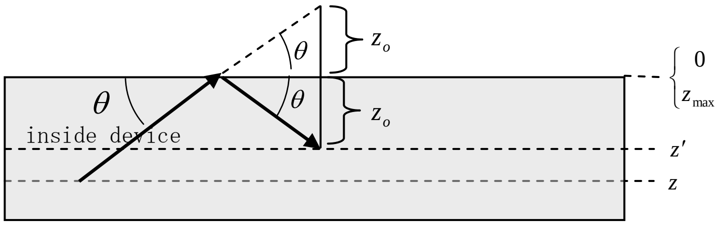

$$z' = -z_o \qquad \text{("top" surface)}$$

$$z' = z_{\max} - \left(z_o - z_{\max}\right) \qquad \text{("bottom" surface)}$$

Figure 3.4 Depiction of specular reflection at a Neumann boundary. In this case, specular reflection at the top surface is depicted.

In Figure 3.4, the carrier has "overshot" the top surface boundary by a distance z_o. The new particle positions after such a reflection are indicated in the equations of Figure 3.4. In this case, the new "x" position has been already determined by via carrier drift in the electric field and is not affected by the boundary encounter. A specular reflection may also occur at a heterostructure interface, as will be described in section 3.8.2.

3.8.2 Barrier Encounters for 3D Carriers

After a 3D carrier completes a drift in a given timestep, it must be determined if a potential barrier was encountered due to a band offset between different materials. This is done by utilizing a carrier attribute called "material type" in which the old and new material types are compared after the drift. Then, the kinetic energy of the carrier is compared to the barrier potential energy. If the kinetic energy is less than the barrier height, a specular reflection occurs, exactly as described in section 3.8.1. If the kinetic energy is greater than the barrier, transmission will occur, provided that a final state exists in momentum space for which the in-plane momentum (perpendicular to the barrier) can be conserved.

Otherwise, a specular reflection occurs. Again, specular reflection occurs exactly as described in section 3.8.1.

Therefore, in the event a carrier has been made a candidate for transmission (final state selection has yet to be considered), the kinetic energy will be transformed as $E_k \to E_k - \Delta E_B$ where ΔE_B is the barrier offset, defined as the difference between the "new" and "old" material offsets. Conserving in-plane momentum requires that $\mathbf{k}'_{//} = \mathbf{k}_{//}$. This, in turn, requires that the squared value of the new wavevector perpendicular to the interface be given as,

$$k_z'^2 = \frac{2m'^*}{\hbar^2}\left(E_k - \Delta E_B\right)\left[1 + \alpha\left(E_k - \Delta E_B\right)\right] - k_{//}^2 \quad . \tag{3.43}$$

Of course, $k_z'^2$ must be greater than zero. If this condition is met, transmission occurs. Otherwise, no condition exists to conserve in-plane momentum and specular reflection occurs.

Although the preceding argument was made for barrier encounters perpendicular to the transport direction, the EMC developed in this work allows also for 3D barrier encounters parallel to the direction of transport. These may exist, for example, due to entrenched gates or insulating layers.

3.9 2D→3D Transitions

When the total energy of a 2D carrier (kinetic plus sub-band energy relative to the potential minimum in the local region of quantization) exceeds some pre-defined threshold, i.e., $E_k^{2D} + E_{sub} > E_t$, the carrier is considered then to behave as a 3D carrier and be subjected thereafter to 3D scattering mechanisms.

In that case, the 2D subband energy is transformed into an additive component to the kinetic energy.

Conserving in-plane momentum requires that $\mathbf{k}'_{//} = \mathbf{k}_{//}$. Also, the real space position is unaltered during the transition. Therefore, the energy-momentum relationship of the transition is written as

$$\frac{\hbar^2}{2m^*}\left(k_{//}^{2} + k_z'^{2}\right) = \left(E_k^{2D} + E_{sub}\right)\left[1 + \alpha\left(E_k^{2D} + E_{sub}\right)\right] \quad . \tag{3.44}$$

Re-arranging and solving for k_z' yields,

$$\left|k_z'\right| = \sqrt{\frac{2m'^*}{\hbar^2}\left(E_k^{2D} + E_{sub}\right)\left[1 + \alpha\left(E_k^{2D} + E_{sub}\right)\right] - k_{//}^{2}} \quad . \tag{3.45}$$

Before determining $\left|k_z'\right|$ however by this expression, a check of the sign of the argument in (3.45) is performed. A negative value indicates that a condition does not exist to preserve in-plane momentum and thus a 2D→3D transition will not occur. If a transition is allowed to occur, the direction of k_z', either positive of negative, is chosen at random, with both values considered to be equally probable.

3.10 3D→2D Transitions

For a 3D carrier, when the condition exists such that $E_k^{3D} < E_t$, a 3D→2D transition may occur. Conservation of energy and in-plane momentum then requires that $E_k^{3D} \rightarrow E_k^{2D} + E_{sub}$. Therefore, the new subband energy associated with the 2D carrier must be such that $E_{sub} = E_k^{3D} - E_k^{2D}$. However, choosing the subband energy in this manner is inconsistent with the fact that the subband energy levels in the quantum well comprising the transport channel have already been pre-determined by the most recent local solution of the periodically updated SWE.

The approximation is thus made that the new 2D carrier will occupy the nth subband such that $E_n \le E_{sub} \le E_{n+1}$. In the event that E_{sub} is less than the ground state subband energy, it is assumed that $n=1$.

Strictly speaking, energy conservation is, of course, violated in this model. Also, it must be noted that an inconsistency exists in determining the carrier energies between the 2D$\rightarrow$3D and 3D$\rightarrow$2D cases. This is because a parabolic dispersion exists in the 2D case, but not in the 3D case. Correcting this problem by using non-parabolic 2D scattering rates will be the subject of future work.

Finally, it must be noted that a more accurate model of 2D$\leftrightarrow$3D transitions has been considered by others [66] in which transition rates are treated as scattering events between 2D and 3D eigenstates. The form of the resulting transition rates then resembles the form of the scattering rates used in this work.

3.11 Scattering Final State Selection

3.11.1 Isotropic Scattering

For the scattering mechanisms described in Chapter 2 that were classified as "isotropic", the magnitude of the final wavevector is still determined by energy conservation requirements. However, as shown in Figure 3.5, all angles of the solid angle $\boldsymbol{\beta}$ between the initial and final wavevectors are equally probable.

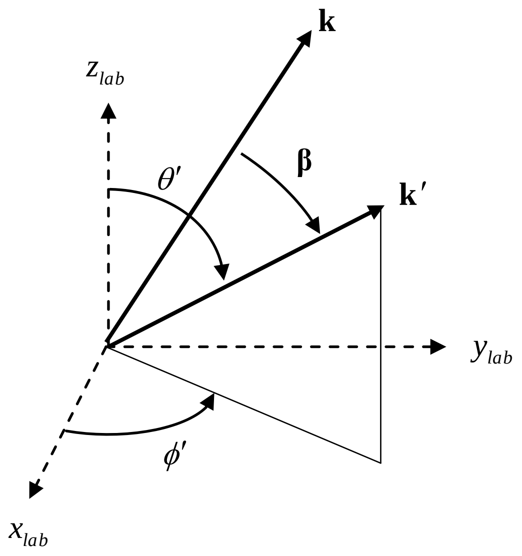

Figure 3.5 Scattering angles in the isotropic scattering process.

Thus, for the spherical coordinates employed in this model, the final polar and azimuthal angles, with respect to the axis of the "laboratory system" can be determined from two random numbers, r_1 and r_2 , both distributed uniformly between 0 and 1, i.e.,

$$\phi' = 2\pi r_1 \quad , \tag{3.46}$$

$$\cos\,\theta' = 1 - 2r_2 \quad . \tag{3.47}$$

The components of the new wavevector are then given as,

$$k'_x = k' \sin\theta' \cos\,\phi' \quad , \tag{3.48}$$

$$k'_y = k' \sin\theta' \sin\phi' \quad , \tag{3.49}$$

$$k'_z = k' \cos\,\theta' \quad . \tag{3.50}$$

For the case of 2D isotropic scattering in spherical bands, the formalism is analogous; one simply sets $\theta' = 90^\circ$.

3.11.2 Anisotropic Scattering

Due to the angular symmetry of the problem in this case, any value for the angle ϕ' is still equally probable, as was the case for isotropic scattering. However the polar component of $\boldsymbol{\beta}$ in Figure 3.5 now has an angular dependence in which small angle scattering is favored. Therefore, the components of $\mathbf{k}'$ need to be defined in terms of β .

Determining the components of $\mathbf{k}'$ is most easily accomplished by utilizing a rotated coordinate system as depicted in Figure 3.6. In the rotated coordinate system, the initial wavevector $\mathbf{k}$ is aligned with the z-axis of the rotated system by rotating the original coordinate system (laboratory system) about the y-axis of the laboratory system by an angle α_x . Then, another rotation is performed about the z-axis of the laboratory system by an angle α_z.

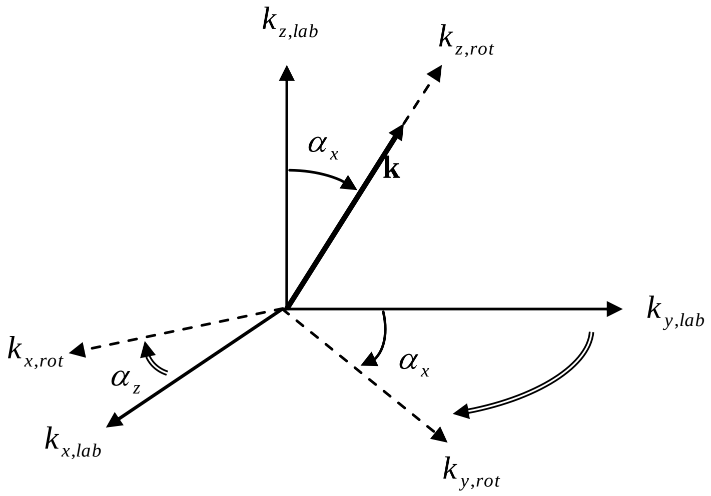

Figure 3.6 Rotated coordinate system used to determine anisotropic scattering angle.

The final wavevector within the rotated coordinate system is then given as,

$$\mathbf{k}'_{rot} = \mathbf{U_{rot}} \mathbf{k}'_{lab} \quad . \tag{3.51}$$

Using basic linear algebra, the rotation matrix $\mathbf{U_{rot}}$ can be decomposed into the matrix product of the α_x and α_z rotation matrices as

$$\mathbf{U_{rot}} = \mathbf{U}_{\alpha_x} \mathbf{U}_{\alpha_z} \quad . \tag{3.52}$$

In turn, (3.52) can be decomposed as,

$$\mathbf{U}_{\alpha_x} = \begin{pmatrix} 1 & 0 & 0 \\ 0 & \cos\alpha_x & -\sin\alpha_x \\ 0 & \sin\alpha_x & \cos\alpha_x \end{pmatrix} \quad , \tag{3.53}$$

$$\mathbf{U}_{\alpha_z} = \begin{pmatrix} \cos\alpha_z & -\sin\alpha_z & 0 \\ \sin\alpha_z & \cos\alpha_z & 0 \\ 0 & 0 & 1 \end{pmatrix} \quad . \tag{3.54}$$

In the rotated coordinate system, $\boldsymbol{\beta}$ can then be decomposed into its polar and azimuthal components, θ' and ϕ', respectively, as depicted in Figure (3.7):

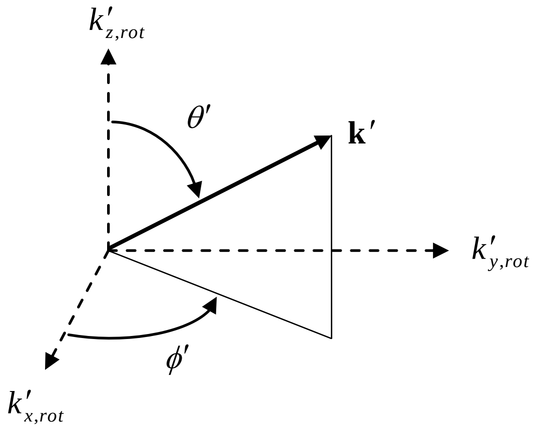

Figure 3.7 Rotated Coordinate system for anisotropic scattering.

Since $\mathbf{k}'_{rot} = \mathbf{U_{rot}}\mathbf{k}'_{lab}$, it follows that

$$\mathbf{k}'_{lab} = \mathbf{U}^{-1}_{\mathbf{rot}}\mathbf{k}'_{rot} \quad . \tag{3.55}$$

Note that $\mathbf{U}^{-1}_{\mathbf{rot}}$ can be found by taking the inverse of (3.52) such that

$$\mathbf{U}^{-1}_{\mathbf{rot}} = \begin{pmatrix} \cos\alpha_z & \cos\alpha_x \sin\alpha_z & \sin\alpha_x \sin\alpha_z \\ -\sin\alpha_z & \cos\alpha_x \cos\alpha_z & \sin\alpha_x \cos\alpha_z \\ 0 & -\sin\alpha_x & \cos\alpha_x \end{pmatrix} \quad . \tag{3.56}$$

Then, inserting (3.56) and (3.51) into (3.55) yields

$$\begin{matrix} k'_x \\ k'_y \\ k'_z \end{matrix} = \begin{pmatrix} \cos\alpha_z & \cos\alpha_x \sin\alpha_z & \sin\alpha_x \sin\alpha_z \\ -\sin\alpha_z & \cos\alpha_x \cos\alpha_z & \sin\alpha_x \cos\alpha_z \\ 0 & -\sin\alpha_x & \cos\alpha_x \end{pmatrix} \begin{pmatrix} k'\sin\theta'\cos\phi' \\ k'\sin\theta'\sin\phi' \\ k'\cos\theta' \end{pmatrix} \quad . \tag{3.57}$$

Finally, inspection of Figure 3.6 reveals that the trigonometric matrix elements of (3.57) are given as,

$$\cos\,\alpha_x = \frac{k_z}{k} \ , \tag{3.58}$$

$$\cos\,\alpha_z = \frac{k_y}{\sqrt{k_x^2 + k_y^2}} \ , \tag{3.59}$$

$$\sin\alpha_x = \frac{\sqrt{k_x^2 + k_y^2}}{k} \ , \tag{3.60}$$

$$\sin\alpha_z = \frac{k_x}{\sqrt{k_x^2 + k_y^2}} \ , \tag{3.61}$$

The treatment of 2D anisotropic scattering is analogous. Setting $\alpha_x = 90^\circ$ ($k_z = 0$) and recognizing that $\phi' = 0$ in (3.57) results in the following matrix equation:

$$\begin{pmatrix} k'_x \\ k'_y \end{pmatrix} = \begin{pmatrix} \cos\alpha_z & \sin\alpha_z \\ -\sin\alpha_z & \cos\alpha_z \end{pmatrix} \begin{pmatrix} k'\sin\theta' \\ k'\cos\theta' \end{pmatrix} . \tag{3.62}$$

Making use of (3.58)-(3.61) gives the final results:

$$k'_x = \frac{k_y}{k} k' \sin\theta' + \frac{k_x}{k} k' \cos\theta' , \tag{3.63}$$

$$k'_y = -\frac{k_x}{k} k' \sin\theta' + \frac{k_y}{k} k' \cos\theta' . \tag{3.64}$$

It is imperative to realize that in this case θ' is the in-plane scattering angle between the 2D wavevectors $\mathbf{k}$ and $\mathbf{k}'$. (Note that the derivation of (3.62) can also of course be done by using a 2D rotation matrix whereby the coordinate system is rotated to align either the k_y or k_x components of the initial wavevector with $\mathbf{k}$).

3.12 Inclusion of Degeneracy (Pauli Exclusion Principle)

The scattering rates presented in Chapter 2 have been derived under the assumption that the occupancy of a final state $\mathbf{k}'$, represented by the normalized distribution function, $f(\mathbf{k}')$, is assumed to be initially equal to zero. In actuality though, the probability per unit time of scattering from state $\mathbf{k}$ to $\mathbf{k}'$, must be written as

$$P(\mathbf{k},\mathbf{k}') = S(\mathbf{k},\mathbf{k}')[1 - f(\mathbf{k}')] \quad , \tag{3.65}$$

where $S(\mathbf{k},\mathbf{k}')$ is the transition probability given in (2.2) and the occupancy factor $[1-f(\mathbf{k}')]$ indicates the probability that the final state is not occupied. Consequently, the value of the occupancy factor is dictated by the PEP, which states that only two particles (electrons) can occupy a quantum mechanical state at the same time and that these two particles must differ by their spin quantum numbers.

Fortunately though, the scattering rates do not need to be re-derived. In fact, incorporation of the PEP into the EMC is easily accomplished in consideration of the theory of the Fermi gas. This theory dictates that the volume that an electron must occupy in momentum space, assuming a 3D system, is given by $(2\pi)^3/V$ where V is the real-space volume of the system under consideration. Therefore, the maximum number of electrons allowed to occupy a "cell" of volume Ω_c^{3D} in momentum space is given as,

$$N_c^{3D} = \frac{2\,\Omega_c^{3D}}{(2\pi)^3/V} \quad , \tag{3.66}$$

where the factor of 2 accounts for the spin degeneracy and the term

$$\Omega_c^{3D} = \Delta k_x \Delta k_y \Delta k_z \quad , \tag{3.67}$$

indicates that k-space is descritized in Cartesian coordinates (any convenient coordinate system could, in principle, be used).

As discussed in [67], determining the scattering rate from an initial state $\mathbf{k}$ to $\mathbf{k}'$ using (3.65) is problematic since the occupancy $f(\mathbf{k}')$ is not known *a priori*. However, in the EMC selecting the final state is easily accomplished, while retaining the previously given scattering rates, by utilizing a random-number rejection technique described as follows (considering only 3D transport for the moment).

After every free flight or scattering event in the EMC, a random number is generated, uniformly distributed between 0 and 1. This random number is compared to the value of the normalized distribution function describing the occupancy of a discrete region of k-space, determined by normalizing (3.66). If the random number is less than the value of the distribution function, the wavevector $\mathbf{k}$ is updated as dictated by the drift or scattering event. Otherwise, the drift or scattering event is treated as a self-scattering event in which no change is made to the particle dynamics.

For simulations in 3D k-space ("bulk" simulations) the volume in (3.66) is given simply as

$$V = \frac{N_p}{\rho_{3D}} \quad , \tag{3.68}$$

where N_p the number of simulated particles used in the EMC, and ρ_{3D} is the electron density in the system.

For the k-space simulation of transport in a quasi 2D electron gas, the treatment is directly analogous. In this case, N_c^{2D} is given as

$$N_c^{2D} = \frac{2\Omega_c^{2D}}{(2\pi)^2 / A} \quad , \tag{3.69}$$

where $\Omega_c^{2D} = \Delta k_x \Delta k_y$. For the 2D system, the area is of interest whereby

$$A = \frac{N_p}{\rho_{2D}} \quad . \tag{3.70}$$

To incorporate the PEP in modeling transport in a quasi 2D gas, such as occurs in a HEMT, the "area" noted above is defined to be the in-plane transport area of the device (device length × device width). Use of this approximation is justified by assuming that the in-plane wavefunctions are slowly varying over the device, allowing a semi-classical treatment. This assumption is admittedly somewhat dubious, but allows a circumvention of the numerical issues cited below. The "width" is chosen rather arbitrarily, but sufficiently large to allow enough particles in the simulation to give statistically meaningful results.

3.13 Inclusion of Spin Dynamics

In III-V compounds, the bulk inversion asymmetry (BIA) that exists due to the polar nature of the compound induces a spin-orbit coupling of a carrier's magnetic moment with an effective magnetic field that is perpendicular to both the electric field of the polar dipole moment and the electron's momentum (i.e., wavevector). Spin relaxation and phase-breaking occur when momentum scattering alters the carrier's wavevector. Hence the direction of the effective magnetic field, about which the carrier's spin magnetic moment precesses, is altered.

The Hamiltonian of this interaction, known as the BIA or Dresselhaus interaction [68], is given by

$$\mathbf{H}(\mathbf{k}) = \frac{1}{2}\hbar\boldsymbol{\sigma}\cdot\boldsymbol{\Omega}(\mathbf{k}) \quad , \tag{3.71}$$

where

$$\mathbf{\Omega}(\mathbf{k}) = \alpha\hbar^2 \cdot \left(2m^* E_g\right)^{-1/2} \boldsymbol{\kappa} \quad , \tag{3.72}$$

is the precession frequency (called the Larmor frequency) about the direction of the effective magnetic field given by $\boldsymbol{\kappa}$ which is written

$$\boldsymbol{\kappa} = \left[k_x\left(k_y^2 - k_z^2\right), k_y\left(k_y^2 - k_z^2\right), k_{zx}\left(k_x^2 - k_y^2\right)\right] \quad , \tag{3.73}$$

In (3.72) α is a dimensionless parameter ($\alpha \approx 0.07$ for GaAs).

Of technological significance is a similar effect that can be engineered in heterostructures by inducing a Structural Inversion Asymmetry (SIA) in the quantization direction of the device, as discussed in the Introduction. As in the BIA case, this results in a carrier spin-orbit coupling with an effective magnetic field that is perpendicular to both the carrier's momentum and the non-zero value of the electric field resulting from the SIA. Varying this field, for example, by changing the gate voltage of the FET-type device, modulates the spin precession rate (and hence the time and length of decoherence). This is known as the Rashba effect [26], as also discussed in the Introduction. Today, a major difficulty in the realization of these devices lies in the difficulty of injecting spin-polarized carriers into the transport channel. However, in a simulation the initial spin distribution can be known, a priori, as is done in this work [29, 69].

Collectively, BIA and SIA spin scattering is known as D'yakanov-Perel (DP) scattering and is the dominant spin-scattering mechanism in III-V compounds at room temperature. However, DP scattering cannot be implemented in the EMC as another “ordinary” momentum scattering mechanism in the scattering tables. This is because the precession frequency of an electron's magnetic moment is usually less than or on the order of the momentum scattering rate. Spin scattering should therefore be treated at each free flight step. A convenient way of dealing with the problem, which is utilized in this work, is due to Saiken et al., [70], as will be discussed next.

Recall that the Pauli matrices denote the matrix representation of the electron's spin operator $\mathbf{S}$ and yield the expectation of observing the direction of the electron's magnetic moment along a particular axis. A 2×2 density matrix for an electron (or any another spin ½ particle) can then be written as a combination of the Pauli matrices as

$$\rho = a_o I + a_x \sigma_x + a_y \sigma_y + a_z \sigma_z \quad , \tag{3.74}$$

where σ_i are the usual Pauli spin matrices, the a_i are complex coefficients, and I is a 2×2 unitary matrix. Elementary density matrix algebra allows (3.74) to be re-written,

$$\boldsymbol{\rho} = \frac{1}{2}\left(\mathbf{I} + \boldsymbol{\sigma} \cdot \mathbf{P}\right) \quad , \tag{3.75}$$

where the polarization vector $\mathbf{P} = \langle \boldsymbol{\sigma} \rangle$ denotes the expectation value of an electron's spin angular momentum. Expanding (3.75) gives, at time t_0,

$$\boldsymbol{\rho}(t_0) = \frac{1}{2}\begin{pmatrix} 1 + P_z(t_0) & P_x(t_0) - iP_y(t_0) \\ P_x(t_0) + iP_y(t_0) & 1 - P_z(t_0) \end{pmatrix} \quad . \tag{3.76}$$

Then, from standard quantum mechanics, the equation of motion of the density operator, (3.76), is given as,

$$\boldsymbol{\rho}(t) = \mathbf{U}^{+}(t,t_0)\boldsymbol{\rho}(t_0)\mathbf{U}(t,t_0) \quad , \tag{3.77}$$

where

$$\mathbf{U}(t,t_0) = \exp\left(-\frac{i}{\hbar}(t-t_0)\mathbf{H}_{SO}\right) \quad , \tag{3.78}$$

is the time evolution operator. (3.78) is valid provided that H_{SO} is independent of time over the range $t-t_0$. Thus, combining (3.77) and (3.78) one obtains

$$\rho(t+\delta t) = e^{-i(H_R+H_D)\delta t/\hbar}\rho(t)e^{i(H_R+H_D)\delta t/\hbar} \quad . \tag{3.79}$$

The terms H_R and H_D in (3.79) refer to the Rashba and Dresselhaus contributions, respectively, to the momentum-dependent spin-splitting in the Hamiltonian. These terms assume a form identical to that of (3.71) and are typically recast for quasi-2D systems as

$$H_R = \eta\left(k_y\sigma_x - k_x\sigma_y\right) \quad , \tag{3.80}$$

$$H_D = \gamma\left(k_y\sigma_y - k_x\sigma_x\right) \quad , \tag{3.81}$$

where η and γ are proportionality constants. The nature of the proportionality constant, η in (3.80) is controversial [71]. However, it is dependent on local electric fields in the quantum well, even if only to a small extent. In the event that the device channel is not oriented along [1,0,0], the angular dependence of the BIA effective magnetic field is accounted for in the Dresselhaus term by replacing (3.81) with [72],

$$H_D = \gamma\left(k_y\sigma_y - k_x\sigma_x\right)\cos(2\xi) + \gamma\left(k_y\sigma_x + k_x\sigma_y\right)\sin(2\xi) \quad , \tag{3.82}$$

where the angle ξ denotes the angle between the device channel and the [1,0,0] crystallographic axis.

Hence, for each 2D carrier (3.79), (3.80) and (3.81) (or (3.82) as appropriate) are updated at each time-step δt in the EMC, since the k terms in (3.80) and (3.81) are in turn updated after a carrier undergoes drift or momentum scattering. An average spin polarization of the ensemble, in real-space, can then be determined.

3.14 Contact Modeling

In the semi-classical, particle-based simulation of semiconductor devices it is only feasible, from a computational perspective, to consider a small cross section of the actual device, the *active region*. This is necessary because the entire structure has dimensions on the order of hundreds of microns, or more likely of millimeters. Accordingly, the domain of the simulation needs to be truncated with the appropriate electrostatic boundary conditions.

At some boundaries of the simulation domain, where it can be assumed that no net current is flowing through the boundary, Neumann boundary conditions are employed. As discussed previously in connection with the Poisson equation, these conditions imply that the electric field across such a boundary interface is set equal to zero. Numerically, this is achieved by defining the potential of the first grid cell immediately "outside" the simulation domain as equal to the potential of the grid cell immediately adjacent to the contact cell, within the simulation domain. Doing this implies a modification of the Poisson equation given by (3.17) in which the coefficient of the grid cell adjacent to the contact cell within the simulation domain is multiplied by a factor of 2.0. In this case setting $\phi_{i+1} = \phi_{i-1}$ results in one of these terms vanishing, while the coefficient of the surviving term doubles. On the other hand, the maintenance of a particular region at a constant potential, as is done for ohmic or Schottky contacts, is known as applying Dirichlet Boundary conditions.

For the case of ohmic contact cells in which the carriers are considered to be 3D (i.e., no quantum mechanical modeling) charge neutrality must be maintained in these regions since they are considered to be in thermal equilibrium, even when current is flowing. Accordingly, the number of 3D carriers that must be maintained in an ohmic contact cell depends on the density of ionized donors or acceptors in that cell. Therefore, immediately prior to the periodic update of the electrostatic potential, carriers must be either added or subtracted from these contact cells to obtain the charge neutral condition. The net gain of carriers in a cell, per unit timestep, is essentially a measurement of the current through the contact cell. However, for ohmic contact cells in which the carriers are to be treated as 2D, one cannot simply maintain charge neutrality in accordance with the doping concentration since consideration must be given to the quantum mechanical distribution of carriers.

In this work, 2D contact modeling is achieved by maintaining a 2D carrier concentration that is equal to the equilibrium carrier concentration at the contacts, at each Poisson/SWE timestep. This is determined from the self-consistent Schrödinger-Poisson equations discussed previously. Furthermore, contact cells for 2D particles are not treated as discrete cells along the direction of quantization (e.g., the heterostructure growth direction), since an exact position is quantum mechanically ill-defined in this direction. However, since a 3D distribution of carriers is needed for solving Poisson's equation, the number of 2D carriers, per sub-band, per region of quantization (typically one "column of cells" in the semiconductor growth direction at the lateral edges of the simulation domain defined as a "contact column" along the jth channel slice) is distributed along the quantization direction as indicated by (3.7). For each subband, (3.7) is written

$$N_n^{2D}(i,j,k) = (n_{2D})_n \, \varphi_n^*(i)\varphi_n(i)\Big|_{j,k} \quad . \tag{3.83}$$

In this way, the 2D charge is effectively "smeared" over the 3D domain consistent with the quantum mechanical probability of finding the particle at some location with respect to the direction of quantization.

For HEMT structures, a more rigorous treatment of contacts must take into consideration the fact that source and drain contacts are typically fabricated on the top edge of the device, above the cap layers. The usual interpretation of quantum mechanics then dictates that the carriers must tunnel through the heterostructure cladding layers to and from the quantum well formed in the channel layer. It is common practice, however, to avoid dealing with the tunneling problem altogether by using side contacts for modeling HEMT structures, wherein the carriers are treated as 3D. Furthermore, Dirichlet boundary conditions are typically applied to these regions and sufficient contact doping is maintained to negate the depletion effects (drops in electrostatic potential) associated with the abrupt change in potential that can occur in the vicinity of the contact cell.

In this work, a tunneling model has not yet been implemented. Rather, modified boundary conditions are introduced that eliminate the "artificial" potential drop associated with the usage of side contacts. The scheme is depicted in Figure 3.8 for a prototypical HEMT structure. In this work, it is postulated that the regions nearest the lateral edges of the device in Figure 3.8 (the dark shaded areas) are in a state of quasi thermal equilibrium by making the argument that tunneling current is nearly "vertical" from the channel to the cap layers (and vice versa). Neumann boundary conditions can then be applied at the lateral edges of the device and the equilibrium carrier density can be maintained in these regions when a bias is applied to the source and drain contacts at the top surface of the cap layers.

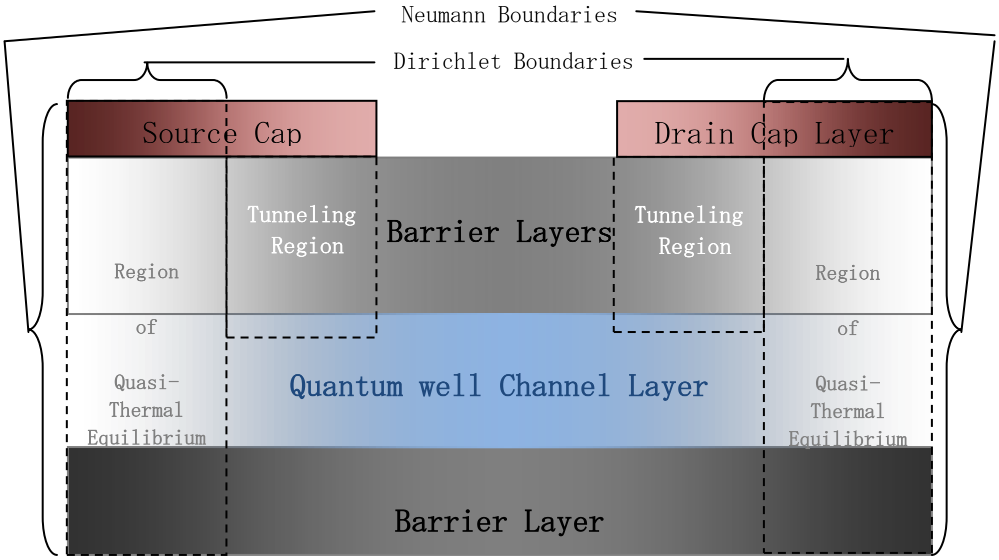
Neumann Boundaries
Dirichlet Boundaries
Source Cap
Drain Cap Layer
Tunneling Region
Barrier Layers
Tunneling Region
Region of Quasi-Thermal Equilibrium
Region of Quasi-Thermal Equilibrium
Quantum well Channel Layer
Barrier Layer

Figure 3.8 Boundary conditions imposed on HEMT during EMC simulation, in the absence of a tunneling model. The areas labeled "tunneling region" indicate where tunneling would occur in an actual device.

4. Simulation Results

4.1 Model Verification

As with the construction of any large computer code, it is first necessary to verify that every portion of the code has been correctly implemented at each step of the development process. Accordingly, several simulations were conducted in momentum space before applying the code to device simulation. These simulations validated the implementation of the scattering rates and tables discussed in Chapter 2, and the drift, scattering, and final state selection routines discussed in Chapter 3.

In Figure 4.1, the simulated velocity vs. time characteristics are plotted for bulk GaAs at T=300K, using scattering parameters discussed in [63]. Electrons are assumed to have been "injected" into the system at time $t = 0$ with a Maxwell-Boltzman energy distribution. The results are in excellent agreement with those indicated in [63] and show that the EMC is successfully capturing the transient effects of velocity overshoot for fields greater than about 3kV/cm.

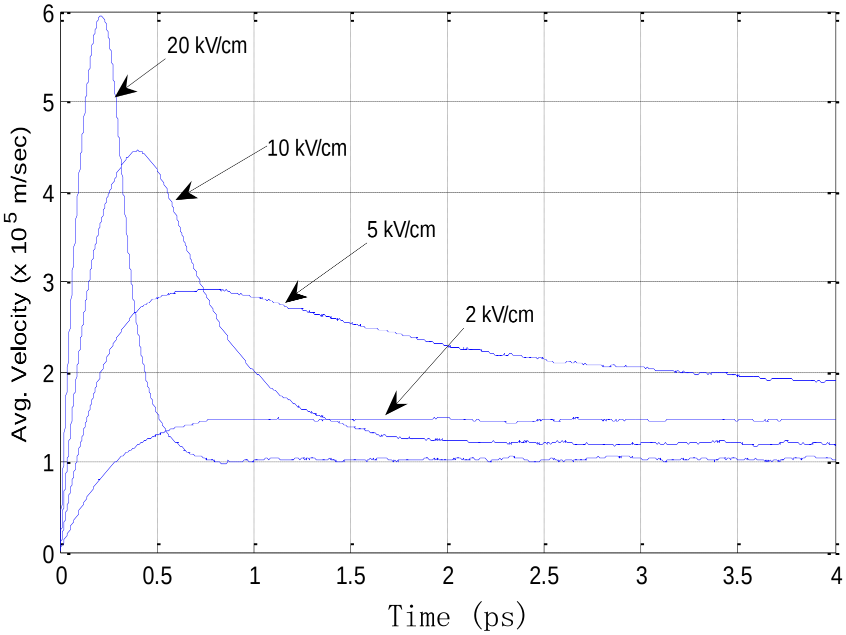

Figure 4.1 Bulk GaAs EMC simulation. T=300K. 3-valley model. (Γ, L, X valleys) Scattering mechanisms included are 3D polar optical phonon, acoustic deformation potential, non-polar optical phonon, and ionized impurity scattering. The impurity concentration is 1.0 x $10^{14}/\text{cm}^3$.

In Figure 4.2, the velocity field characteristics of bulk GaAs from the EMC simulation are presented as an additional check on the implementation of the 3D portion of the code. These results are obtained via the steady state portion of the velocity vs. time data in Figure 4.1 as the electric field is incremented in units of 1kV/cm. The location of the peak in the curve is consistent with the expected Negative Differential Conductivity (NDC) phenomenon in GaAs. The NDC is caused by electrons being scattered from the Γ valley to the L valley where the effective mass is on the order of three times greater; hence slowing the average carrier velocity. The noise in the curve at higher fields is statistical. A smoother curve would result if one utilized more particles and longer time-averaging of the carrier velocity. Comparable test results for bulk GaAs were also obtained when the 2D scattering mechanisms were implemented in the EMC.

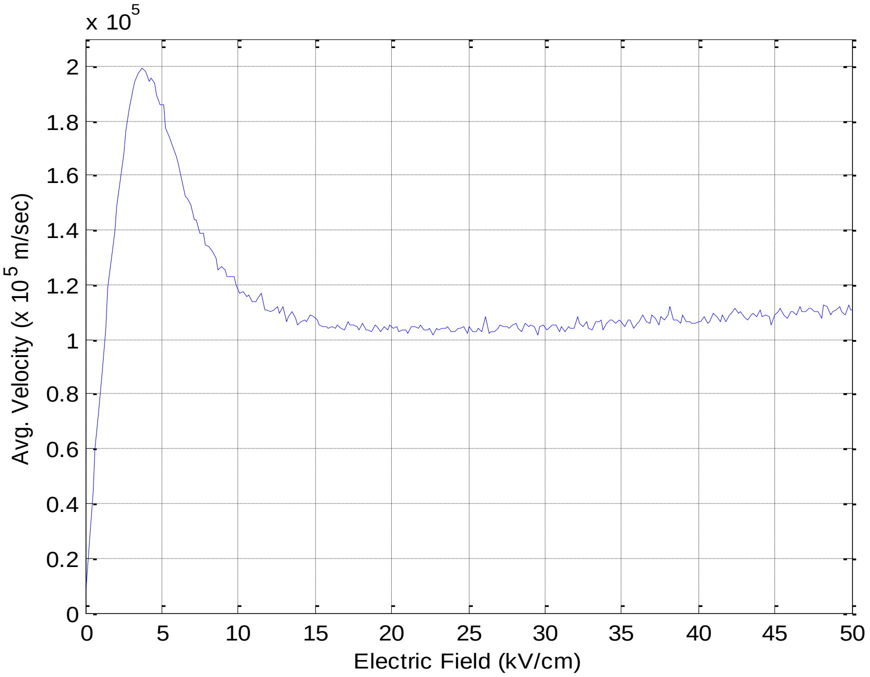

Figure 4.2 Bulk GaAs velocity field characteristics from EMC simulation. T=300K. 3-valley model. (Γ, L, X valleys). The scattering parameters are the same as those depicted in Figure 4.1.

4.2 Intel Corp. HEMT Simulation

As discussed in [17], III-V InGaAs HEMT structures are attractive candidates for future use in high frequency, low power applications. Compared to advance strained silicon MOSFETs, such devices have exhibited a 20-65 % gain in drive current at Vcc bias of 0.5-1.0 V. This is despite the fact that carrier densities in the active region of the device are roughly half that of the comparative silicon devices. In order to exploit the full capability of such HEMTs accurate device simulation is crucial. Hence, EMC simulations were conducted on the structure depicted in Figure 4.3 (see next page). This structure resembles the

HEMT of Figure 1 in [17], to the extent possible that information was provided to this author in consideration of proprietary concerns. Consequently, some structural dimensions, such as the thickness of the beveled SiN regions, cap layer doping, and the lack of delta-doping directly under the gate, were assumed. Additionally, due to the numerical problems with simulating a delta-doped layer, the delta-doping was "smeared" over a 1 nm region (typically 1-2 grid cells) as depicted in Figure. 4.3.

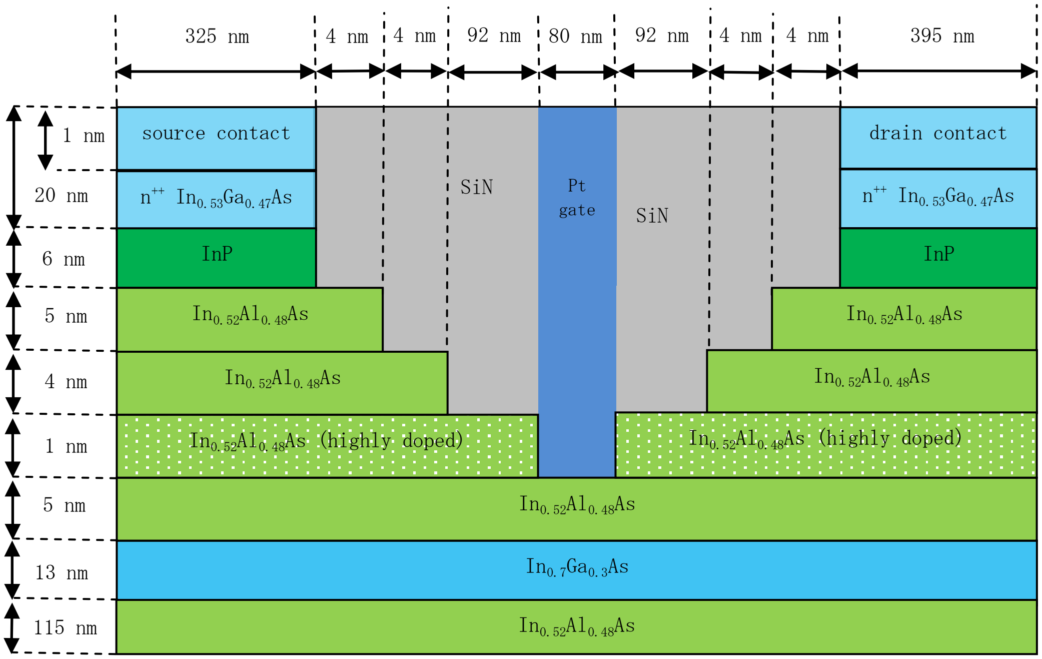
325 nm
4 nm
4 nm
92 nm
80 nm
92 nm
4 nm
4 nm
395 nm
1 nm
20 nm
6 nm
5 nm
4 nm
1 nm
5 nm
13 nm
115 nm
source contact
drain contact
n^{++} $In_{0.53}Ga_{0.47}As$
n^{++} $In_{0.53}Ga_{0.47}As$
SiN
Pt gate
SiN
InP
InP
$In_{0.52}Al_{0.48}As$
$In_{0.52}Al_{0.48}As$
$In_{0.52}Al_{0.48}As$
$In_{0.52}Al_{0.48}As$
$In_{0.52}Al_{0.48}As$ (highly doped)
$In_{0.52}Al_{0.48}As$ (highly doped)
$In_{0.52}Al_{0.48}As$
$In_{0.7}Ga_{0.3}As$
$In_{0.52}Al_{0.48}As$

Figure 4.3 Intel Corp. HEMT simulated structure.

EMC Simulations of the gate region heterostructures in Figure 4.3, in momentum-space, were then conducted. In such simulations, the 2D transport in the infinite 2D plane formed by the quantum well of the InGaAs channel was considered. As such, the potential profile used in the momentum-space simulation corresponded directly to the center "slice" of the device depicted in Figure 4.3

comprising the entire 37nm Pt Gate, 5nm $In_{0.52}Al_{0.48}$ As cladding layer, 13nm $In_{0.7}Ga_{0.3}$ As channel, and 115nm $In_{0.52}Al_{0.48}$ As "substrate" layer. In doing these simulations, real-space transport was still allowed in the growth direction.

In Figure 4.4 the corresponding velocity field characteristics are presented for various roughness scattering parameters, as discussed in section 2.4.4. Additionally, results are presented in Figure 4.5 for various 2D alloy scattering parameters, at a fixed rms roughness value of 0.6nm and auto-correlation length of 1.5 nm.

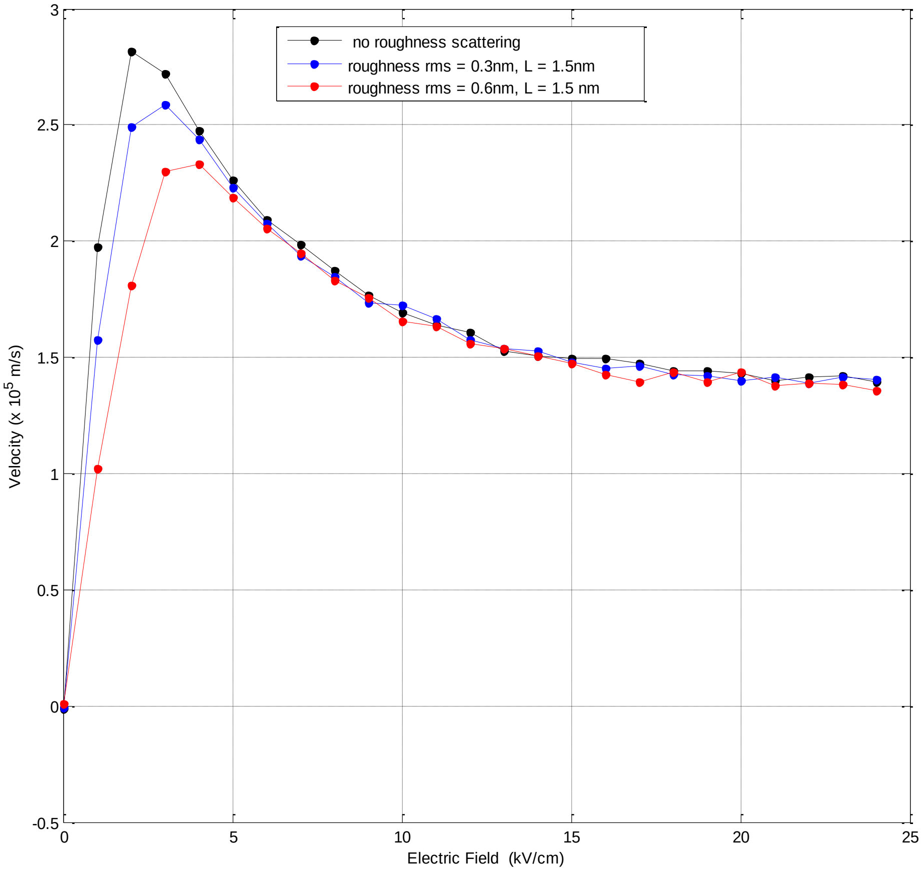

Figure 4.4 Velocity field characteristics corresponding to the gate heterostructure of Figure 4.3 as a function of the interface roughness height.

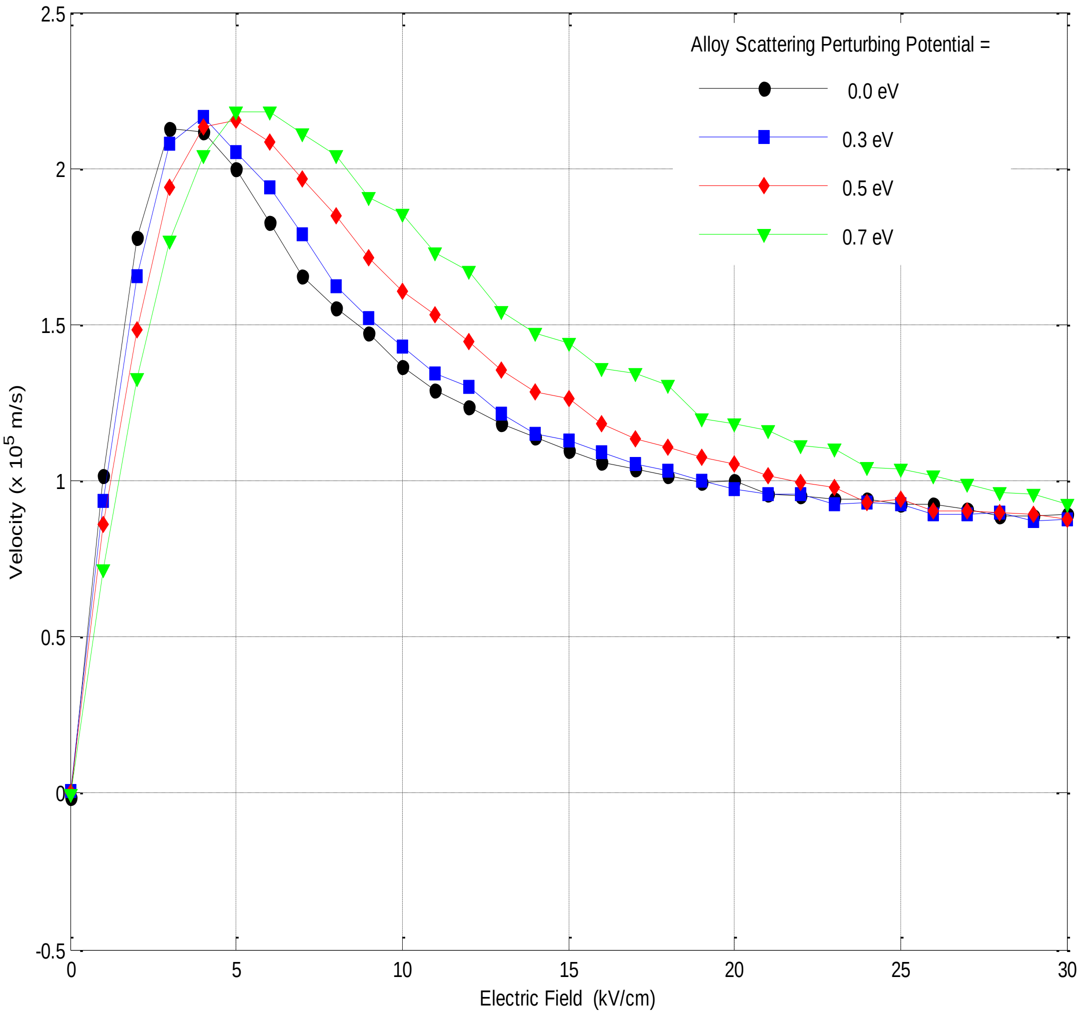

Figure 4.5 Velocity field characteristics corresponding to the gate heterostructure of Figure 4.3 as a function of the alloy disorder potential at roughness height of 0.6nm and length of 1.5nm.

Although a root mean square (rms) roughness height of 0.6nm is considered to be very large, it is only the comparative effects of the alloy parameters that are of interest in this case.

In the results of Figures 4.4 and 4.5 average effective masses were used in determining the 2D scattering rates, by weighting the contributions from each mesh point in the growth direction with the quantum mechanical probability of a 2D carrier being at that location. However, when device simulations were conducted, numerical instabilities mandated that the contribution to the effective mass from the 13nm $In_{0.7}Ga_{0.3}$ As channel be used. As shown in Figure 4.6, this approximation is justified, since both schemes for determining the 2D effective mass give nearly identical results.

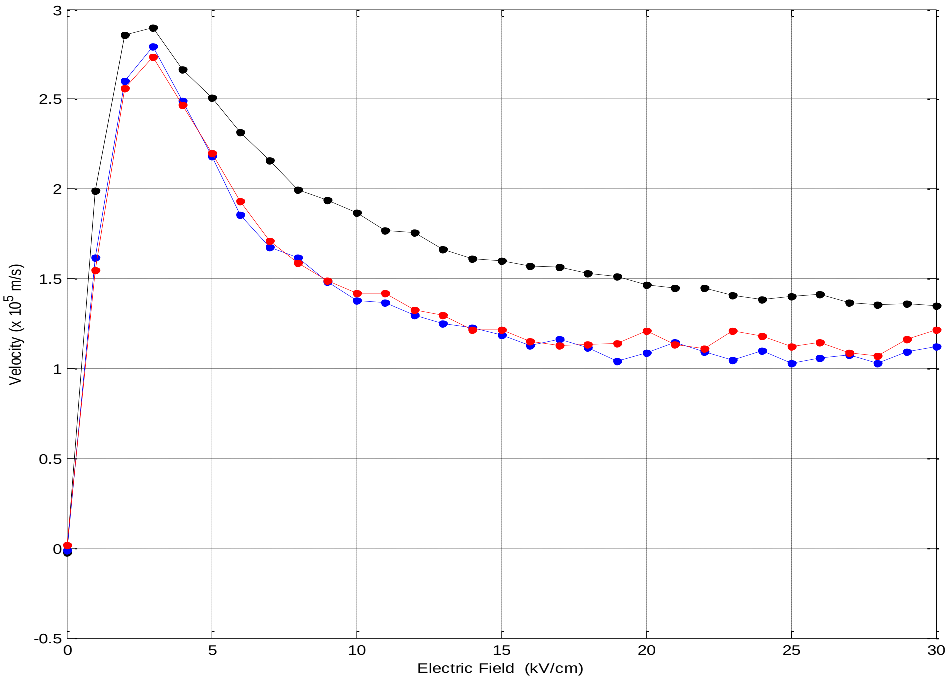

Figure 4.6 Lower curves (red, blue): Effect of two different 2D effective mass calculation schemes on velocity field results for the gate heterostructure of Figure 4.4; Red curve: Average 2D effective mass used.; Blue curve: $In_{0.7}Ga_{0.3}As$ effective mass used; Both lower curves assume roughness rms = 0.3nm Roughness L = 1.5nm. Top curve: (black) No roughness scattering, average effective mass used. For all cases T=300K and the Pauli Exclusion Principle was not applied.

Next, device simulation results are presented for the structure depicted in Figure 4.3. Unless otherwise noted, in the results that follow, the scattering parameters are exactly as described in Chapter 2. e.g., the rms roughness length is taken as 0.3 nm, the autocovariance length as 1.5nm, the alloy perturbing potential is given as $\Delta V = 0.5\mathrm{V}$, and the lattice constant is taken as $5.8\,\overset{\circ}{\mathrm{A}}$

In Figure 4.7, I_d vs. V_{ds} results are plotted for the EMC simulation of the structure in Figure 4.3, and the related experimental results as depicted in [17]. The corresponding I_d vs. V_{gs} curves, at V_{ds}=0.5V, are presented in Figure 4.8.

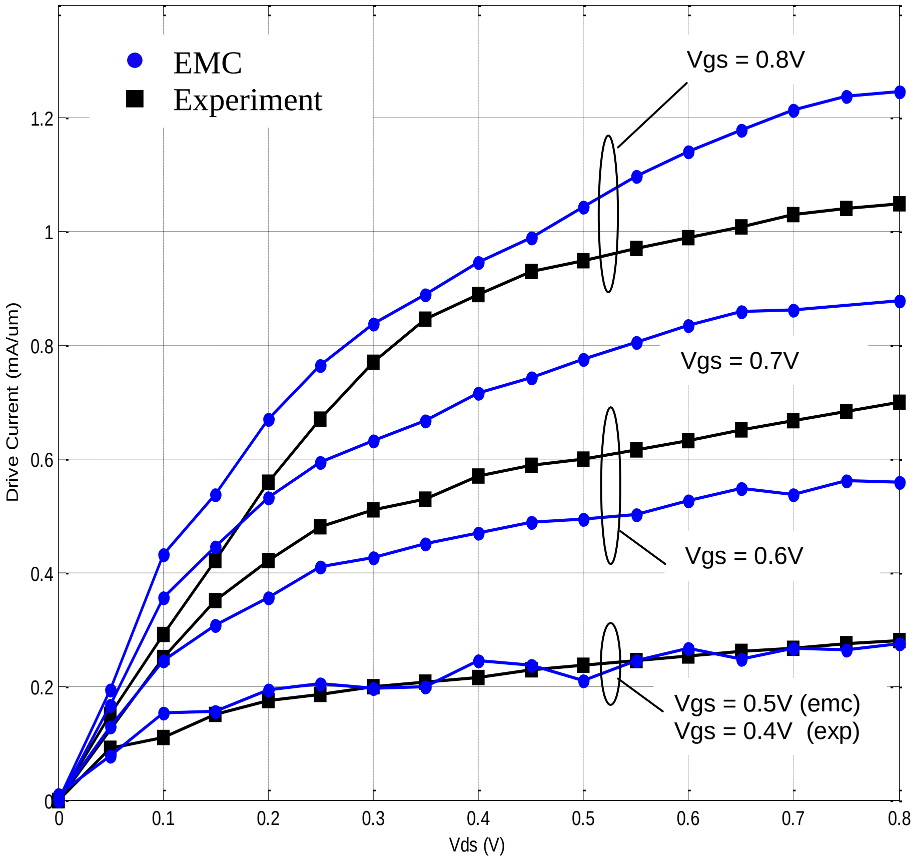

Figure 4.7 EMC simulation of I_d vs. V_{ds} curves for the structure depicted in Figure 4.3, and the corresponding experimental results of [17].

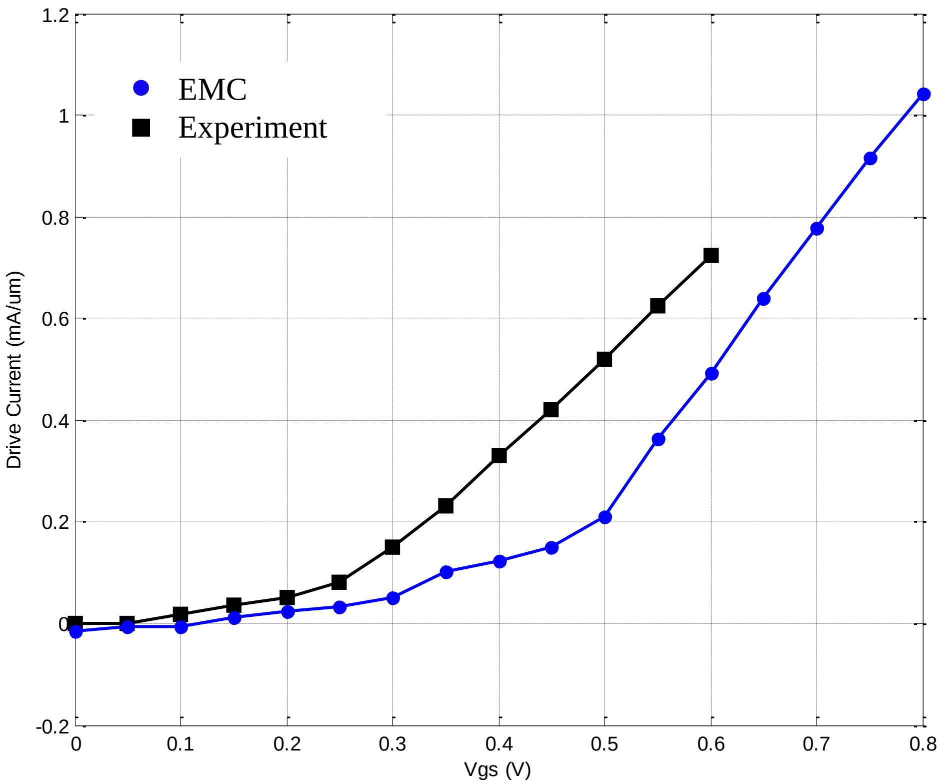

Figure 4.8 Simulated I_d vs. V_{gs} curves for the structure depicted in Figure 4.3, and the corresponding experimental results of [17], at $V_{ds} = 0.5V$, $T = 300K$.

In Figure 4.7 and Figure 4.8 the "raw" V_{gs} value is depicted as opposed to subtracting out the threshold voltage from V_{gs}. This was done in order to observe the roughly 0.2V difference in threshold voltage V_T between the two cases, as can be observed by extrapolating to the x-axis the linear portions of the curves in Figure 4.8. As indicated in Figure 4.7 and Figure 4.8, the simulation results are in reasonable agreement with experiments, and differences are attributed to the following reasons. First, in the EMC model the domain of the SWE did not extend to the gate region. Accordingly, it is believed that the gate control over the device is "sluggish" due to an imposed inaccurate electrostatic condition in the gate region of the QW channel. Second, the exact structural specifications of the

Intel experimental devices, notably in the gate region were not provided to this author. Third, the Schottky barrier for the platinum gate was estimated to be 0.8V. However, the exact value of the barrier was not known. Furthermore, in Figure 4.7, discrepancies between the EMC and experimental results may be somewhat diminished by slightly varying the scattering parameters. Such effects will be discussed later in this section.

In Figure 4.9, the transconductance is calculated from the EMC result in slope of the I_d vs. V_{gs} curve in Figure 4.8. The "noise" is due to the coarseness of the descritized dI_d/V_{gs} function. The peak of the transconductance occurs at V_{ds} =0.5 V, consistent with the result in [17], whereby the reported experimental peak in the transconductance was $\approx 1800\text{mS}/\text{um}$.

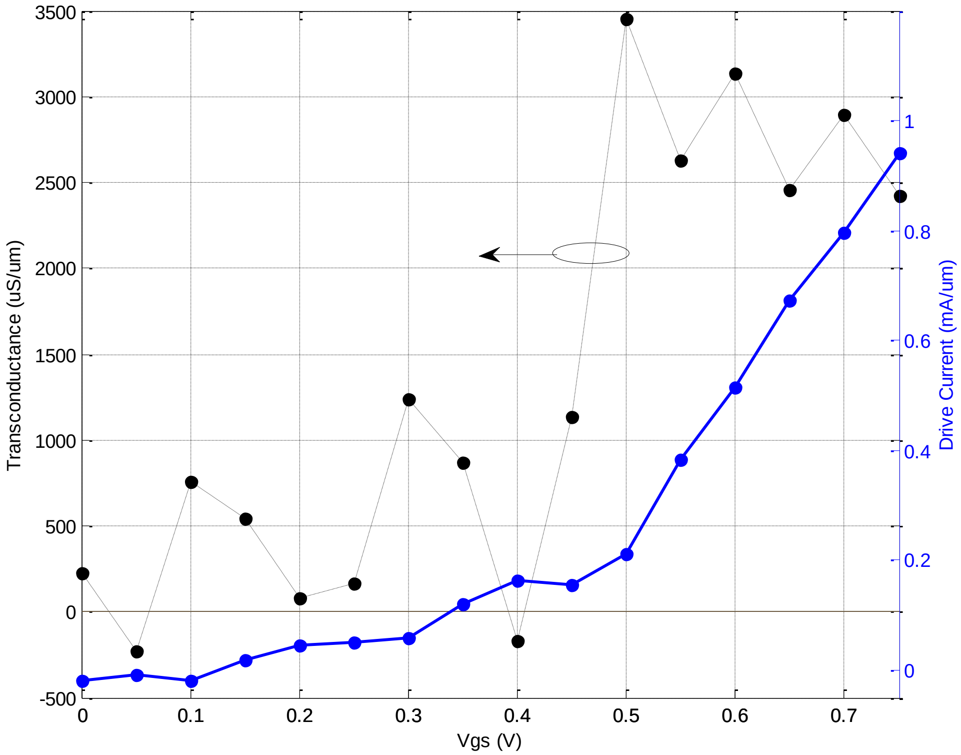

Figure 4.9 Calculated transconductance based on Figure 4.8 EMC curve.

Next, results are presented that emphasize the effects of varying some scattering parameters and device structural attributes.

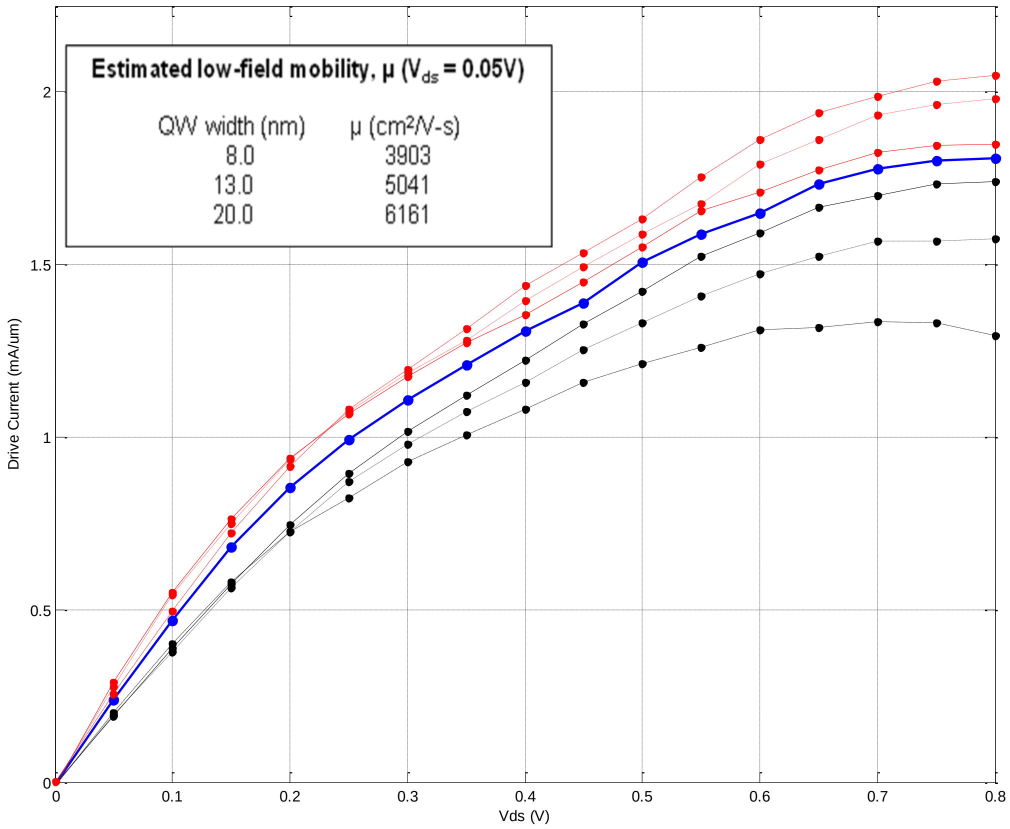

Figure 4.10 Effect of various scattering parameters and quantum well widths on HEMT drive current. Blue curve: roughness rms = 0.3nm, L = 1.5 nm, alloy ΔV = 0.5V QW width = 13nm. All other curves retain these values except for one parameter change as noted. Red solid: roughness rms 0.15nm; Red dotted: Alloy ΔV = 0.15V; Red dashed: QW width = 20nm; Black solid : roughness rms = 0.45nm; Black dotted: alloy ΔV = 0.75V; Black dashed : QW width = 8nm.

In Figure 4.10, the effects of varying the quantum well width and various scattering parameters on the drive current are compared. Based on the extracted velocity from the current, and assuming that an average electric field can be defined in the device as that corresponding to the potential drop over the width of the gate region, the low field mobility is also estimated. Unless otherwise specified all structural and scattering parameters are as previously mentioned.

Next, assorted "diagnostic" results are shown as evidence that the aforementioned results are from a "well behaved" EMC simulator that is working as expected. Figure 4.11 and Figure 4.12 indicate the cumulative amount of charge that has passed through the contacts of the device in Figure 4.3 as time progresses during the simulation. The slope of these curves serves as a measurement of the current. Observance of these types of plots is crucial prior to plotting I-V characteristics, especially if device structural attributes and scattering parameters are altered, in order to insure that the time-domain averaging is in fact being done in the steady state regime. In Figure 4.11 is shown the "charge vs. time" plot for the case of V_{gs}=0.8V and V_{ds} = 0.0V. As expected, once steady state is reached the slopes of the drain and source curves are equal and flat, indicating that no drive current exists at this bias condition. The middle (blue) curve corresponds to the drain contact curve, the lower (red) curve corresponds to the source contact curve, and the upper (green curve) corresponds to the difference of the source and drain curves. In Figure, 4.12, the effect of a finite source drain bias is indicated, whereby the upper (blue) curve corresponds to the drain contact, the middle (red) curve corresponds to the source contact and the lower (green) curve represents the difference between the source and drain curves. In the EMC, measuring the current from these curves entails averaging the slope of the curve at several thousand timesteps at steady state.

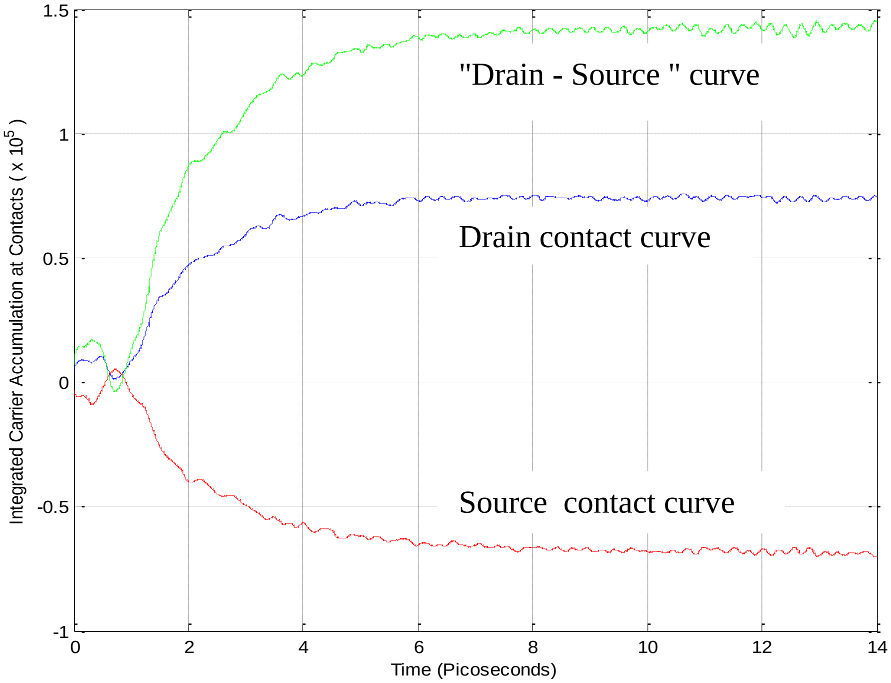

Figure 4.11 Plot of cumulative charge vs. time through the source and drain for the contacts for the device depicted in Figure 4.3. V_{gs} =0.9 V , V_{ds} =0.0 V.

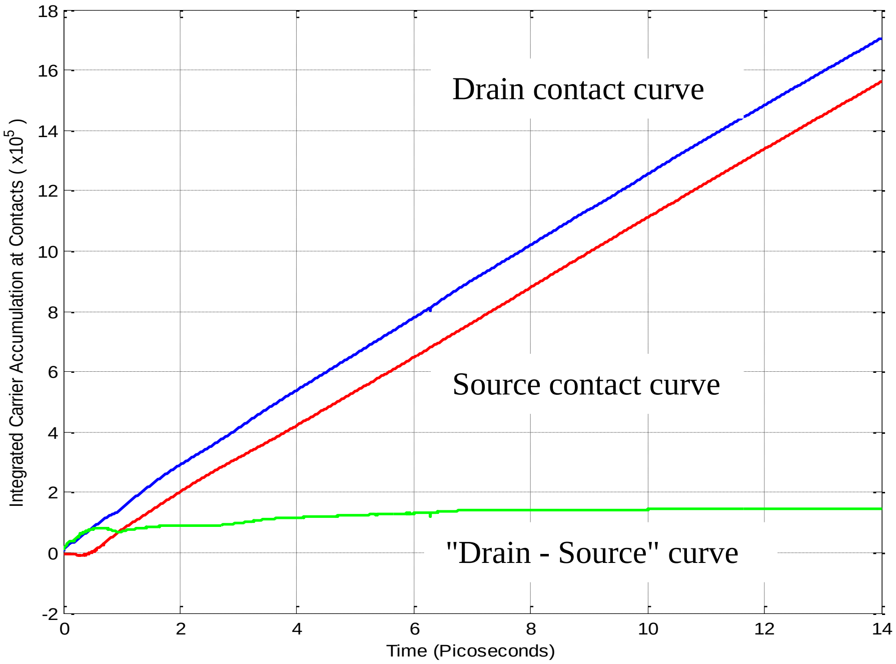

Figure 4.12 Plot of cumulative charge vs. time through the source and drain for the contacts for the device depicted in Figure 4.3. V_{gs} =0.9 V, V_{ds} =0.8 V.

Next, the average carrier velocity and energy is plotted for the device depicted in Figure 4.3, at the bias values corresponding to the peak of the transconductance in Figure 4.9. As expected, as the carriers are accelerated by the strong electric field in the gate region (425nm - 505nm). Scattering then causes the momentum distribution to randomize, while the energy of the carriers remains high until they reach the drain.

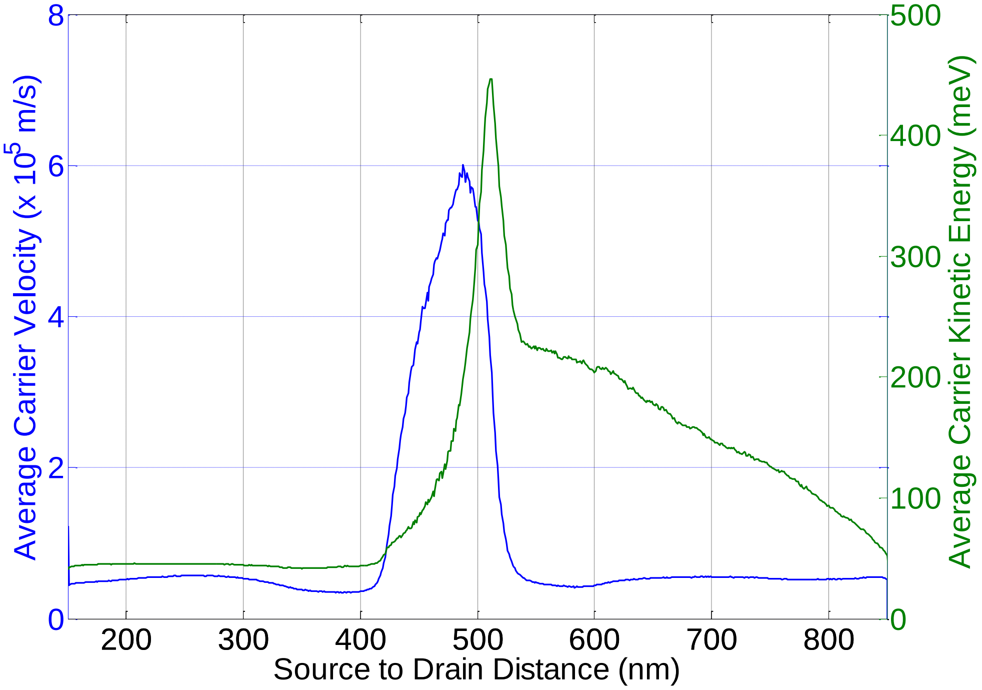

Figure 4.13 Average carrier velocity and energy at V_{gs} = 0.5V, V_{ds} = 0.5V

Next, several plots of potential energy and carrier density over the simulation domain are presented for different bias conditions.

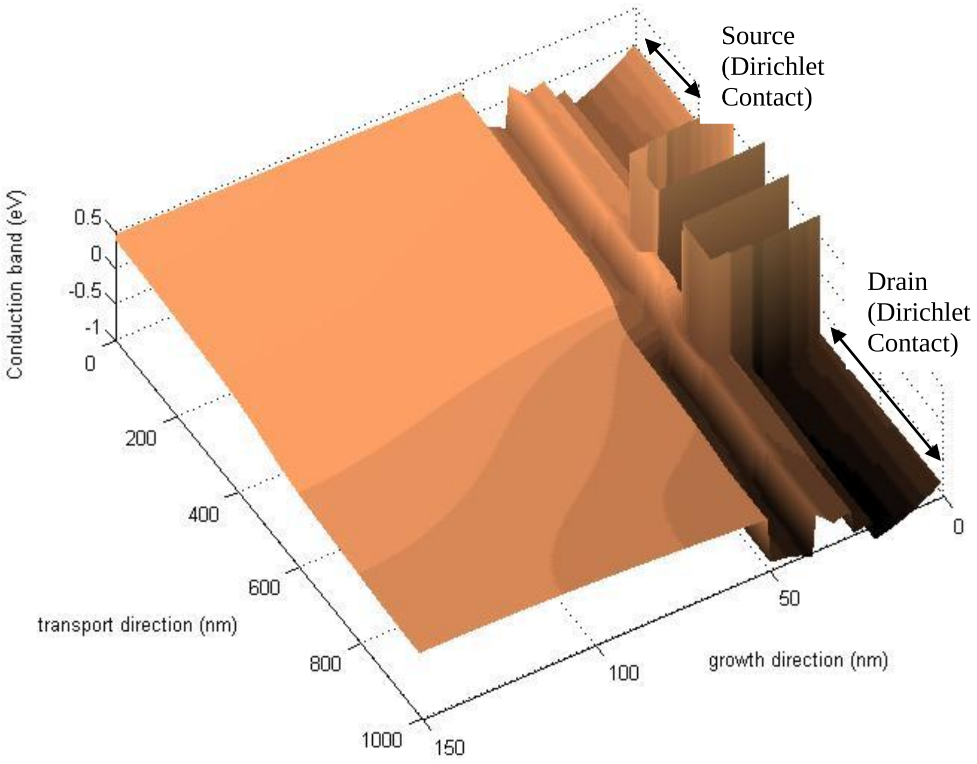

Figure 4.14 Potential energy profile over the simulation domain at V_{gs} =0.8V, V_{ds} =0.8V.

As expected, the potential drop occurs mostly over the gate region. Neumann boundary conditions are imposed at the "bottom" of the device (150nm position along the growth direction) and along the sides of the device. The treatment of the contacts is as described in Section 3.14. The associated carrier density is plotted in Figure 4.15. Real space transfer of carriers near the drain end is observed in Figure 4.15 and Figure 4.16. At low V_{ds}, that effect is not observed as indicated in Figure. 4.17.

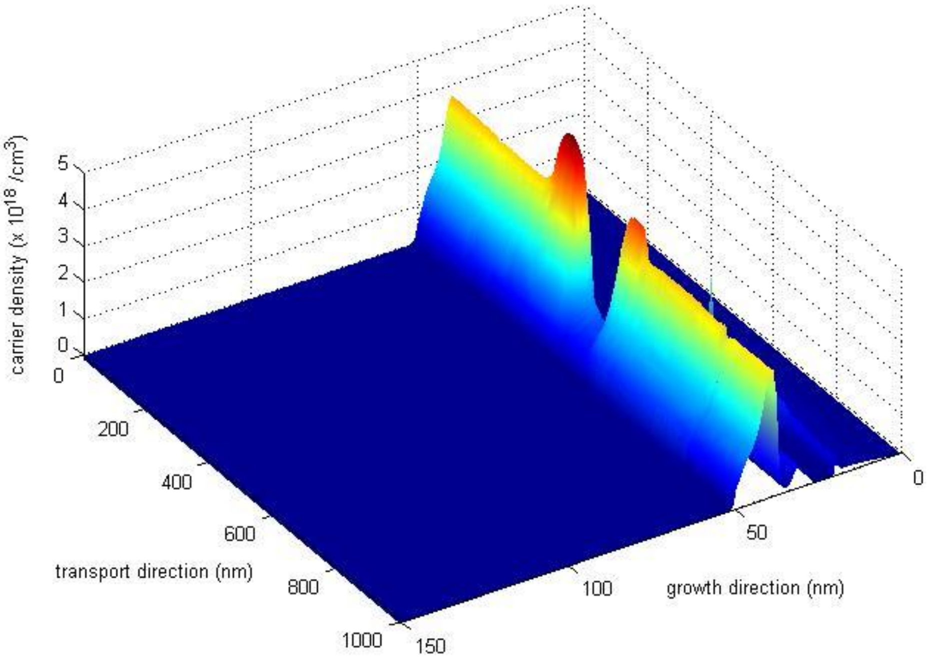

Figure 4.15 Steady-State carrier density at V_{gs} = 0.8V, V_{ds} = 0.8V, corresponding to the potential profile plot in Figure 4.14.

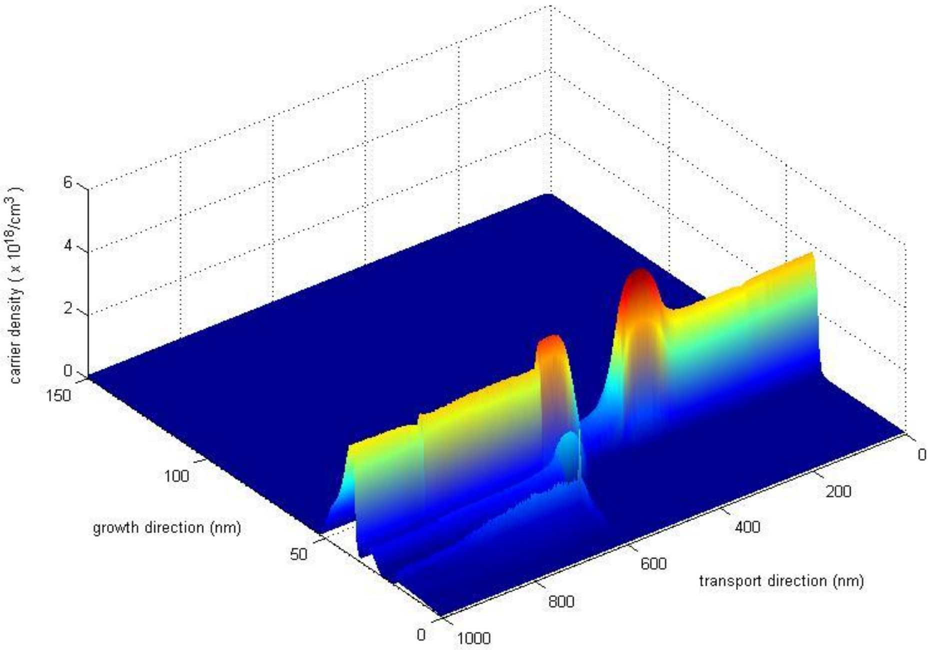

Figure 4.16 Rotated view of Figure 4.15.

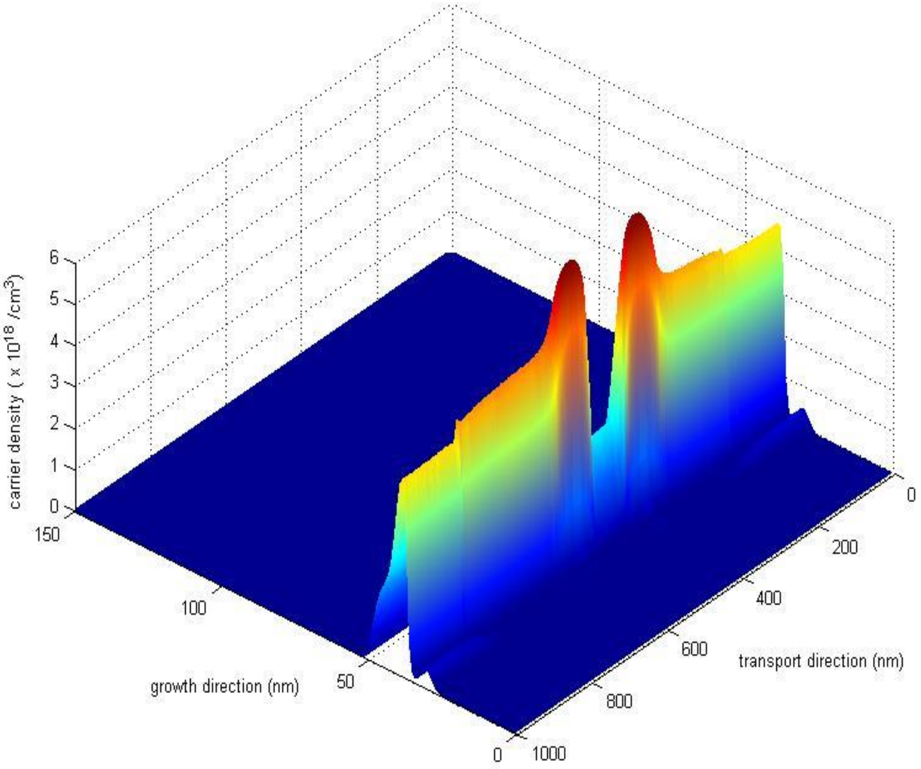

Figure 4.17 Carrier density at V_{gs} = 0.8V, V_{ds} = 0.1V. The figure is oriented in the same way as in Figure 4.16.

4.3 Spintronics Simulation Results

As an extension of the Intel Corp. HEMT modeling described in the last section, the viability of constructing a SpinFET device based upon the Intel HEMT structure is investigated. Earlier spintronics studies by this author were reported in [29, 69]. Accordingly, one previously reported result [29, 69] will be described next, since the methodology for calculating the Rashba and Dresselhaus coefficients [73] in [29, 69] has been retained in this effort to model a SpinFET device based upon the aforementioned Intel structure.

As reported earlier [29, 69], in order to validate the DP approach described in Section 3.11, the temporal evolution of the spin polarization in k-space was modeled, assuming carriers were assigned a particular initial polarization. The system considered was a simple AlGaAS/GaAs modulation doped heterostructure. The Schottky barrier height (0.8V) and doping density were chosen to obtain a ground state subband energy of ~22 meV. The model for the Rashba interaction was given by $\eta = \alpha \vec{E}_z$ where the strength of the interaction was given as being simply proportional to the local electric field in the quantum well (defined as an average value of the electrostatic field over the heterostructure) with $\alpha = 5.3\ eV - \overset{\circ}{A}{}^{2} / V$ for GaAS. The Dresselhauss constant described in Section 3.11 was given, for each subband, as $\gamma_i = \beta \langle k_{z,i}^2 \rangle$ with the Kane BIA parameter given as $\beta = 29.0\ eV - \overset{\circ}{A}{}^{3}$, for GaAs. Furthermore, $k_{z,i}^2$ was calculated via the fact that $k_{z,i} \to -i\nabla_z$, resulting $\eta / \gamma_i \approx 4.0$ for the 1st subband.

As reported in [29], Figure 4.18 shows the effects of varying the square quantum well width on spin relaxation. In this case, spin relaxation is plotted as a function of the ground state energy, which varies inversely with the quantum well width. As expected, the relaxation rate increases with increasing ground state energy (which, of course, implies a decreasing quantum well width). This is because as the quantum well narrows, both the Rashba and Dresselhaus coefficients become greater, as calculated according to [73], resulting in faster dephasing of the spin density matrix.

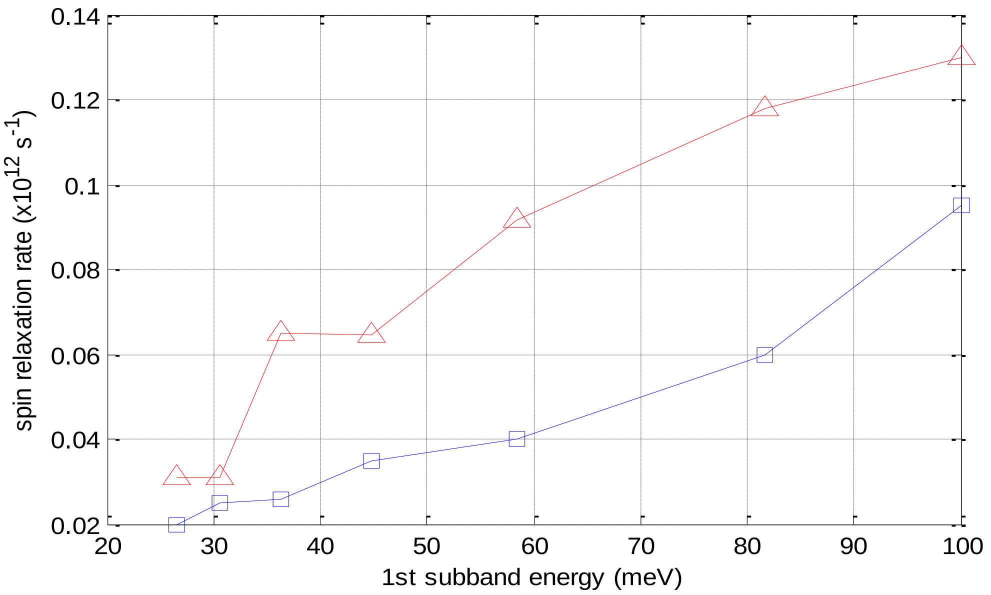

Figure 4.18 Spin relaxation rates, as determined by the EMC (red, top curve) are compared to experimental data (bottom, blue curve) for various well widths. The difference between the curves is likely due to higher carrier energies in the EMC compared to those of the optically excited carriers in the experiment [74].

In the results reported in [29, 69], and reiterated in Figure 4.18, the device channel was oriented along [1,0,0]. As discussed in the literature, though [72, 75], spin coherence is best obtained when the device channel is oriented at an angle of -45° with respect the [1,0,0] crystallographic axis. In particular, it has been reported [75] that if the device channel is oriented at an angle of -45° with respect to [1,0,0] and if the Rashba coefficient can be set to be equal to the Dresselhaus coefficient (by tuning the gate voltage, for example, and altering the local electric field in the quantum well), an optimal condition for spin coherence will result, since in this case the effective magnetic field for carrier precession is always oriented perpendicular to the transport direction. In this work, it was verified that $\xi = -45^\circ$ is indeed optimal, by conducting several "on the fly" simulations of spin decoherence at various values of the angle ξ in (3.82). Hence, the results presented next are for simulations in which $\xi = -45^{\circ}$ in (3.82).

Figure 4.19 depicts k-space simulations of spin decoherence for the heterostructure defined directly under the gate region of the Intel HEMT depicted in Figure 4.3. For the $In_{0.7}Ga_{0.3}As$ channel in the structure, the Rashba constant is taken as $\alpha = 29.9\, eV - \overset{\circ}{A}{}^{2}/V$ and the Kane parameter for the Dresselhaus constant is taken as $\beta = 98.5\, eV - \overset{\circ}{A}{}^{3}$, as derived from a linear interpolation between values given for pure compounds and other alloy molar fractions reported in [70, 75]. The ensemble is initially polarized along the growth direction at T=77K, and the decoherence, as a function of "position" (extracted from the time resolved k-space EMC), was determined. The departure from pure sinusoidal-like behavior at positions less than 10nm is likely due to the abrupt changes in the Rashba and Dresselhaus constants that result when intersubband scattering occurs.

Even though $\xi = -45^{\circ}$ for the simulation results reported in Figure 4.19, the fast dephasing may lead one to conclude that this heterostructure may not be well suited for a spintronics application. However, it was found that "tweeking " the Dresselhaus coefficient by a factor of 2-4 (though perhaps not physically justifiable) would improve the situation. Furthermore, an actual device simulation, as discussed next, yields better results.

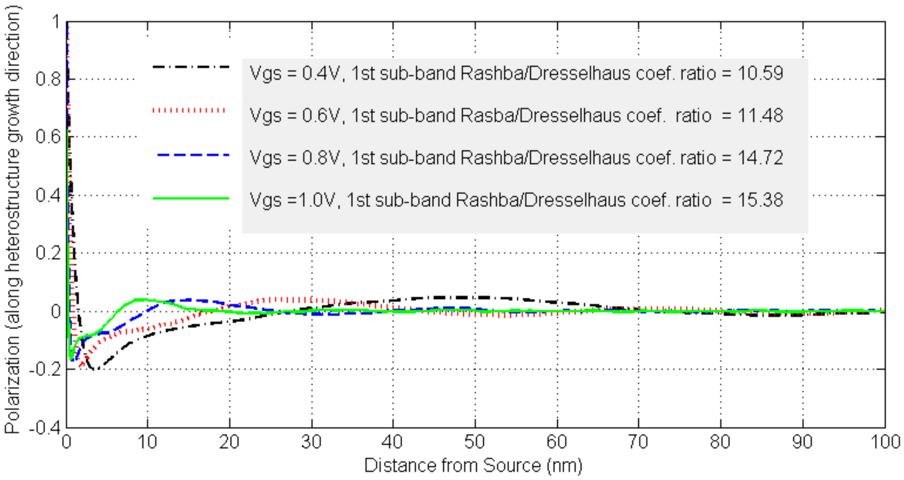

Figure 4.19 Decoherence as a function of "position" in k-space, for the heterostructure of the gate region of the Intel HEMT device depicted in Figure 4.3. T=77K. The driving electric field along the transport direction is 0.6 kV/cm.

For the results depicted in Figure 4.20, the device of Figure 4.3 has been scaled along the direction of transport, as noted by the dashed lines in Figure 4.20. However, the heterostructure is otherwise the same as in Figure 4.3 along each "slice" of the transport channel. To the best of this author's knowledge, the EMC simulation of the D'yakanov-Perel spin dynamics has not been previously reported for a device with the boundary conditions discussed in Chapter 3 or utilizing Rashba and Dresselhaus coefficients that are both subband and spatially dependent.

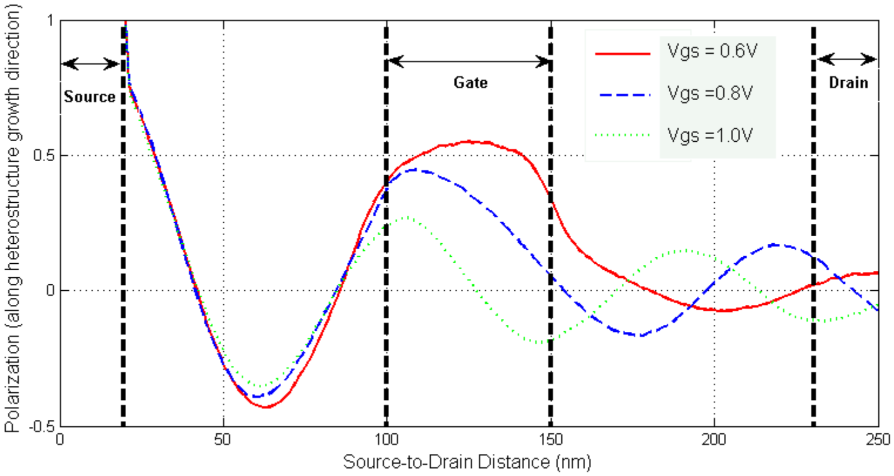

Figure 4.20 Spin polarization as a function of source to drain position in a scaled down version of the Intel HEMT depicted in Figure 4.3. V_{ds}= 0.15V. T= 77K.

As seen in Figure 4.20, an ensemble of carriers, 100% polarized along the heterostructure growth direction at the source contact, is injected into the device at T=77K. The initial spin distribution within the device is otherwise random, or "unpolarized". The local spin polarization at each "slice" along the transport channel is then computed as an average of spin polarizations of all carriers and averaged over time once the device has reached a steady state. (The achievement of steady state is checked by viewing charge-vs-time plots as previously discussed.) The constants α and β are as previously mentioned. However, since the electric field and quantum confinement varies over the device channel, the resulting Rashba and Dresselhaus coefficients, updated periodically during the simulation, result in more favorable Rashba/Dresselhaus ratios. This gives better coherence than in the case of the k-space simulation in which the coefficients vary only nominally as a function of time. In Figure 4.20, a "spin discrimination" mechanism was not simulated at the drain. However, the oscillations at the drain contact, in particular for the cases of V_{gs} = 0.8V and V_{gs} = 1.0 are clearly of opposite polarity. This perhaps indicates the viability of being able to tune the spin orientation at the drain, as a function of gate voltage in an actual SpinFET device. The extension of this model to include a "spin discriminator" at the drain will be the subject of future work.

5. Summary and Future Work

In summary, an ensemble Monte Carlo code has been developed to simulate, semi-classically, spin-polarized transport in III-V semiconductor nanostructures. The code was written in order to accommodate both 2D and 3D transport conditions, as carrier energies evolve during simulation. In doing this, an admixture of various “quantum corrections” was included in the model. These include periodic updating of the SWE at various regions of quantization during the simulation time and a unique method of modeling contacts in HEMTs. The applicability of the code to model D'yakanov-Perel spin scattering was also demonstrated.

In Chapter 1, a brief overview of carrier dynamics in semiconductors was presented. A physical justification for using Monte Carlo techniques to model carrier dynamics was presented that accounts for the relevant scattering mechanisms. Then, a brief historical overview of Monte Carlo semiconductor device simulation was presented. This culminated with a discussion of how the use of certain “quantum corrections” is needed in contemporary EMC modeling of low dimensional semiconductors. This code addressed many of those needs.

In Chapter 2, the dominant 2D and 3D scattering mechanisms in III-V compound were delineated. These included polar optical phonon, acoustic deformation potential, non-polar optical phonon, ionized impurity, alloy, and surface roughness scattering.

In chapter 3, the details of the EMC algorithm were presented, with a separate section devoted to each of the main components. It was discussed that the code was written modularly, in order to allow the easy inclusion of additional scattering rates. Furthermore, a unique description of contact modeling was presented, in the absence of a tunneling model. In this method, the quantum mechanical distribution of carriers at the contacts, found from a self-consistent SWE-Poisson solution is maintained at each time step. This method is in contrast to the usual 3D "charge neutral" contact procedure that is common practice in the semi-classical HEMT modeling community.

In Chapter 4, results were presented that demonstrate reasonable success has so far been achieved with the EMC, warranting further development. First, a validation of the EMC algorithm was performed by simulating transport in bulk III-V systems. Results were in excellent agreement with the published results of other modeling groups. Then, the model was applied to the simulation of a HEMT device, which has been under recent experimental investigation by researchers at Intel Corporation. The results clearly indicate the relative effect of various structural and scattering parameters to serve as an aid in the future development of such HEMT devices. Finally, the EMC was used to model spin-polarized electron transport in a prototypical SpinFET device.

For future HEMT modeling, several modifications will be made to the EMC code. First, non-parabolic 2D scattering rates will be implemented. This is expected to be a straightforward procedure, as such scattering mechanisms are well known for simple non-parabolic bandstructures. Second, the modeling of 2D/3D transitions can perhaps be altered by using 2D/3D "capture" and "escape" scattering rates, in a manner more consistent with the usual momentum scattering rates already implemented. Third, a tunneling model needs to be implemented to treat the contacts more accurately. Additionally, the use of more realistic band-structures needs to be considered, as opposed to using simple 3-valley models.

With regard to future spintronics modeling, spin discrimination at the drain will be modeled. The proper usage of other scattering mechanisms, such as the Elliot-Yafet mechanism needs to also be considered. Finally, the applicability of using the EMC to conduct a semi-classical simulation of the Spin Hall effect will be researched. In particular, use of a modified form of the Rashba Hamiltonian to account for an electric field along the transport direction needs to be investigated.

REFERENCES

[1] G.E. Moore, “Cramming more components onto integrated circuits,” *Electronics*, vol. 38 (1965).

[2] R.H. Dennard, F.H. Gaensslen, H.N. Yu, V.L. Rideout, E. Bassous, and A.R. LeBlanc, “Design of ion-implanted MOSFET’s with very physical dimensions,” *IEEE J. Solid-State Circuits*, vol. SC-9 (1974): pp. 256-268.

[3] J.R. Brews, W. Fichtner, E.H. Nicollian, and S.M. Sze, “Generalized guide for MOSFET miniaturization.” *IEEE Electron Dev. Lett.*, vol. 1 (1980): pp. 2-4.

[4] G. Baccarani, M.R. Wordeman, and R. H. Dennard, “Generalized theory and its application to 114 micron MOSFET design,” *IEEE Trans. Electron Devices*, vol. 31 (1984): pp. 452-462.

[5] K.K. Ng, S.A. Eshraghi, and T.D. Stanik, “An improved generalized guide for MOSFET scaling,” *IEEE Trans. Electron Devices*, vol. 40 (1993): pp. 1895-1897.

[6] K.J. Kuhn. “Moore's Law past 32nm: Future Challenges in Device Scaling.” download.intel.com/pressroom/pdf/kkuhn/Kuhn_IWCE_invited_text.pdf.

[7] G.D. Wilk, R.M. Wallace, and J.M. Anthony, “High-κ gate dielectrics: Current status and materials properties considerations,” *J. Appl. Phys.*, vol. 89 (2001): pp. 5243-5725.

[8] S-W Sun, P.G.Y. Tsui, “Limitation of CMOS Supply-Voltage Scaling by MOSFET Threshold-Voltage Variation,” *IEEE J. Solid-State Circuits*, vol. 30, No. 8 (1995): pp.947-949.

[9] B. Razavi, *Design of Analog CMOS Integrated Circuits* (Boston, MA: McGraw Hill, 2001), pp. 579-600.

[10] D.A. Tichenor, G.D. Kubiak, S.J. Haney, R.P. Nissen, K.W. Berger, R.W. Arling, A.K. Ray-Chaudhuri, K.B. Nguyen, R.H. Stulen, J.B. Wronosky, J.D. Jordan, T.G. Smith, J.R. Darnold, P.M. Kahle, A.A. Jojola, S.M. Kohler, R.S. Urenda, D.R. Wheeler, J.E. Bjorkholm, O.R. Wood II, G.N. Taylor, and R.S. Hutton, “Recent results in the development of an integrated EUVL laboratory tool,” *Proc. SPIE Int. Soc.Opt. Eng.*, vol. 2437 (1995): pp. 292-307.

[11] G.D. Wilk, R.M. Wallace, and J.M. Anthony, “High-κ gate dielectrics: Current status and materials properties considerations,” *J. Appl. Phys.*, vol. 89 (2001): pp. 5243-5725.

[12] T. Mimura, S. Hiyamizu, T. Fujii, and K. Nanbu, “A New Field-Effect Transistor with Selectively Doped GaAs/n-AlxGa1-xAs Heterojunctions,” *Jpn. J. Appl. Phys.*, vol. 19 (1980): pp. L225-L227.

[13] H. Daemkes, *Modulation-Doped Field Effect Transistors: Principles, Design and Techniques*, (New York: IEEE Press, 1991).

[14] P. Price, “Low-temperature, two-dimensional mobility of a GaAs heterolayer,” *Surf. Sci.*, Vol. 143, No. 1 (1984): pp. 145–156.

[15] W. Walukiewicz, H.E. Ruda, J. Lagowski, and H.C. Gatos, “Electron mobility in modulation doped heterostructures,” *Phys. Rev. B, Condens. Matter*, Vol. 30, No. 8 (1984): pp. 4571–4582.

[16] D. Dawson, L. Samoska, A.K. Fung, K. Lee, R. Lai, R. Grundbacher, P.-H. Liu, and R. Raja, “Beyond G-band: A 235 GHz InP MMIC amplifier,” *IEEE Microw. Wireless Compon. Lett.*, vol. 15, no. 12 (2005): pp. 874–876.

[17] G. Dewey, R. Kotlyar, R. Pillarisetty, M. Radosavljevic, T. Rakshit, H. Then, and R. Chau. “Logic Performance Evaluation and Transport Physics of Schottky Gate III-V Compound Semiconductor Quantum Well Field Effect Transistors for Power Supply Voltages (Vcc) Ranging from 0.5V to 1.0V,” *IEDM, IEEE International*, pp. 1-4, Dec. 7-9, 2009.

[18] P.M. Smith, “Status of InP HEMT technology for microwave receiver applications,” *Microwave and Millimeter-Wave Monolithic Circuits Symposium*, Digest of Papers, IEEE 1996.

[19] S. Takagi et al., Intl. Symposium on VLSI Technology, Systems and Applications, *Solid-State Electronic.*, 51 (2007) 526; 55 (2008) 21; VLSI symp. (2010) 147.

[20] C. Jacoboni and P. Lugli, *The Monte Carlo Method for Semiconductor Device Simulation*, (Berlin, Germany: Springer-Verlag, 1989).

[21] S. Datta and B. Das, “Electronic analog of the electro-optical modulator,” *Appl. Phys. Lett.*, vol. 56 (1990): pp. 665-667.

[22] D.C. Marinescu, G.M. Marinescu, *Approaching Quantum Computing*, (Pearson Prentice Hall, 2005).

[23] S. Das Sarma et al., "Theoretical Perspectives on Spintronics and Spin-Polarized Transport," *IEEE Transactions on Magnetics*, Vol. 36, No. 5 (2000).

[24] I. Zutic, J. Fabian, S. Das Sarma "Spintronics: Fundamentals and Applications," *Review of Modern Physics*, Vol. 76 (2004): pp. 323-410.

[25] S.A. Wolf et al., "Spintronics- A Retrospective and Perspective," *IBM J. Res. & Dev.*, Vol. 50, No. 1 (2006).

[26] Y.A. Bychkov, E.I. Rashba, "Oscillatory effects and the magnetic susceptibility of carriers in inversion layers," *J. Phys. C: Solid State Phys.*, Vol. 17, No. 9 (1984): pp. 6039-6045.

[27] B.T. Jonker et al., "Electrical spin-injection into silicon from a ferromagnetic metal/tunnel barrier contact," *Nature Physics*, Vol. 3 (2007): pp. 542-546.

[28] M.J. Gilbert and J.P. Bird, "Application of Split-Gate Structures as Tunable Spin Filters," *Applied Physics Letters*, Vol. 77 (2000): pp. 1050-1052.

[29] B.D. Tierney, T.E. Day, S.M. Goodnick, "Investigation of spin-polarized transport in GaAs nanostructures," *Journal of Physics: Conf. Ser. 109*, 2008.

[30] J. Nitta, T. Akazaki, and H. Takayanagi, "Gate Control of Spin-Orbit Interaction in an Inverted $In_{0.53}Ga_{0.47}As/In_{0.52}Al_{0.48}As$ Heterostructure," *Phys. Rev. Lett.*, vol. 78 (1997): pp. 1335-1338.

[31] Th. Schäpers, G. Engels, J. Lange, Th. Klocke, M. Hollfelder, and H. Lüth, "Effect of the heterointerface on the spin splitting in modulation doped InxGa1-xAs/InP quantum wells for B→0," *J. Appl. Phys.*, vol. 83 (1998): pp. 4324-4333.

[32] D. Grundler, "Large Rashba Splitting in InAs Quantum Wells due to Electron Wave Function Penetration into the Barrier Layers," *Phys. Rev. Lett.*, vol. 84 (2000): pp. 6074-6077.

[33] M. Saraniti, *Development of Efficient Numerical Techniques for Semiconductor Device Simulations*, Ph.D. dissertation, Dept. of Physics, Technical University of Munich, Munich, Germany, 1996.

[34] P.A. Markowich and C. Ringhofer, *Semiconductor Equations*, (New York: Springer-Verlag Wien, 1990).

[35] W. Fawcett, A.D. Boardman, and S. Swain, "Monte Carlo Determination of Electron Transport Properties in Gallium Arsenide," *J Phys. Chem. Solids,* vol. 31 (1970): pp. 1963-1990.

[36] D. Vasileska and S.M. Goodnick, *Computational Electronics,* (United States of America: Morgan & Claypool, 2006).

[37] T. Kurosawa, Proc. Int. Conf. Phys. Semicond., Kyoto, 1966; *J. phys. Soc. Japan Suppl.,*21, 424, 1966.

[38] P.J. Price, "Monte Carlo calculation of electron transport in solids," *Semiconductors and Semimetals,* Vol. 14 (1979), pp. 249-334.

[39] C. Jacoboni and L. Reggiani, "The Monte Carlo method for the solution of charge transport in semiconductors with applications to covalent materials," *Rev. Mod. Phys.,* Vol. 55 (1983), pp. 645-705.

[40] T. Wang and K. Hess, "Calculation of the electron velocity distribution in high electron mobility transistor using an ensemble Monte Carlo method," *J. Appl. Phys.,* Vol. 57, No. 12 (1985): pp. 5336–5339.

[41] M. Tomizawa, A. Yoshii, and K. Yokoyama, "Modeling for an AlGaAs/GaAs heterostructure device using Monte Carlo simulation," *IEEE Electron Device Lett.*, Vol. EDL-6, No. 7 (1985): pp. 332–334.

[42] K. Yokoyama and K. Hess, "Monte Carlo study of electronic transport in Al1−xGaxAs/GaAs single-well heterostructures," *Phys. Rev. B, Condens.Matter*, vol. 33, no. 8 (1986): pp. 5595–5606.

[43] U. Ravaioli and D.K. Ferry, "MODFET ensemble Monte Carlo model including the quasi-two-dimensional electron gas," *IEEE Trans. Electron Devices*, Vol. ED-33, No. 5 (1986): pp. 677–680.

[44] H. Shichijo and K. Hess, "Band-structure-dependent transport and impact ionization in GaAs," *Phys. Rev. B, Condens. Matter*, vol. 23, No. 8 (1981): pp. 4197–4207.

[45] H. Shichijo, K. Hess, and G.E. Stillman, "Simulation of high-field transporting GaAs using a Monte Carlo method and pseudopotential bandstructures," *Appl. Phys. Lett.,* vol. 38, No. 2 (1981): pp. 89–91.

[46] M.V. Fischetti and S.E. Laux, "Monte Carlo analysis of electron transport in small semiconductor devices including band-structure and space-charge effects," Phys. *Rev. B, Condens. Matter,* vol. 38, No. 14 (1988): pp. 9721–9745.

[47] S.E. Laux and M.V. Fischetti, “Monte-Carlo simulation of submicrometer Si n-MOSFETs at 77 and 300 K,” *IEEE Electron Device Lett.*, Vol. 9, No. 9 (1988): , pp. 467–469.

[48] M. Saraniti and S.M. Goodnick, “Hybrid fullband cellular automaton/Monte Carlo approach for fast simulation of charge transport in semiconductors,” *IEEE Trans. Electron Devices*, vol. 47, no. 10 (2000): pp. 1909–1916.

[49] D. Ferry, “The onset of quantization in ultra-submicron semiconductor devices,” *Superlattices & Microstructures*, vol. 27 (2000), p. 61.

[50] H. Tanimoto, N. Yasuda, K. Taniguchi, and C. Hamaguchi, “Monte Carlo Study of Hot Electron Transport in Quantum Wells,” *Jpn. J. Appl. Phys.*, vol. 27, No. 4 (1988), pp. 563-571.

[51] H. Ueno, S. Yamakawa, C. Hamaguchi, and K. Miyatsuji, “Monte Carlo Simulation of HEMT,” Physics, pp. 85-89, 1995 workshop on physics and computer modeling of devices based on low-dimensional Structures (PHYSICS'95), 1995

[52] B. Winstead and R. Ravaioli, “A quantum correction based on Schrödinger equation applied to Monte Carlo device simulation,” *IEEE Trans. Electron Dev.*, vol. 50, issue 2 (2003): pp. 440-336.

[53] C. Heitzinger, C. Ringhofer, S. Ahmed, and D. Vasileska, “3D Monte-Carlo Device Simulations Using an Effective Quantum Potential Including Electron-Electron Interactions,” *J. Comput. Electron.*, Vol. 6, Numbers 1-3 (2007): pp. 15-18.

[54] L.F. Register and N. Shi, “Schrödinger-equation-based quantum corrections addressing degeneracy-breaking and confinement-enhanced scattering,” *J. Comput. Electron.*, Vol. 9, Numbers 3-4 (2010), pp. 201-205.

[55] K. Tomizawa, *Numerical Simulation of Submicron Semiconductor Device*, (Boston: Artech House, 1993), pp. 25-33

[56] E.O. Kane, Semiconductors and Semimetals, ed. R.K. Willardson and A.C. Beer (Academic, New York, 1966) Vol. 1, p. 75.

[57] P.J. Price, “Two-dimensional electron transport in semiconductor layers, I. Phonon Scattering”, *Ann. Phys.*, vol. 133 (1981): p. 217.

[58] M.A. Littlejohn, J.R. Hauser, T.H. Glisson, D.K. Ferry, and J.W. Harrison, “Alloy Scattering And High Field Transport In Ternary And Quaternary III-V Semiconductors, " *Solid State Electronics*, Vol. 21 (1978): pp. 107-114.

[59] F.A. Riddoch and B.K. Ridley, “On the scattering of electrons by polar optical phonons in quasi-2D quantum wells,” *J. Phys. C: Solid State Phys.*, vol. 16 (1983): pp. 6971-6982.

[60] S.M. Goodnick and P. Lugli, *Hot Carriers In Semiconductor Nanostructures*, *Physics and Applications*, ed. J. Shah (San Diego: Academic, 1992): pp. 191-234.

[61] S.M. Goodnick, D.K. Ferry, C.W. Wilmsen, Z. Liliental, D. Fathy, and O.L. Krivanek “Surface roughness at the Si (100)-SiO2 interface,” *Phys. Rev. B*, vol. 32, No. 12 (1985): pp. 8171-8186.

[62] S. Jin, M. Fischetti, and T. Tang, “Modeling of Surface-Roughness Scattering in Ultrathin-Body SOI MOSFETs,” *IEEE Trans. Electron Dev.*, vol. 54, No. 9 (2007): pp. 2191-2203.

[63] K. Tomizawa, *Numerical Simulation of Submicron Semiconductor Device*, (Boston: Artech House, 1993), pp. 79-114.

[64] I.H. Tan, G.L. Snider, L.D. Chang, and E.L. Hu “A self-consistent solution of Schrödinger-Poisson equations using a non-uniform mesh,” *J. Appl. Phys.*, vol. 68 (1990): pp. 4071-4076.

[65] R.W. Hockney and J.W. Eastwood, *Computer Simulation Using Particles*, (Bristol and New York: Adam Hilger, 1988), Chapter 10.

[66] M. Abou-Khalil, M. Goano, A. Champagne, and R. Maciejko, “Capture and escape in quantum wells as scattering events in Monte Carlo simulation,” *Photonics Tech. Letters, IEEE,* vol. 8, No. 1 (1996): pp. 19-21.

[67] P. Lugli and D.K. Ferry, “Degeneracy in the Ensemble Monte Carlo Method for High Field Transport in Semiconductors,” IEEE Trans. Electron Dev., vol. ED-32, No. 11 (1985): pp. 2431-2437.

[68] G. Dresselhaus, “Spin-orbit Coupling Effects in Zinc Blend Structures,” *Physical Review,* Vol. 100, No. 2 (1955): pp. 580-586.

[69] B.D. Tierney, and S. M. Goodnick, “Monte Carlo simulation of spin-polarized transport in GaAs nanostructures” Nanotechnology, 2007, *IEEE-NANO 2007,* 7th IEEE Conf. On (2007): pp. 414-417.

[70] S. Saikin, M. Shen, M. Cheng, and V. Privman "Semi-classical Monte Carlo model for in-plane transport of spin polarized electrons in III-V heterostructures," *J. of Appl. Phys.*, Vol. 94, No. 3 (2003): p. 1769.

[71] W. Zawadzki, P. Pfeffer, "Spin splitting of subband energies due to inversion asymmetry in semiconductor heterostructures," *Semicond. Sci. Technol.*, Vol. 19 (2004): pp. R1-R17.

[72] S. Saikin, M. Shen, M. Cheng "Study of Spin-Polarized Transport Properties for Spin-FET Design Optimization," *IEEE Trans. Electron Devices*, vol. 3, no. 1 (2004): pp. 173-179.

[73] E. Shafir et al., "Modulation of spin dynamics in a channel of a non-ballistic spin field effect transistor," *Phys. Rev. B*, Vol. 70 (2004): 241302(R).

[74] A. Malinowski et al., "Investigation of spin-polarized transport in GaAs nanostructures," *Phys. Rev. B*, Vol 62, No. 19 (2000): pp. 13034-13039.

[75] M. Ohno, K. Yoh., "Datta-Das-type spin-field-effect transistor in the non-ballistic regime," *Phys. Rev. B*, Vol 77 (2008): pp. 045323-1 - 045323-7.